

FILE COPY

AD -

TERMINATION OF GENERAL AND SPECIFIC PROPERTIES OF WIDE ENERGY-
BAND GAP HgCdTe IN THE 1 TO 2 MICROMETER WAVELENGTH RANGE

FINAL TECHNICAL REPORT

By

Nguyen-Duy T., Durand A., Royer M., and Raymond F.

September 1988

United States Army

EUROPEAN RESEARCH OFFICE OF THE U.S. ARMY

London England

CONTRACT NUMBER: DAJA45-87-C-0020

Societe Anonyme de Telecommunications

DTIC
ELECTE
OCT 17 1988
S & D
H

Approved for Public Release; distribution unlimited

88 1014 077

AD-A201 341

REPORT DOCUMENTATION PAGE

1a. REPORT SECURITY CLASSIFICATION Unclassified			1b. RESTRICTIVE MARKINGS		
2a. SECURITY CLASSIFICATION AUTHORITY			3. DISTRIBUTION/AVAILABILITY OF REPORT Approved for public release; distribution unlimited		
2b. DECLASSIFICATION/DOWNGRADING SCHEDULE					
4. PERFORMING ORGANIZATION REPORT NUMBER(S) 7313/88			5. MONITORING ORGANIZATION REPORT NUMBER(S) R&D 5574-EE-01		
6a. NAME OF PERFORMING ORGANIZATION Societe Anonyme de Telecommunications		6b. OFFICE SYMBOL (If applicable)	7a. NAME OF MONITORING ORGANIZATION USARDSG-UK		
6c. ADDRESS (City, State, and ZIP Code) 41, Rue Cantagrel 75631 Paris Cedex 13 France			7b. ADDRESS (City, State, and ZIP Code) Box 65 FPO NY 09510-1500		
8a. NAME OF FUNDING/SPONSORING ORGANIZATION DARPA		8b. OFFICE SYMBOL (If applicable)	9. PROCUREMENT INSTRUMENT IDENTIFICATION NUMBER DAJA45-87-C-0020		
8c. ADDRESS (City, State, and ZIP Code) 1400 Wilson Boulevard Arlington VA 22209-2308			10. SOURCE OF FUNDING NUMBERS		
PROGRAM ELEMENT NO. 61103A		PROJECT NO. 11161103BH57	TASK NO. 03	WORK UNIT ACCESSION NO.	
11. TITLE (Include Security Classification) Study for the Determination of General and Specific Properties of Wide Energy-Band Gap HgCdTe in the 1 to 2 micrometer Wavelength Range					
12. PERSONAL AUTHOR(S) Nguyen-Duy, T., Durand A., Royer M., Raymond F.					
13a. TYPE OF REPORT Final Report		13b. TIME COVERED FROM 1987 TO 1988		14. DATE OF REPORT (Year, Month, Day) 88SEP09	
15. PAGE COUNT 85					
16. SUPPLEMENTARY NOTATION					
17. COSATI CODES			18. SUBJECT TERMS (Continue on reverse if necessary and identify by block number)		
FIELD	GROUP	SUB-GROUP	WIDE ENERGY-BAND GAP, MERCURY CADMIUM TELLURIDE, INFRARED		
09	01		DETECTION, TRAVELING HEATER METHOD, HgCdTe BULK MATERIAL,		
17	05		HgCdTe PHYSICAL PROPERTIES, HgCdTe OPTICAL PROPERTIES. <i>mjm</i>		
19. ABSTRACT (Continue on reverse if necessary and identify by block number) The metallurgical process of Wide Band Gap Mercury Cadmium Telluride (WBHCT) compound fabrication is briefly reviewed. Special emphasis is given to the Traveling Heater Method (THM) for HgCdTe growth. Physical and electronic properties are analyzed with particular attention to properties that apply to optoelectronic devices. Some special features, such as low intrinsic concentration, low band gap temperature coefficient and matching of band gap to spin orbit coupling appear to be of particular and unique interest in the fabrication of avalanche photodiodes (APD) in this spectral region. Electroluminescent properties have also been investigated. Light-emitting structures are discussed.					
20. DISTRIBUTION/AVAILABILITY OF ABSTRACT <input checked="" type="checkbox"/> UNCLASSIFIED/UNLIMITED <input type="checkbox"/> SAME AS RPT. <input checked="" type="checkbox"/> DTIC USERS			21. ABSTRACT SECURITY CLASSIFICATION Unclassified		
22a. NAME OF RESPONSIBLE INDIVIDUAL Dr. John M. Zavada			22b. TELEPHONE (Include Area Code) 01-409-4423		22c. OFFICE SYMBOL AMXSN-UK-R1

18. Subject Terms (continued)

HgCdTe LIGHT EMITTING PROPERTIES



Accession For	
NTIS GRA&I	<input checked="" type="checkbox"/>
DTIC TAB	<input type="checkbox"/>
Unannounced	<input type="checkbox"/>
Justification	
By	
Distribution/	
Availability Codes	
Dist	Avail and/or Special
A-1	

AD -

DETERMINATION OF GENERAL AND SPECIFIC PROPERTIES OF WIDE ENERGY-
BAND GAP HgCdTe IN THE 1 TO 2 MICROMETER WAVELENGTH RANGE

FINAL TECHNICAL REPORT

By

Nguyen-Duy T., Durand A., Royer M., and Raymond F.

September 1988

United States Army

EUROPEAN RESEARCH OFFICE OF THE U.S. ARMY

London England

CONTRACT NUMBER: DAJA45-87-C-0020

Societe Anonyme de Telecommunications

Approved for Public Release; distribution unlimited

TABLE OF CONTENTS

	page
LIST OF FIGURES	iii
ABSTRACT	1
KEYWORDS	1
LIST OF PARTICIPATING PERSONNEL	1
 I - INTRODUCTION	 2
 II - METALLURGICAL PROCESSES	 3
II.1 - LIQUID-PHASE EPITAXY	3
II.2 - VAPOR-PHASE EPITAXY	3
II.3 - BULK MATERIAL	4
 III - PHYSICAL PROPERTIES	 5
III.1 - CRYSTAL STRUCTURE	5
III.2 - THERMAL PROPERTIES	5
III.3 - MECHANICAL PROPERTIES	7
 IV - ELECTRONIC PROPERTIES AND BAND STRUCTURE	 9
IV.1 - BAND GAP ENERGY VARIATION	9
IV.2 - BAND STRUCTURE	10
IV.3 - INTRINSIC CARRIER CONCENTRATION	11
IV.4 - MOBILITY	12
 V - OPTICAL PROPERTIES	 14
V.1 - TRANSMISSION NEAR THE BAND GAP	14
V.2 - ELECTRO-REFLECTANCE NEAR THE E_g TRANSITIONS	14
V.3 - MEDIUM AND FAR INFRARED TRANSMISSION	16

	page
VI - ADVANTAGES OF WIDE BAND GAP HgCdTe	16
VII - ADVANTAGES OF HgCdTe AVALANCHE PHOTODIODES	17
VII.1 - GAP SPIN-ORBIT RESONANCE	17
VII.2 - DESCRIPTION OF THE PHOTODIODE	18
VII.3 - DIODE CHARACTERIZATION	21
VIII - INVESTIGATION AND FEASIBILITY OF LARGE AREA DETECTORS	24
VIII.1 - JUSTIFICATION FOR EXTRAPOLATION	24
VIII.2 - RESULTS ACHIEVED	25
VIII.3 - MEASUREMENTS AND ADVANTAGES OF LOW TEMPERATURE OPERATION	26
IX - HgCdTe LIGHT-EMITTING PROPERTIES	27
IX.1 - INTRODUCTION	27
IX.2 - HgCdTe PROPERTIES PERTINENT TO LED PROCESSING	27
X - CONCLUSIONS	30
LITERATURE CITED	31
FIGURES	35

LIST OF FIGURES

- Fig. 1 - Band gap energy and detector cutoff wavelength vs. composition
- Fig. 2 - Detector cutoff wavelength vs. composition in the 1- 2 μm spectral wavelength region
- Fig. 3a - Principle of THM process
- Fig. 3b - Steps of a THM growth run
- Fig. 4 - Longitudinal homogeneity of three THM-grown ingots as a function of detector cutoff wavelength
- Figs. 5a/b Radial homogeneity of THM wafers for different diameters
- Fig. 6 - Zinc blende crystal lattice (after Long (34))
- Fig. 7 - Lattice constant and density vs. composition
- Fig. 8 - Microhardness vs. composition for $\text{Hg}_{1-x}\text{Cd}_x\text{Te}$
- Fig. 9 - Variation of gap energy vs. composition
- Fig. 10 - Band structure of CdTe
- Fig. 11 - Band structure of HgTe
- Fig. 12 - Band structure of $\text{Hg}_{0.3}\text{Cd}_{0.7}\text{Te}$
- Fig. 13 - E_g and Δ_0 vs. composition
- Fig. 14 - Intrinsic carrier concentration
- Fig. 15 - Electron mobility at 300 K
- Fig. 16 - Electron mobility of N-type $\text{Hg}_{1-x}\text{Cd}_x\text{Te}$ at 300 K
- Fig. 17 - Electron mobility of N-type $\text{Hg}_{1-x}\text{Cd}_x\text{Te}$ at 77 K
- Fig. 18 - Optical transmission vs. wavelength
- Fig. 19 - Internal transmission of $\text{Hg}_{0.3}\text{Cd}_{0.7}\text{Te}$ vs. wavelength for different wafer thicknesses
- Fig. 20 - Absorption coefficient vs. wavelength for $\text{Hg}_{0.3}\text{Cd}_{0.7}\text{Te}$
- Fig. 21 - Absorption coefficient vs. wavelength for different values of E_g
- Fig. 22 - Relative change of reflectivity at different temperatures for $x = 0.6$
- Fig. 23 - Theoretical and experimental transmission curves for $E_g = 0.89$ eV
- Fig. 24 - Theoretical and experimental transmission curves for $E_g = 0.59$ eV
- Fig. 25 - Transmission curves for different P-type concentrations at $E_g = 0.89$ eV
- Fig. 26 - Transmission curves for different P-type concentrations at $E_g = 0.59$ eV
- Fig. 27 - Hole-generated spin-orbit resonance
- Fig. 28a - Cross-sectional structure of an avalanche photodiode
- Fig. 28b - Cross-sectional view of an avalanche photodiode
- Fig. 29 - Breakdown at the edge of the junction of a photodiode without guard ring
- Fig. 30 - Central multiplication of a photodiode with guard ring
- Fig. 31 - Schematic structure across the junction
- Fig. 32 - Valenza's doping profile
- Fig. 33 - Electric field as a function of distance, as reported by Valenza
- Fig. 34 - I(V) curve of an avalanche photodiode

- Fig. 35 - Voltage-capacitance characteristics up to 80 V
- Fig. 36 - Spectral response of a $\text{Hg}_{0.3}\text{Cd}_{0.7}\text{Te}$ photodiode at 300 K
- Fig. 37 - Multiplication as a function of voltage
- Fig. 38 - Photo-response as a function of distance (spot scan along one diameter) for different values of reverse bias voltage
- Fig. 39 - Schematic layout of the test bench for the measurement of avalanche noise
- Fig. 40 - Photon flux noise as a function of multiplication
- Fig. 41 - Main characteristics of $1.3\text{ }\mu\text{m}$ HgCdTe avalanche photodiodes
- Fig. 42 - $I(V)$ characteristics of a $1.3\text{ }\mu\text{m}$ photodiode (0.080 mm dia.)
- Fig. 43 - $I(V)$ characteristics of a $1.3\text{ }\mu\text{m}$ photodiode (0.250 mm dia.)
- Fig. 44 - $I(V)$ characteristics of a $1.3\text{ }\mu\text{m}$ photodiode (1 mm dia.)
- Fig. 45 - $I(V)$ characteristics of a $1.3\text{ }\mu\text{m}$ photodiode (2 mm dia.)
- Fig. 46 - $I(V)$ characteristics of a $1.3\text{ }\mu\text{m}$ photodiode (5 mm dia.)
- Fig. 47 - $I(V)$ characteristics of a $1.55\text{ }\mu\text{m}$ photodiode (0.080 mm dia.)
- Fig. 48 - $I(V)$ characteristics of a $1.55\text{ }\mu\text{m}$ photodiode (1 mm dia.)
- Fig. 49 - $I(V)$ characteristics of a $1.55\text{ }\mu\text{m}$ photodiode (2 mm dia.)
- Fig. 50 - $I(V)$ characteristics of a $1.55\text{ }\mu\text{m}$ photodiode (5 mm dia.)
- Fig. 51 - Saturation current as a function of diode area
- Fig. 52 - $I(V)$ characteristics of a $1.55\text{ }\mu\text{m}$ photodiode, 5 mm dia., at $T = +55^\circ\text{C}$
- Fig. 53 - $I(V)$ characteristics of a $1.55\text{ }\mu\text{m}$ photodiode, 5 mm dia., at $T = -15^\circ\text{C}$
- Fig. 54 - Reverse $I(V)$ characteristics of a $1.55\text{ }\mu\text{m}$ photodiode, 5 mm dia., as a function of diode temperature
- Fig. 55 - Reverse variation of R_{VO} as a function of diode temperature
- Fig. 56 - Variation of saturation current as a function of diode temperature
- Fig. 57 - HgCdTe photodiode emission spectra
- Fig. 58 - Emitted power as a function of current and $I(V)$ characteristics

ABSTRACT

The metallurgical process of Wide Band Gap Mercury Cadmium Telluride (WBHCT) compound fabrication is briefly reviewed. Special emphasis is given to the Traveling Heater Method (THM) for HgCdTe growth.

Physical and electronic properties are analyzed with particular attention to properties that apply to optoelectronic devices. Some special features, such as low intrinsic concentration, low band gap temperature coefficient and matching of band gap to spin orbit coupling appear to be of particular and unique interest in the fabrication of avalanche photodiodes (APD) in this spectral region. Electroluminescent properties have also been investigated. Light-emitting structures are discussed.

KEYWORDS

WIDE ENERGY-BAND GAP MERCURY CADMIUM TELLURIDE
INFRARED DETECTION
TRAVELING HEATER METHOD
HgCdTe BULK MATERIAL
PHYSICAL PROPERTIES
ELECTRONIC PROPERTIES
OPTICAL PROPERTIES
AVALANCHE PHOTODIODES
LIGHT EMITTING PROPERTIES

LIST OF PARTICIPATING PERSONNEL

Nguyen-Duy, T., Principal Investigator
Durand, A.
Flachet, C.
Lux, F.
Pitault, B.
Radix, J.-C.
Raymond, F.
Royer, M.

I - INTRODUCTION

For many years, HgCdTe compounds have been widely investigated in the mercury-rich composition range for medium (3 to 5 μm) and far (8 - 12 μm) infrared detection devices.

The advantage of HgCdTe in the cadmium-rich (WBHCT) composition range, mainly in the two low-loss channels at 1.3 μm and 1.55 μm has manifested itself with the advent of fiber optical telecommunication systems.

The purpose of this study was to review the possibility to extend the detection and emission spectral band of this material from 1 μm to 2 μm for the development of high-performance optoelectronic devices.

The first interim report dealt with the investigation of suitable growth techniques for this composition range and analysis of the Traveling Heater Method (THM) developed by Societe Anonyme de Telecommunications (SAT). The electronic, optical and physical properties of these alloys are reviewed. Some particular properties, such as band gap and spin orbit energy ratio are analyzed for APD applications.

II - METALLURGICAL PROCESSES

For the mercury-rich composition range, a great number of publications, describing several techniques, can be found in the literature.

On the other hand, much less has been published on WBHCT for the 1 - 2 μm wavelength range. This discrepancy is considerably magnified when compared with the wealth of literature which exists for the III-V compounds.

However, the most important growth methods are encountered and dealt with for both epitaxial and bulk materials (1).

As shown in Figs. 1 and 2, the WBHCT corresponds to $\text{Hg}_{1-x}\text{Cd}_x\text{Te}$ alloys for which $0.5 < x < 0.9$.

II.1 - LIQUID-PHASE EPITAXY (LPE)

The growth of LPE layers has been carried out for compositions of $x \leq 0.5$ (2) and $x = 0.73$ to 0.75 for heterojunction mesa diodes at $1.3 \mu\text{m}$ (3). These epitaxies were carried out on CdTe substrates, generally (111) oriented, by means of a vertical dipping system.

More recently, LPE growth of $\text{Hg}_{0.3}\text{Cd}_{0.7}\text{Te}$ has been reported (4) on CdTe and $\text{Cd}_{0.9}\text{Zn}_{0.1}\text{Te}$ substrates in a closed-tube apparatus by the tipping method. This latter substrate provides lattice matching with the epitaxial layer.

In all cases the growth temperature was within the 550 to 600°C range and the layer thickness was within 10 to 40 micrometers.

II.2 - VAPOR-PHASE EPITAXY

Only a few publications are available on MBE and MOCVD methods.

As far as MOCVD is concerned, the growth of $\text{Hg}_{0.34}\text{Cd}_{0.66}\text{Te}$ (5) is obtained through an interdiffused multilayer process (6), (7), at a temperature of 420°C with a growth rate up to $30 \mu\text{m hr}^{-1}$ on CdTe, $\text{Cd}_{1-y}\text{Zn}_y\text{Te}$ and GaAs substrates with thickness up to $20 \mu\text{m}$.

With the MBE technique, $\text{Hg}_{0.6}\text{Cd}_{0.4}\text{Te}$ layers have been grown (8) on GaAs in order to obtain monolithic IRCCD devices. The layer is grown at low temperature (50°C) and low rate ($1.7 \mu\text{m h}^{-1}$) to a final thickness of $20 \mu\text{m}$.

Lattice mismatch between HgCdTe and GaAs induces poor electrical properties. To reduce this effect, a CdTe buffer layer is grown between the GaAs and HgCdTe materials.

The isothermal evaporation diffusion process (EDRI) (9), (10), has been used to grow wide band gap HgCdTe on CdTe substrates for waveguide applications (11) at 10.6 μm . A graded interdiffused layer of HgCdTe in CdTe was obtained with an x-value varying between 0.6 and 1.0 with a 60 μm thickness.

II.3 - BULK MATERIAL

As far as we know, only SAT and the Laboratoire de Physique des Matériaux (CNRS-Bellevue) have published their results on the growth of WBHCT material.

The growth method used by SAT is the THM. The THM principle is described elsewhere (12). A number of different materials have already been grown using this method (12), such as: Si, Si-Ge, GaP, as well as CdTe (13), (15), HgTe (15) and HgCdTe (15), (16). The main advantage of the THM is the fact that it permits the growth of the entire composition range from $x = 0$ to $x = 1$ without any major difficulty, including the problems encountered with mercury pressure.

Several papers (17 - 20) have been devoted to the THM process for the 8 - 12 μm , 3 - 5 μm and 1.3 - 1.6 μm spectral regions.

The following is a summary of the principal results achieved by SAT:

- Ingots currently produced are 60 mm in length, with diameters up to 40 mm;
- Growth is carried out at approximately 700°C at a rate of about 2.5 mm per day;
- Figs. 3a and 3b show a schematic representation of a growth run;
- Fig. 4 illustrates the typical longitudinal homogeneity profile as a function of cutoff wavelength measurement along the ingot;
- Figs. 5a and 5b illustrate the radial homogeneity as a function of spectral range and wafer diameter.

As a consequence of the higher cadmium concentration, single crystal ingots are not yet obtained for values of $x > 0.5$. With the small band gap material, single crystals up to 60 mm length are routinely grown.

III - PHYSICAL PROPERTIES

III.1 - CRYSTAL STRUCTURE

As described above, CdTe and HgTe are miscible in all proportions, leading to a continuous family of alloys which crystallize in a zinc blende cubic structure (34). Fig. 6 shows a zinc blende crystal lattice wherein the A atoms represent cations and the B atoms anions. Experimental data from WOOLLEY and RAY (35) indicate slight deviation of lattice constant from Vegard's law (see Fig. 7).

III.2 - THERMAL PROPERTIES

Most data on thermal properties found in the literature deal with narrow band gap material. However, due to the small differences between the properties of HgTe and CdTe, they provide a good approximation of the wide band gap material parameters.

III.2.1 - Phase diagram

Analytical expressions for the liquidus and solidus curves of the pseudo-binary diagram are given by SZOFRAN et al. (21) for DTA measurements:

$$x_L(T) = D_1 T^* + D_2 T^{*2} + D_3 T^{*3} + D_4 T^{*4}$$

$$x_S(T) = C_1 \sin\left(\frac{\pi}{2} T^*\right) + C_2 \sin\left(\frac{\pi}{2} \sqrt{T^*}\right) + C_3 \log(1+9T^*) + C_4 \sqrt{T^*}$$

wherein $T^* = (T - 670)/412$ with T in °C; the values of the constants are listed in the following table.

i	C_i	D_i
1	0.502804	0.607640
2	0.165390	0.077209
3	0.746318	0.696167
4	-0.413546	-0.381683

III.2.2 - Thermal expansion

Thermal expansion coefficients have been measured for HgTe (22), CdTe (23) and $\text{Hg}_{1-x}\text{Cd}_x\text{Te}$ (23) for $x = 0.2$ to $x = 0.3$. These results are listed in Table I. No data have been found for higher x -values.

A negative thermal expansion coefficient for liquid $\text{Hg}_{1-x}\text{Cd}_x\text{Te}$ has been determined through density measurements (22) for a temperature very close to the liquidus temperature for $x < 0.2$.

The melt density exhibits a maximum value with increasing temperature, this maximum being dependent on x . This abnormal behavior seems to be induced by the presence of mercury. Thus, the solid- to- liquid volume change $\frac{\Delta \rho}{\rho}$ indicates a near linear decrease with x , resulting in $\frac{\Delta \rho}{\rho} \approx 0$ in the 0.7 - 0.8 range, i.e.: solidification occurs with no change in volume for material in the 1 to 1.5 μm spectral region.

Compound	Thermal expansion coefficient
HgTe (22)	$6.68 \cdot 10^{-6} \text{ } ^\circ\text{C}^{-1}$ $25^\circ\text{C} < T < 670^\circ\text{C}$
CdTe (23)	$1.96 \cdot 10^{-6} \text{ } ^\circ\text{C}^{-1}$ $24^\circ\text{C} < T < 210^\circ\text{C}$
$\text{Hg}_{0.796}\text{Cd}_{0.204}\text{Te}$ (23)	$2.86 \cdot 10^{-6} \text{ } ^\circ\text{C}^{-1}$ $24^\circ\text{C} < T < 93^\circ\text{C}$
$\text{Hg}_{0.775}\text{Hg}_{0.225}\text{Te}$ (23)	$3.49 \cdot 10^{-6} \text{ } ^\circ\text{C}^{-1}$ $24^\circ\text{C} < T < 93^\circ\text{C}$
$\text{Hg}_{0.69}\text{Cd}_{0.31}\text{Te}$ (23)	$3.22 \cdot 10^{-6} \text{ } ^\circ\text{C}^{-1}$ $24^\circ\text{C} < T < 93^\circ\text{C}$

TABLE I

Thermal expansion coefficient from (22) and (23)

III.2.3 - Molar specific heat

The molar specific heat of a solid is given by L.R. HOLLAND (24), derived from data on CdTe and HgTe (25) by linear interpolation:

$$C_S (x,T) = 52.06 - 12.036 x + (9.06 + 23.95x) T/1000 \text{ J mol}^{-1}\text{°C}^{-1}$$

No data are available for the molar specific heat of the liquid.

III.2.4 - Thermal conductivity

The thermal conductivity variation for x and T has been established by V. ALEXIADES et al. (26) from values of HOLLAND (24) and reported in Table II for x < 0.3 with data from POPPENDIEK (23).

III.3 - MECHANICAL PROPERTIES

Only sketchy information about the mechanical properties of HgCdTe alloys is available (27), (28).

We performed microhardness measurements (19) and these results are presented in Fig. 8. They are in good agreement with those of the literature, although secondary maxima are not observed. All the curves show a maximum for x \approx 0.75 (1 atom of Hg for 3 atoms of Cd). The hypothesis of a metallic lattice order has been suggested but it still remains unverified. It can be noticed that the 1 to 2 μm spectral range (x = 0.5 to 0.9) corresponds to the highest hardness of the solid solution.

We noticed a difference between the hardness of the two faces A and B in the case of (111) orientation, like in III-V compounds (29). In HgCdTe alloys the metallic face is harder than the metalloid face ($\frac{\Delta H}{H} \sim 5\%$ to 10%), independent of the material composition. H

In contrast to GaAs where the harder face depends on the type (29), such an inversion between the N- and P-type is not observed with HgCdTe.

TEM observations of dislocations have been conducted (28) following uniaxial deformation, which led to conclusions about the deformation mechanism (Peierls mechanism). The strain-stress behavior of $\text{Hg}_{0.34}\text{Cd}_{0.66}\text{Te}$ is quite similar to that of the Group IV and III-V compounds.

Liquid Hg_{1-x}Cd_xTe (26)

$$k_L = 1.2 \cdot 10^{-2} [B(x) - \ln T - A(x)]$$

$$\begin{aligned} \text{wherein } A(x) &\approx 58.499034 - 79.4574x \\ B(x) &\approx 9.085703 - 12.741994x \\ 0 &< x < 0.31 \end{aligned}$$

Solid Hg_{1-x}Cd_xTe (26)

$$k_S = [1.276 - 0.295x + (0.222+0.587x) \frac{T}{1000}] a_S(x, T)$$

$$\text{wherein } a_S(x, T) =$$

$$10^{-2} x [A_0(x) - A_1(x) \frac{T}{10^3} + A_2(x) \frac{T^2}{10^6} - A_3(x) \frac{T^3}{10^9}]$$

$$A_0(x) \approx 2.305915 - 5.050485x$$

$$A_1(x) \approx 8.33024 - 14.938646x$$

$$A_2(x) \approx 17.472562 - 24.771145x$$

$$A_3(x) \approx 13.068309 - 17.96172x$$

Solid Hg_{1-x}Cd_xTe (23)

$$x = 0.204 \quad k_S = 2.10^{-2} \text{ J s}^{-1} \cdot \text{cm} \cdot ^\circ\text{C}$$

$$x = 0.31 \quad k_S = 1.71^{-2} \text{ J s}^{-1} \cdot \text{cm} \cdot ^\circ\text{C}$$

$$x = 1.0 \quad k_S = 3.97^{-2} \text{ J s}^{-1} \cdot \text{cm} \cdot ^\circ\text{C}$$

TABLE II: Thermal conductivity parameters

IV - ELECTRONIC PROPERTIES AND BAND STRUCTURE

IV.1 - BAND GAP ENERGY VARIATION

For wide band gap material ($x > 0.5$) the most accurate relationship between E_g , x and T deduced from our recent data (36) is:

$$E_g(x, T) = -0.303 + 1.94x - 0.655x^2 + 0.579x^3 \\ + (5.5 - 13.92x + 5.84x^2)10^{-4}T \quad (\text{eV})$$

The band gap temperature coefficient calculated from this relation (see Table III) indicates very low values in this composition range and even a quasi-invariance of the band gap with temperature near the $2 \mu\text{m}$ wavelength (see Fig. 9). These data have been confirmed through electro-reflectance measurements in the 100 to 300 K temperature range (see para. V.2).

$\lambda_c (\mu\text{m})$	x	$E_g(\text{eV})$ $T=300 \text{ K}$	$\frac{dE_g}{dT} (\text{eV K}^{-1})$
1	0.89	1.24	$- 2.10^{-4}$
1.35	0.72	0.92	$- 1.5.10^{-4}$
1.6	0.63	0.77	$- 0.9.10^{-4}$
2	0.53	0.62	$+ 0.2.10^{-4}$

TABLE III
HgCdTe band gap parameters

IV.2 - BAND STRUCTURE

The band structures of CdTe and HgTe have been calculated by many authors (37), (38). They are illustrated in Figs. 10 and 11.

The band structure of $\text{Hg}_{0.3}\text{Cd}_{0.7}\text{Te}$, as determined by HASS (39) is described in Fig. 12.

Electro-reflectance measurements have confirmed the presence of an energy level in relation with the spin orbit band. This value Δ_o (split-off energy) has been studied (40), (41), (36) in relation to the band gap energy (Fig. 13). This figure points out a composition range where $\Delta_o \approx E_g$. It is located for x-values between 0.6 and 0.7, i.e.: for wavelengths between 1.3 μm and 1.6 μm , as shown in Table IV.

λ_c (μm)	x	E_g (eV)	Δ_o (eV)	Δ_o/E_g
1	0.89	1.24	0.81	0.65
1.35	0.72	0.92	0.81	0.65
1.6	0.63	0.77	0.81	1.05
2	0.53	0.62	0.81	1.30

Table IV
Band structure parameters

In this composition range ($0.6 < x < 0.7$) impact ionization phenomena will be enhanced. the ionization coefficient ratio of holes and electrons $K = \frac{\beta}{\alpha}$, especially, will be high (42).

This condition is essential for the development of low-noise avalanche photodiodes (43) and it has been verified experimentally on photodiodes fabricated in SAT's laboratories (44).

IV.3 - INTRINSIC CARRIER CONCENTRATION

Effective masses have been calculated for the four bands: conduction, heavy hole, light hole and split-off) (37), (45) and they are listed in Table V for $x = 0.6$ and $x = 0.7$.

Composition	m_e^*	m_{hh}^*	m_{lh}^*	m_{so}^*
$\text{Hg}_{0.3}\text{Cd}_{0.7}\text{Te}$	$0.008 m_0$	$0.55 m_0$	$0.17 m_0$	$0.145 m_0$
$\text{Hg}_{0.4}\text{Cd}_{0.6}\text{Te}$	$0.058 m_0$	$0.55 m_0$	$0.16 m_0$	$0.145 m_0$

TABLE V
HgCdTe effective masses

In consideration of low electron effective mass, low intrinsic concentration will be expected.

From these values and using the following equation, we get:

$$n_i = 4.9 \cdot 10^{15} \left(\frac{m_e^*}{m_0^*} \frac{m_{hh}^*}{m_0^*} \right)^{3/4} \cdot T^{3/2} \cdot \exp(-E_g/kT)$$

$$\text{for } T = 300 \text{ K, and } x = 0.7 : n_i \approx 4 \times 10^{10} \text{ cm}^{-3}$$

The following two semi-empirical equations have been proposed to calculate n_i :

$$n_i(x, T) = \frac{1.265 \cdot 10^{16} \cdot T^{3/2} (6+x)^{-3/2} E_g^{3/2}}{1 + \left[1 + 19.4 (6+x)^{-3/2} \frac{m_e^* E_g^{3/2}}{m_0^*} \exp \frac{E_g}{kT} \right]^{1/2}} \quad (46)$$

and (47):

$$n_i(x, T) = (1.093 - 0.296x + 4.42 \cdot 10^{-4} T) 5.16 \cdot 10^{14} (E_g)^{3/4} T^{3/2} \exp \frac{-E_g}{2kT}$$

The variations of n_i with x and T are shown in Fig. 14 and in table VI for $T = 300$ K.

x	0.89	0.72	0.63	0.53
$\lambda_c (\mu m)$	1	1.35	1.6	2
$n_i (cm^{-3})$	$2 \cdot 10^8$	$3 \cdot 10^{10}$	10^{12}	10^{13}

TABLE VI
HgCdTe intrinsic carrier concentration vs. x -composition

IV.4 - MOBILITY

Electron mobility vs. composition for carrier concentrations less than $2 \times 10^{15} cm^{-3}$ is shown in Fig. 15 from SCOTT (48), while hole mobility in the same composition range is about 50 to 100 $cm^2 V^{-1} s^{-1}$.

SAT's experimental data at 300 K and 77 K are illustrated in Figs. 16 and 17 and in Table VII. Electron mobility at 300 K varies between 1,000 $cm^2 V^{-1} s^{-1}$ and 2,000 $cm^2 V^{-1} s^{-1}$ for $0.5 < x < 0.8$. These results are in good agreement with Scott's data (48).

Other works (30) reporting on the same material show that the variation of electron mobility with temperature exhibits a maximum in the 30 to 50 K range and that the R_H value depends on the annealing temperature. For treatment temperatures between 250°C and 400°C the donor concentration increases with temperature and involves both residual impurities and native defects, while at temperatures in excess of 400°C the material remains P-type.

T (K)	x	P-type		N-type	
		Carrier concentration (cm ⁻³)	Mobility μ_1 (cm ² V ⁻¹ s ⁻¹)	Carrier concentration (cm ⁻³)	Mobility μ_1 (cm ² V ⁻¹ s ⁻¹)
300	0.5	10 ¹⁵ - 2.10 ¹⁷	400 - 50	3.10 ¹⁴	2,000
	0.6	10 ¹⁵ - 5.10 ¹⁶	80 - 50	3.10 ¹⁴	1,200
	0.7	8.10 ¹⁴ - 5.10 ¹⁶	60 - 30	3.10 ¹⁴	1,000
77	0.2	10 ¹⁶ - 4.10 ¹⁷	600 - 200	2.10 ¹⁴	150,000
	0.3	5.10 ¹⁵ - 2.10 ¹⁷	600 - 200	2.10 ¹⁴	60,000
	0.5	10 ¹⁵ - 10 ¹⁷	100 - 50	3.10 ¹⁴	10,000
	0.6	-----	-----	4.10 ¹⁴	5,500
	0.7	-----	-----	4.10 ¹⁴	4,000

TABLE VII

Carrier concentration and mobility as a function of different x-values for N- and P-type material

V - OPTICAL PROPERTIES

V.1 - TRANSMISSION NEAR THE BAND GAP

Experimental values of the absorption coefficient were determined through transmission measurements with a dual-beam Perkin Elmer model 983 spectrophotometer. Due to the steep increase of the absorption coefficient with increasing wavelength (Fig. 18) it has been necessary to reduce the thickness of the sample down to 0.7 μm in order to obtain reliable absorption data in the band-to-band absorption region (Figs. 19 - 20).

By applying the usual k.p theory, the absorption coefficient may be computed from the band structure parameters, using the equation:

$$\alpha = e^2 \pi^3 P^2 (1 - E_g / h\nu)^{1/2} (4\pi\lambda\epsilon_0)^{-1}$$

the relation of P to the interband absorption matrix element is:

$$P = -i(\hbar/m_0) \langle S | P_x | x \rangle \quad (P = 8 \times 10^{-8} \text{ eV cm})$$

ϵ_0 = dielectric permittivity

This equation is accurate for photon energies above the band gap energy. In the vicinity of the absorption edge it would be necessary to take into account the role of the elementary excitations, such as phonons and excitons.

As illustrated in Fig. 21 and Table VIII, the absorption coefficient is greater than 10^4 cm^{-1} in the wavelength range used in a photodetector. Therefore, the layer may be as thin as a few micrometers.

V.2 - ELECTRO-REFLECTANCE NEAR THE E_g TRANSITIONS

Relative changes in reflectivity vs. temperature are shown in Fig. 22, evidencing a very low temperature coefficient for the band gap dE_g/dT on the order of $2 \times 10^{-5} \text{ eV K}^{-1}$ for an x-composition of 0.6 (49).

Such a low value is a unique feature and an important advantage of the HgCdTe family.

As a consequence, a photodiode will always have a well-adjusted maximum wavelength of detectivity with no, or few changes as a result of room temperature variations. In an electro-luminescent device the emission wavelength will equally incur very few changes with temperature variations.

Parameter (Units)	HgTe $x = 0$	Hg _{1-x} Cd _x Te $x = 0.6$ $x = 0.7$		CdTe $x = 1$
E_g , opt. (eV)	-	0.8	0.9	1.5
ϵ_{static}	20	13.4	12.5	10.6
ϵ_{∞}	17	9.4	8.3	7.2
n	3.74	3.0	2.88	2.7
α at λ_{max}	-	10^4	10^4	

Table VIII
Main optical parameters of Hg_{1-x}Cd_xTe alloys (T = 300 K)

V.3 - MEDIUM AND FAR INFRARED TRANSMISSION

Far below the edge of the band, the absorption coefficient arises out of several processes:

- phonon absorption around the 300 cm^{-1} wavenumber;
- free carrier absorption as a function of carrier concentration;
- intravalence band absorption in the medium infrared region.

At the shorter wavelengths, N- and P-type materials differ significantly.

In the P-type material, due to the proximity of the Fermi level to the valence band, light hole-band to heavy hole-band transitions are observed. Depending on the composition, the modeling of this absorption mechanism may be performed using a parabolic or non-parabolic band structure (Figs. 23-24). In both cases, higher order k terms must be used in the energy vs. k expansion (51). The variation of the absorption with hole concentration is linear in a wide range of concentration (far from band degeneracy) and therefore presents a convenient method to measure hole concentration with a contactless technique (Figs. 25-26).

In N-type materials, electron-free carrier absorption prevails. However, due to band non-parabolicity, it follows a $\lambda^{2.5}$ to λ^3 law (52). The height of the term level rules out the intervalence absorption mechanism. As usually observed in II-VI compounds, the absorption coefficient in the medium infrared region may be as low as 10^{-5} to 10^{-4} cm^{-1} in low-doped N-type material.

VI - ADVANTAGES OF WIDE BAND GAP HgCdTe

In addition to epitaxial techniques, HgCdTe alloys may be produced in bulk ingots using the THM process. This method is now yielding large diameter ingots in the $x = 0.5$ to $x = 0.8$ composition range with high longitudinal and radial homogeneity for large area detector processing.

The resonance between the forbidden band and the spin-orbit band in the 1.3 to $1.5\text{ }\mu\text{m}$ wavelength region and the ensuing high β/α ratio (> 10) resulting from the ionization coefficients in the three bands, is beneficially implemented in the fabrication of low-noise APDs. In the $2\text{ }\mu\text{m}$ wavelength range, the CCCH ionization which favors electron multiplication ($\beta/\alpha < 0.1$) is utilized to obtain a similar gain improvement in the photodetectors.

Moreover, the low value of the band gap temperature coefficient permits the operation of these devices in a wide temperature range with negligible impact on their spectral characteristics. The following table summarizes the principal characteristics of $\text{Hg}_{0.3}\text{Cd}_{0.7}\text{Te}$, as compared to other materials used in the fabrication of photodetectors in a similar wavelength region.

	HgCdTe	InGaAs	Ge
n_i (300 K)	$3 \cdot 10^{10} \text{ cm}^{-3}$	10^{12} cm^{-3}	$2.3 \cdot 10^{13} \text{ cm}^{-3}$
$dE_g/dT (\text{eVK}^{-1})$	$-1.5 \cdot 10^{-4}$	$-3.7 \cdot 10^{-4}$	$3.7 \cdot 10^{-4}$
$K = \beta/\alpha$	10	0.3	1

VII - ADVANTAGES OF HgCdTe AVALANCHE PHOTODIODES

The advantages of HgCdTe avalanche photodiodes are directly related to the band structure (see IV.2). The multiplication and noise properties associated with these avalanche diodes, as generally applicable, are described in (53) and (54) and, with particular reference to HgCdTe, in VII.1 below.

VII.1 Gap-spin orbit resonance

The multiplication process initiated by holes may be broken down into 5 stages (Fig. 27):

- 1 - Absorption of a photon and creation of a hole in the valence band (Fig. 27a),
- 2 - the hole is accelerated by the action of a strong electrical field (Fig. 27b),
- 3 - the hole travels from the light hole band to the split-off band at the edge of the band with k (wave vector) practically constant (Fig. 27c),
- 4 - hole relaxation (Fig. 27d),
- 5 - Auger effect reciprocal to k (wave vector) = 0. The hole gives off its energy by creating a new pair of carriers. A new cycle may start over.

The hole and electron ionization coefficients follow an exponential law which approximates a Boltzmann function

$$\alpha_n, \beta_p \approx \exp \left(- \frac{E_i}{q\lambda_{LO}E} \right)$$

wherein λ_{LO} is the average distance covered by a carrier before interacting with one phonon. E is the electrical field.

E_i represents a threshold energy which corresponds to the minimum energy necessary to create an ionizing shock. In the case where $E_g \gg \Delta_o$, and for the holes:

$$E_i = E_g \left[1 + \frac{m_{so}^* (1 + \Delta_o / E_g)}{2m_{hh}^* + m_e^* - m_{so}^*} \right] \quad (55)$$

wherein m_{so}^* , m_{hh}^* and m_e^* represent the reduced masses of the spin-off holes, the heavy holes and of the electrons, respectively.

In the above equation, when $E_g = \Delta_o$, E_i becomes minimal and equals E_g . The hole ionization coefficient thus reaches a maximum.

To this date no study has permitted the experimental observation of this resonance effect. Only two published papers based on theoretical calculations (56), (57) have proven that

$$0.8 < \Delta_o < 0.9 \text{ eV}$$

VII.2 - Description of the photodiode

VII.2.1 - Technology

The HgCdTe avalanche photodiodes which respond to 1.3 and 1.55 μm radiation are developed in the SAT laboratories (58).

The principal operations of the fabrication process are summed up as follows:

- Fine polishing of the wafer surface with abrasive alumina, followed by chemo-mechanical etching.

- Deposition of dielectric layers by sputtering, opening of the diffusion windows by photo-lithography and chemical etching. These windows will be used for the diffusion of the guard rings.

- Forming of the N-type guard rings by mercury diffusion at 300°C.

- Sputtering of dielectric layers and opening of diffusion windows for creating the sensitive diode area.

- Forming of the $N^+/N/P$ structure by ion implantation (60 keV, $5 \times 10^{14} \text{ cm}^{-2}$ dose), followed by mercury diffusion to form the N-region.

- Deposition of dielectric layers by sputtering for the purpose of:

- passivation against ambient atmosphere;
- providing an anti-reflection coating at the 1.3 and 1.55 μm wavelengths.

- Metallization of the N-contact by platinum-gold sputtering through the openings in the dielectric layers.

- Chemical processing and metallization of the rear face for the P-contact.

- General passivation by SiO_2 sputtering.

VII.2.2 - Photodiode structure

A cross-sectional illustration of the diode structure is shown in Fig. 28a and in the photograph of Fig. 28b by an image of the induced current. The guard ring has a typical depth of 6 to 8 μm .

VII.2.3 - Purpose of the guard ring for avalanche structures

The purpose of this guard ring is to minimize the risk of breakdown in areas where the electrical field reaches its maxima, such as in the vicinity of the smaller radii of curvature of the space charge region or near the substrate surface.

In the photograph of Fig. 29 which was taken by electron microscope in the "induced current" mode, the frequent breakdown at the edge of the junction is visible on a structure without guard ring.

Fig. 30 shows a photodiode provided with a guard ring, wherein only the central portion of the junction is subjected to the avalanche multiplication phenomenon. It is this ring which is responsible for most of the non-multiplied dark current (I_d).

VII.2.4 - Modeling of the avalanche photodiode

Fig. 31 represents the schematic cross-section of the junction. The typical junction depth x_j is 3 μm . It was determined experimentally by a parametric study of the diode sensitivity (the junction depth was measured by electron microscopy in the induced current mode on cleaved diodes). The N^+ -region is created by ion implantation. The transition between the N^+ - and N-regions takes place within about 0.3 μm of the surface.

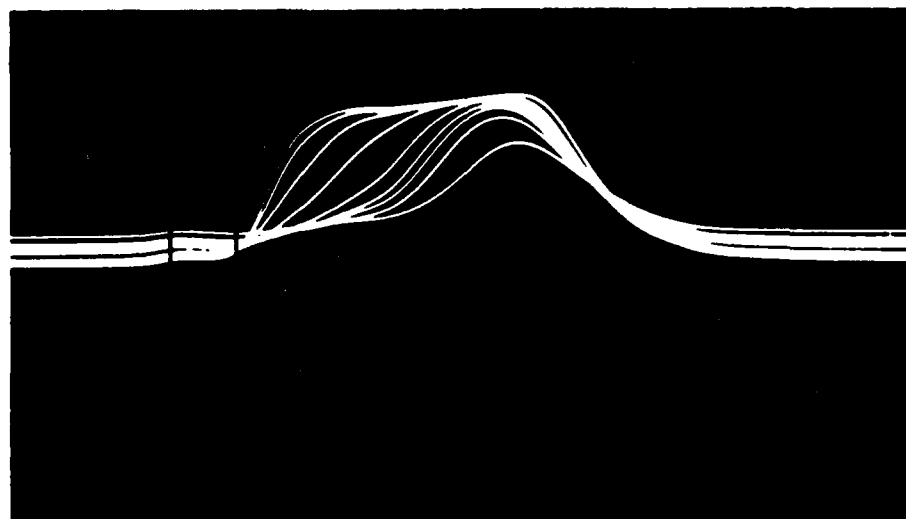
The doping profile was determined very accurately by Valenza (59), through capacitance measurements under variable bias voltage for the N-region and through calculations for the N^+ -region. The resulting doping profile is shown in Fig. 32. It shows that this profile is gradual up to a thickness of the depleted region of about $1\text{ }\mu\text{m}$ around x_j .

The average concentration gradient obtained by $C(V)$ is about $7 \times 10^{19}\text{ cm}^{-3}\text{ }\mu\text{m}^{-1}$, which agrees with other values previously published (60), (61).

Since the doping of the N-region is weaker than that of the P-region, the increase of the space charge region, depending on the bias, favors the N-side. A few volts of reverse bias suffice for this depleted region to touch the N^+ -region, from where it extends slightly to the P-side.

Starting from this model, Valenza reconstructed the numerical values of the $C(V)$ of the photodiode and reached almost perfect agreement with the experimental values of $C(V)$.

We were able to observe with the electron microscope in the induced current mode the effective expansion of the depleted region (see illustration below).



Expansion of the space charge zone

The ordinate in this photograph represents the amplitude of the induced signal into the junction by the scan of the electron microscope. The abscissa shows the junction depth with respect to the surface. At about -10 V , the N-region is practically depleted. The expansion to the P-side is virtually nil (the picture is that of a cleaved diode).

Valenza also calculated the electrical field in the junction. Fig. 33 shows the distribution of the field as a function of the abscissa x . One observes that the electrical field is practically constant over about a $2 \mu\text{m}$ zone which behaves like an intrinsic region. The maximum value of the electrical field at breakdown is $4 \times 10^5 \text{ V cm}^{-1}$, which is additional proof of agreement with the other results (60), (61).

VII.3 - Diode Characterization

The diodes are encapsulated in a hermetically sealed housing for the measurement of the following characteristics:

VII.3.1 Dark current characteristics $I(V)$, $C(V)$

- $I(V)$

A test bench with a picoammeter and a computer permits the measurement of the $I(V)$ characteristics and to make the following calculations:

- the avalanche voltage, which will be useful for measurements in the multiplication mode;
- the saturation current I_s ;
- the zero volt resistance R_{V0} ;
- the diode factor β

A typical $I(V)$ characteristic is shown in Fig. 34.

- $C(V)$ - see Fig. 35

VII.3.2 Characteristics under illumination

- Spectral response

A spectral response sample is illustrated in Fig. 36.

- Quantum efficiency and multiplication

The radiation source consists of a LED operating at $1.3 \mu\text{m}$, modulated at 1 kHz, with adjustable optical power for the measurements at low frequencies with a low photocurrent (about 100 nA). A lens pair (responding at $1.3 \mu\text{m}$) permits focusing of the emitted radiation (beam diameter $\approx 30 \mu\text{m}$).

The quantum efficiency of HgCdTe diodes is determined by comparison with a Ge diode calibrated at $1.3 \mu\text{m}$. The voltage for which $M = 1$ is selected arbitrarily at -20 V. The N-region is then completely depleted.

Following this operation, the LED is adjusted for a primary photocurrent on the order of 100 nA. Next, the curve $I_{\text{rad}} \sim f(V)$ is recorded (Fig. 37). The breakdown voltage V_{BV} appears at about -83 V for the diode shown in the example.

The quantum efficiency of the device is about 70%. A maximum multiplication of 22 is obtained for $V \sim V_{\text{Bias}}$, in which case the dark current (I_d) is about 60 nA.

For V_{Bias}	-73 V:	$M \sim 2$	$I_d \sim 20$ nA
For V_{Bias}	-78 V:	$M \sim 3$	$I_d \sim 30$ nA
For V_{Bias}	-80.5 V:	$M \sim 5$	$I_d \sim 40$ nA
For V_{Bias}	-82 V:	$M \sim 10$	$I_d \sim 50$ nA

• Mapping under illumination

The benefit of this characterization is threefold:

- it ensures the absence of microplasmas;
- it ensures the efficiency of the guard ring;
- it permits control of gain homogeneity (sorting).

Mapping under radiation provides the most accurate type of information because it is done under normal operating conditions. The radiation of a laser is focused (beam dia. about 20 μm) on the sample. A scan over one diameter permits to confirm the homogeneity of the sample. Fig. 38 shows the multiplication over the diameter of a homogeneous APD.

Nevertheless, the poor resolution of this experimentation has led us to consider a more accurate (and faster) characterization: multiplication of the induced current through SEM scan. The diodes are biased to $V_{\text{Bias}} \sim -3$ V and the electrons are accelerated at 15 kV.

Any existing microplasmas are clearly shown. Components with good and poor homogeneity can be clearly identified. At the present time this type of characterization is an indispensable tool in the selection of avalanche photodiodes.

Nevertheless, sorting by $I_d(V)$ for $I = 95 \mu\text{A}$ seems to be an efficient method for the elimination of components whose protection by the guard ring is inadequate and for APD's with microplasmas, as the diodes multiplying along the edges show very rapid deterioration.

On the other hand, inhomogeneities within the defined sensitive zone cannot, for the moment, be detected neither through biasing at high current nor through measurement of the dark noise (only microplasmas are revealed in the latter case) and testing with the SEM is the only efficient method for the sorting of APD's.

These inhomogeneities seem to be associated with the device processing as it has been confirmed that this peculiarity is characteristic of a given wafer (with noticeable differences between two wafers of a same ingot).

- Bandwidth

For a primary photocurrent with peak amplitude 1 μ A or less, the bandwidth of the HgCdTe APD is not affected by multiplication: $\tau_r \sim \tau_f \sim 450$ ps with $M = 1$ ($V = -20$ V) and $M = 10$ (V about -75 V). Hence, the speed of the detector is RC time-limited and not transit time-limited, as would be the case for a PIN diode.

Under higher illumination (> 10 μ W) saturation of the gain and bandwidth becomes evident as a result of unbiasing of the junction by the photocarriers.

VII.3.3 - Additional measurements: Noise

Three types of measurements were conducted:

- determination of the radiation noise in a 1 MHz bandwidth at 30 MHz;
- measurement of dark current and radiation noises at low frequencies;
- measurement of signal-to-noise ratio at 30 MHz and at higher frequencies.

- Multiplication noise of the optical signal

The schematic outline of the SAT measurement process is shown in Fig. 39.

The measured synchronous radiation noise (~ 1 kHz) is carried as a function of multiplication. The incident optical powers are on the order of 100 nW and focused on the detector (beam diameter: about 30 μ m). Fig. 40 illustrates the result obtained on a diode with a cutoff wavelength of 1.41 μ m. The approximation $F(M) = M^x$ is justified up to multiplication coefficients of 10. In the example shown $x \sim 0.45$ wherein $3 < M < 10$. Nevertheless, the analog measurement thus conducted does not ensure great accuracy of the result.

• Noise measurement at low frequencies

The experimental set-up, HgCdTe diode measurements and the most important analyses relating to the results have been published in (60): IEEE Transactions on Electron Devices, Vol. ED-32, No. 7, July 1985, 1302-1306. This publication confirms that $x \sim 0.5$ as well for the relative dark current noise multiplied as for the radiation noise. The ionization coefficient ratio is very close to 10.

VII.3.4 - Summary of the principal characteristics of 1.3 μ m HgCdTe APDs.

The best results and most typical results obtained are summarized in the table of Fig. 41.

VIII - INVESTIGATION AND FEASIBILITY OF LARGE AREA DETECTORS

VIII.1 Justification for extrapolation

One must remember that a photodiode is a current generator. The total generated current can be expressed by:

$$I_{\text{total}} = I_{\text{ph}} + I_{\text{diff}} + I_{\text{gr}} + I_{\text{tunnel}} + I_{\text{leakage(s)}}$$

wherein:

I_{ph} = photon flux current
 I_{diff} = diffusion current
 I_{gr} = generation-recombination current
 I_{tunnel} = tunneling noise
 $I_{\text{leakage(s)}}$ = leakage currents on the surface or around the junction, associated with the quality of the device processing technology.

The contribution of the tunneling current for the composition $x = 0.7$ is negligible.

Example of a diffusion mode

The saturation current I_s can be expressed as follows:

$$I_s = qAn_i^2 (L_p, L_n, \tau_n, \tau_p, \text{ carrier concentr.}) \exp(-E_g/kT)$$

wherein:

A = junction area

L_n, L_p, τ_n, τ_p = diffusion lengths and carrier lifetimes

In this case the dynamic resistance at zero bias (R_o) can be written as follows:

$$R_o = \frac{kT}{qI_s} \sim \frac{1}{n_i^2} \sim \exp(-E_g/kT)$$

This shows the importance of both the intrinsic properties of the material and of the technological device process which is found in the leakage term ($1/R_o A$). In turn, the leakage may have a number of different origins such as, above all: surface leakage and dielectric leakage (due to voltages which may reach 100 V, as shown) and leakage around the junction.

As a result, it can be shown that the quantity $R_o A$ must be related to the junction area geometry and that the only reasonable step to estimate the possibility of fabricating sensitive areas as large as 2 cm x 2 cm is to go through extrapolation of results obtained on a certain number of diodes of different diameters fabricated by SAT (0.080 mm, 0.250 mm, 1 mm, 2 mm and 5 mm).

VIII.2 Results achieved

Figs. 42 to 46 show the $I(V)$ characteristics of diodes of different sensitive areas (0.080 mm, 0.250 mm, 1 mm, 2 mm and 5 mm diameter). The respective junction areas are (cm^2):

$$1.3 \times 10^{-4}, 8 \times 10^{-4}, 102 \times 10^{-4}, 360 \times 10^{-4}, 2.2 \times 10^{-1}$$

Example of a generation-recombination mode

I_s is directly related to the value of the intrinsic concentration $I_s \sim n_i$

$$\text{and } R_o \sim \frac{1}{n_i} \sim \exp(-E_g/kT)$$

More generally speaking, the dark current I_d as a function of saturation current can be expressed as follows:

$$I_d = I_{sat} \left(\exp \frac{qV_c}{\beta kT} - 1 \right)$$

wherein V_c is the voltage at the ends of the transition zone and β a coefficient which represents the relative significance of various current contributors (=1 in the case only of diffusion mechanisms and = 2 in the case only of generation-recombination mechanisms).

$$\beta = \frac{R_o q I_s}{kT}$$

What has been stated about the saturation current level can also be stated for the quantity $R_0 A$.

$$\frac{1}{R_0 A} = \left(\frac{1}{R_0 A} \right)_{\text{diff}} + \left(\frac{1}{R_0 A} \right)_{\text{gr}} + \left(\frac{1}{R_0 A} \right)_{\text{tunnel}} + \left(\frac{1}{R_0 A} \right)_{\text{leakage}}$$

R_0 depends on the electrical characteristics of the semiconductor (concentration, lifetime, carrier diffusion length) and also on the impact of the device fabrication technology on the latter factors.

Each of these characteristics was measured at ambient temperature on diodes with a 1.55 μm wavelength. Figs. 47 to 50 show their characteristics (0.080 mm, 1 mm, 2 mm and 5 mm diameters). The totality of these characteristics permits to measure the saturation current of each diode. The results have been combined in Fig. 51 which thus permits the evaluation of the saturation currents that one may expect as a function of the diode area. This extrapolation supposes, of course, that we are dealing here with comparable technological processes and metallurgical characteristics.

VIII.3 - Measurements and advantages of low temperature operation

The high saturation currents obtained from large area diodes may reveal themselves to become a limiting factor for certain applications.

A diode of 5 mm diameter operating at the 1.55 μm wavelength was measured at eight different operating temperatures between -15 and +55°C. The I(V) characteristics at the temperature extremes are shown as examples in Figs. 52 and 53.

Fig. 54 combines different reverse characteristics for each temperature.

Fig. 55 shows resistance variations at zero bias R_{V0} as a function of temperature.

Fig. 56 shows the saturation current variations I_s as a function of temperature. These results lead us to the ^s immediate conclusion that considerable improvements may be expected for this parameter by lowering the operating temperature to a range between about -5°C and +25°C.

These are general results which may be of particular interest if one considers the use of larger diode sensitive areas.

IX - (HgCdTe) LIGHT EMITTING PROPERTIES

IX.1 - Introduction

Although laser emission has been observed in HgCdTe at various wavelengths under electronic or optical excitation, results with light emitting diodes disclosed low external emission yield (Figs. 57 and 58) (11), (36). This particularity may have intrinsic and extrinsic origins which are related to the very structure of the material or to the way the material is processed and the emitting device is fabricated.

Among the intrinsic reasons we may mention the ratio of non-radiative to radiative recombination processes which may vary with the band structure of the material and with the doping conditions. Also, the value of the minority carrier lifetime is strongly related to the band structure. The structure and processing of the device has a great impact on its external efficiency.

The following chapters will present a review of the phenomena which are of importance in these devices. In conclusion we establish that HgCdTe alloys are suitable materials for the fabrication of efficient light emitting diodes (LED), provided that a proper technology is developed for this type of application.

IX.2 - HgCdTe properties pertinent to LED processing

IX.2.1 - Recombination processes

The emission properties of LEDs are the result of the competition between radiative and non-radiative processes for minority carriers on both sides of a P-N junction. The radiative recombination rate must be higher or, at least, of the same order of magnitude as the non-radiative processes to get adequate external efficiency. Non-radiative processes arise mainly from deep impurity-induced recombination and from band-to-band Auger processes.

Radiative processes are technology-dependent and may be controlled through careful study of the device processing. At least, for material with x-composition lower than 0.8, the radiative processes have shown to be prevailing up to the point where the low value of E_g makes the Auger processes more dominant.

The Auger processes are strongly dependent on the band structure and they have been found to be quite different for electrons and holes.

The minority electron Auger recombination mainly involves the CCHC mechanism (62). The probability of this process increases when the forbidden band gap decreases. It is expected to be predominant only for low band gap materials under low injection rates, since under the same conditions the radiative band-to-band transition rate also increases.

The hole recombination through Auger mechanisms uses several processes involving mainly the light-hole valence band. The transition rates are higher than those for electrons under the same injection conditions. Furthermore, for LED emission in the 1.3 to 1.5 μ m wavelength region the spin-orbit split-off bands lead to resonant processes ($\Delta \approx E_g$) (42 - 44), resulting in short recombination times.

As a consequence, light emission in HgCdTe is more likely to occur from electron injection in the P-region of the LED. A peak in the emission dissymetry is observed in 1.3-1.5 μ m LEDs.

Besides the band-to-band radiative recombination, conduction band-to-acceptor level emission may be observed. Such radiative processes are less subject to reabsorption than the band-to-band mechanism although it may be expected to remain weak because of the low concentration levels obtained without drastic mobility reduction.

IX.2.2 - Self-absorption

The absorption coefficient is closely related to the band-to-band radiative processes. It depends mainly on the density of the states and on the optical transition matrix element.

In III-V and II-VI Group direct band gap semiconductors the k.p model may be used as a first-order approximation.

For the conduction band and the light hole band the effective masses may be computed by:

$$m_{e,h}^* \sim E_g / P^2$$

Since the joint density of state depends mainly on the effective mass of the lighter band and given the fact that the valence bands of corresponding II-VI and III-V compounds are roughly similar, the absorption coefficient may be expressed as:

$$K \sim m^{3/2} P^2 (E - E_g)^{1/2}$$

hence:

$$K \sim \frac{1}{P} (E - E_g)^{1/2}$$

In a first approach, the effective masses of the II-VI compounds are twice the corresponding effective masses of III-V compounds (i.e.: GaAs vs. CdTe), thus indicating a lower value of the intra-band matrix element. Therefore the absorption coefficient is larger at a comparable value of E_g .

As a result, the self-absorption mechanisms are more efficient in HgCdTe compounds.

IX.2.3 - Diode technology

From a technological point-of-view, the strong reabsorption observed in LEDs of the III-V Group, has been overcome by using heterostructures. HgCdTe exhibits the same possibility on account of the small lattice parameter mismatch observed between HgTe and CdTe. This indicates that epitaxial techniques would be suitable to develop a sandwich structure by coupling an active layer with another layer of lower refractive index to get both optical confinement and a limitation of reabsorption processes.

The last problem to consider in HgCdTe junctions is the higher value of residual resistivity, as compared to that obtainable in III-V compounds.

It results from the preceding that there is no fundamental problem in using HgCdTe as a basic material for LEDs, since the material properties are reasonably close to those of corresponding III-V Group materials.

The principal remaining drawbacks may be conquered by a properly adapted technology, since the whole composition range may be epitaxied owing to the small variation of the lattice parameter. In such a way the structure of the LED may be rendered similar to that of the III-V compound LEDs, with the same results for suitable heterostructures. The limiting wavelength in the infrared for such a device to operate may be the point where the Auger recombination processes become predominant, i.e.: for band gap energies lower than 0.3 eV.

X - CONCLUSIONS

Wide band gap mercury cadmium telluride has been grown using a low-temperature process: the Traveling Heater Method. The general properties, electrical as well as optical, of this new composition ($x = 0.6$ to 0.7) have been analyzed.

The behavior of this high cadmium content material is similar to the more conventional low- x material ($x = 0.2$ to 0.3): conversion from P- to N-type material by annealing with the N and P mobility strongly dependent on the composition.

Conventional N/P, PIN photodiodes for fiber optic communications at the 1.3 and 1.5 μm wavelengths are currently manufactured using this composition range. Different photodiode diameters were processed, from 0.080 mm to 5 mm. Extrapolated results from experimental measurements lead to a saturation current of about 1 μA for a 2×2 cm^2 photodiode at the 1.3 μm wavelength and operating at 300 K.

Radiative lifetime is expected in this wide gap material and therefore light emission is more likely to occur from electron injection in the P-type region of the junction. However, some technological limitations have to be surmounted before an efficient light emitting device is produced. A heterostructure is recommended to avoid strong reabsorption through the layer by using, for example, a low-temperature epitaxial process, such as MBE or MOCVD.

Furthermore, this wide gap material presents a particular band gap structure with a spin orbit energy close to the band gap energy. This produces a large hole ionization coefficient.

Material using this composition range is therefore suitable for the fabrication of low-noise avalanche photodiodes in the 1.3 to 1.5 μm wavelength region. Avalanche photodiodes, implementing a guard ring technology, have been fabricated during the period of this contract and delivered to DARPA for measurement.

LITERATURE CITED

- (1) M. ROYER, Lecture notes in Physics Vol. 133 W. ZAWADZKI, ed. Springer Verlag (1980)
- (2) M. CHU, C.C. WANG, J. Appl. Phys. 51 (4) (1980) 2255
- (3) M.CHU, S.H. SHIN, H.D. LAW, D.T. CHEUNG, Appl.Phys. Lett. 37 (3) (1980) 318
- (4) E. JANIK, M. FERAH, R. LEGROS. R. TRIBOULET, T. BROSSAT Y. RYANT, J. Cryst. Growth 72 (1985) 133
- (5) G.T. JENKINS, J. THOMPSON, M.J. HYLIANDS, K.T. WOODHOUSE, V. VINCENT, Proceedings SPIE Conference, Cannes, France, (1985), vol. 587 p.76
- (6) J. TUNNICLIFFE, S.J.C. IRVINE, O.D. DOSSER, J.B. MULLIN, J. Cryst. Growth 68 (1984) 245
- (7) S.J.C. IRVINE, J.TUNNICLIFFE, J.B. MULLIN, Mat. Letts. 2 (1984) 305
- (8) K. NISHITANI, R. OHKATA, T. MURATONI, J. Electron Mat. 12 (3) (1983) 619
- (9) F. BAILLY, C.R. Acad. Sci. Paris, 262 (1966) 635
- (10) F.BAILLY, Y. MARFAING, G. COHEN-SOLAL. J. MELNGAILIS, J. Phys. 28 (1967) 273
- (11) T. BROSSAT, A. AZEMA, J. BOTINEAU, F. RAYMOND, Proceedings SPIE Conference, Cannes, France (1985), Vol. 588 p.111
- (12) C.H.L. GOODMAN, Crystal Growth, Theory and Techniques, Vol. 1, Plenum Press, London, England (1974)
- (13) R. TRIBOULET, Y. MARFAING, J. Cryst. Growth 51 (1981), 89
- (14) R. TRIBOULET, Rev. Phys. Appl. 12 (1977), 23
- (15) R. TRIBOULET, D. TRIBOULET, G. DIDIER, J. Cryst Growth, 38 (1977) 82
- (16) R. UEDA, O. OHTSUKI, K. SHINOMARA, Y. UEDA, J. Cryst. Growth 13/14 (1972) 668
- (17) R. TRIBOULET, T. N'GUYEN-DUY, A. DURAND, J. Vac. Sci. Technol. A, 3 (1) (1985) 95
- (18) T. N'GUYEN-DUY, J. MESLAGE, G. PICHARD, J. Cryst. Growth 72 (1985) 490

- (19) A.DURAND, J.L. DESSUS, T. N'GUYEN-DUY, Proceedings SPIE Conference, Innsbruck, Austria, (1986) vol. 659 p. 131
- (20) A. DURAND, J.L. DESSUS, T. N'GUYEN-DUY, Proceedings SPIE Conference, Cannes, France (1985) Vol. 587 p. 68
- (21) F.R. SZOFRAN, S.L. LEHOCZKY, J. Electron. Mat. 10 (6) (1981) 1131
- (22) D. CHANDRA, L.R. HOLLAND, J. Vac. Sci. Technol. A, 1 (3) (1983) 1620
- (23) H.F. POPPENDIEK, D.J. CONNELLY, C.M. SABIN, A.L. GIOIA, Geoscience Ltd., Final Report, Contract DARPA/MDA 903.83.C.0156 (1984)
- (24) L.R. HOLLAND, R.E. TAYLOR, J. Vac. Sci. Technol. A, 1 (3) (1983) 1615
- (25) K.C. MILLS, Thermodynamic Data for Inorganic Sulphides, Selenides and Tellurides, Butterworth, London, England (1974)
- (26) V. ALEXIADES, G.A. GEIST, A.D. SOLOMON, Martin Marietta Energy Systems, Inc., Report for US Department of Commerce, Contract DE-AC05- 84OR21400
- (27) J. PELLEGRINO, J.M. GALLIGAN, J. Vac. Sci. Technol. A, 3 (1) (1985) 160
- (28) J.F. BARBOT, G. RIVAUD, J.C. DESOYER, 14th Conf. Defects in Semiconductors, Paris, August 1986
- (29) P.B. HIRSH, P. PIROUZ, S.G. ROBERTS, P.D. WARREN, Phil. Mag (1985)
- (30) J. ZHANG, J.C. THUILLIER, Phys. Stat. Sol. (a) 77 (1983) 649
- (31) S. COLE, A.F.W. WILLOUGHBY, M. BROWN, J. Crystal. Growth 59 (1982) 370
- (32) B.B. SHARMA, S.K. METHA, V.V. AGASHE, Phys. Stat. Sol. a60, K 105 (1980)
- (33) BALGUROUA, KHABAROV, J. Soviet. Phys. 7 (1976) 943
- (34) D. LONG, "Energy Band in Semiconductors", J. Wiley & Sons, New York, U.S.A., 1968
- (35) J. C. WOOLLEY and B. RAY, J. Phys. Chem. Solids 13, 151, (1960)

- (36) M. ROYER, T. BROSSAT, P. FRAGNON, J. MESLAGE, G. PICHARD and T. N'GUYEN-DUY, Annales des Telecommunications 98 (1983) 62
- (37) S. KATSUKI and JUNIMUNE, J. of Phys. Soc. of Japan, Vol.31, No. 2 (1971)
- (38) R.D. GRAFT, J. Vac. Sci. Technol. of Japan, Vol. 21 (1982)
- (39) K.C. HASS, H. EHRENREICH and B. VELICKY, Physical Review B, Vol. 27 No. 2 (1983)
- (40) A. MORITANI, K. TANIGUCHI, C. HAMAGUCHI and J. NAKAI, J. Phys. Soc. of Japan, Vol. 34 (1973) 73
- (41) M. CARDONA, K.L. SHAKLEE and F.H. POLLACK, Physical Review Vol. 154 No. 3 (1967)
- (42) J. MESLAGE, G. PICHARD, M. FRAGNON, M. ROYER, T. N'GUYEN-DUY, C. BOISROBERT, D. MORVAN, SPIE Geneva, Switzerland (1983)
- (43) O. HILDEBRAND, W. KUEBART, K.W. BENZ and M.H. PILKUHN, IEEE J. Quantum Electronics, 17 (1981) 284
- (44) B. ORSAL, R. ALABEDRA, M. VALENZA, G. PICHARD and J. MESLAGE, J. Cryst. Growth 72 (1985) 496
- (45) P.W. KRUSE, Semiconductors and Semimetals Vol. 18 p. 10 (1981), Academic Press, New York, U.S.A.
- (46) E. FINKMAN, Y. NEMIROVSKY, J. Appl Phys. Vol. 50 (1979)
- (47) J.L. SCHMIT, J. Appl. Phys. Vol 41 No. 7 (1970)
- (48) M.W. SCOTT, J. Appl. Phys. No. 43, p. 1055 (1972)
- (49) C. ALIBERT, Universite des Sciences et Techniques du Languedoc, Montpellier, France (private communication)
- (50) C. VERIE, Advances in Solid State Physics, O. Madelung, ed. Pergamon Viewey Braunschweig, Germany, 1970 p. 11-12
- (51) T. BROSSAT, F. RAYMOND, J. Cryst. Growth 72 (1985) 280
- (52) T.N. CASSELMAN, G.L. HANSEN, J. Vac. Sci. Technol. A (1983) 1683
- (53) R.J. McINTYRE, "Multiplication Noise in Uniform Avalanche Diodes", IEEE Trans. on E.D., Vol. ED-13, No. 1, pp. 164-168
- (54) G.E. STILLMAN et C.M. WOLFE, "Avalanche Photodiodes", Semiconductors and Semimetals, Vol. 12, ed. Willardson & Beer, Academic Press, New York, U.S.A., 1977

- (55) C. VERIE, F. RAYMOND, J. BESSON, T. N'GUYEN-DUY, "Bandgap-Spin Orbit Splitting Resonance Effects in HgCdTe Alloys" Proc. Int. Conf. on II-VI compounds, Durham NC, U.S.A. Apr. 1982 (J. Cryst. Growth, supplement, Oct. 1982)
- (56) A. MORITANI, K. TANIGUCHI, C. HAMAGUCHI, J. NAKAI, Journal of the Physical Society of Japan, Vol. 34, NO. 1, Jan. 1973
- (57) C. N'GUYEN, C. HINNEN, R. TRIBOULET, P. LEMASSON, Journal of Crystal Growth, Vol. 72, (1985) p. 490
- (58) J.C. FLACHET, M. ROYER, Y. CARPENTIER, G. PICHARD, "Emission and Detection in the 1 to 3 μm Spectral Range with $\text{Hg}_{1-x}\text{Cd}_x\text{Te}$ Diodes" 2nd Int. Tech. Sympos. on Optical and Electro-Optical Applied Science and Engineering, Cannes, France, 25 Nov.- 6 Dec. 1985
- (59) M. VALENZA, "Caracterisation des photodetecteurs HgCdTe pour la detection a 1,3 μm ", Ph.D.Th., Universite des Sciences et Techniques du Languedoc, Montpellier, France, July 1985
- (60) R. ALABEDRA, B. ORSAL, G. LECOY, G. PICHARD, J. MESLAGE, P. FRAGNON, "A $\text{Hg}_{0.3}\text{Cd}_{0.7}\text{Te}$ Avalanche Photodiode for Optical Fiber Transmission Systems at 1.3 μm ", IEEE Trans. on E.D., Vol. ED-32, No. 7, July 85
- (61) R. ALABEDRA, B. ORSAL, M. VALENZA, L. BAYO, G. PICHARD, J. MESLAGE, C. BOISROBERT, "Photodiodes a Avalanche $\text{Hg}_{1-x}\text{Cd}_x\text{Te}$ avec $x = 0.6$ pour la Detection a 1,55 μm " OPTO'85, Paris, France, ESI Publications
- (62) P.E. PETERSEN, "Auger recombination in MCT", Semiconductors and Semimetals, ed. Willardson & Beer, Academic Press, New York, U.S.A., 1981

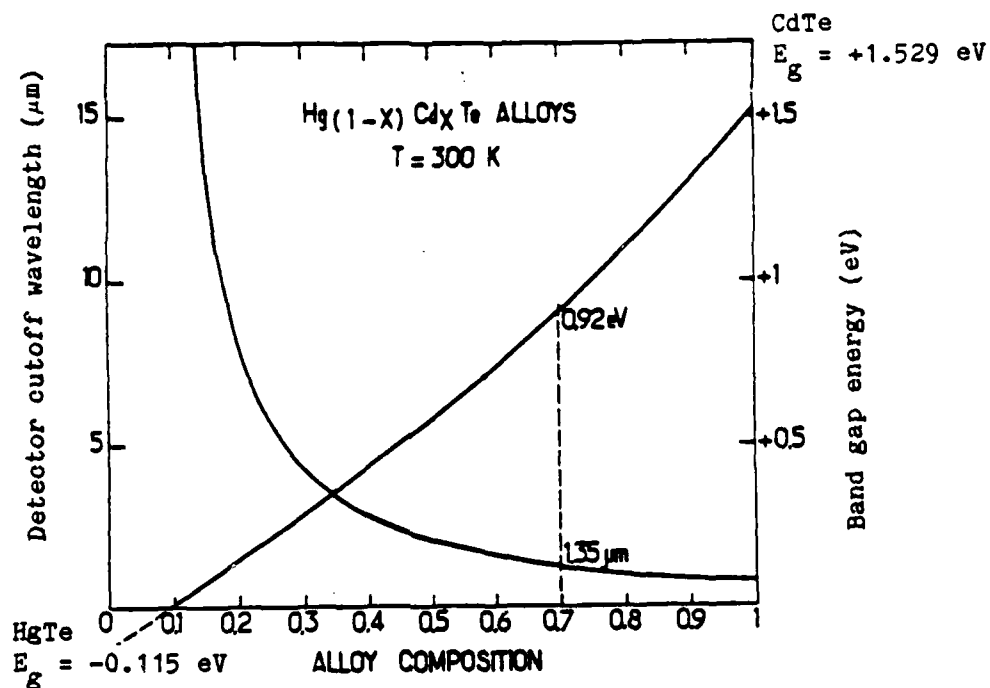


Fig. 1 Band gap energy and detector cutoff wavelength vs. composition

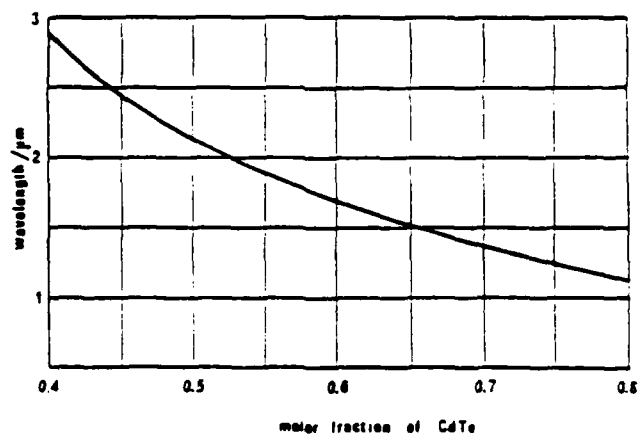


Fig. 2 Detector cutoff wavelength vs. composition in the 1 - 2 μm spectral wavelength region

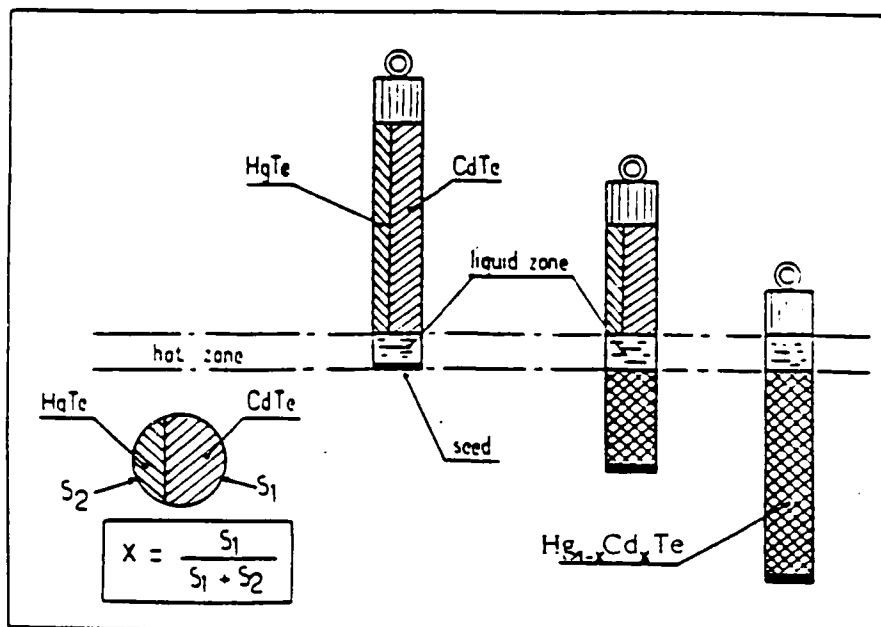


Fig. 3a Principle of THM process

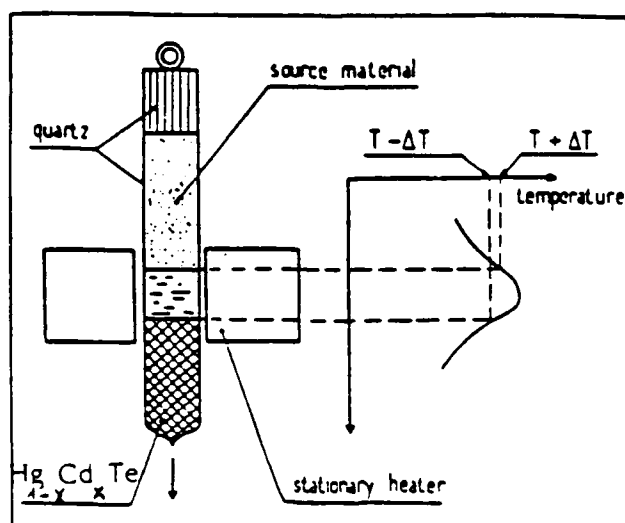


Fig. 3b Steps of a THM growth run

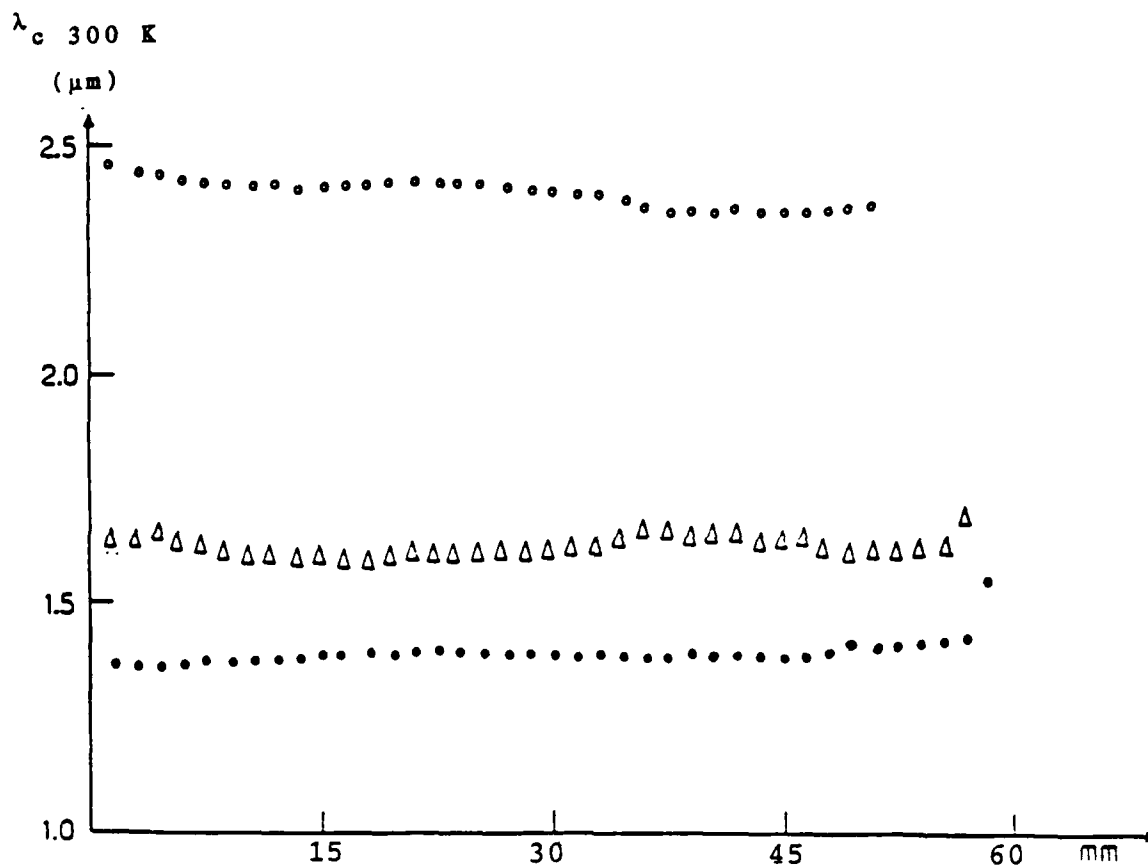


Fig. 4 Longitudinal homogeneity of three THM-grown ingots as a function of detector cutoff wavelength

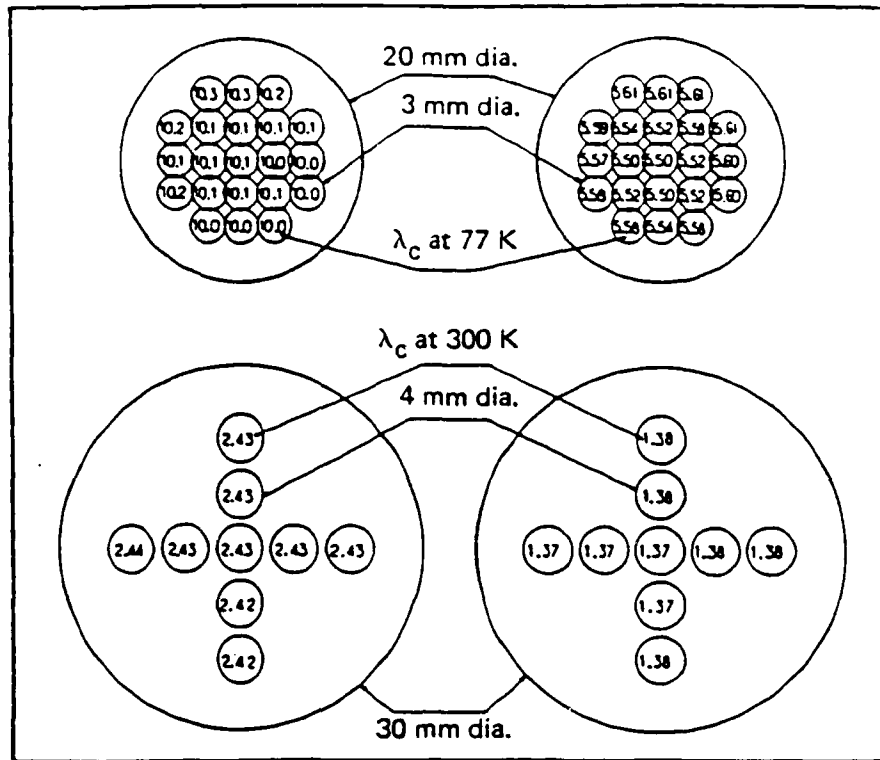


Fig. 5a

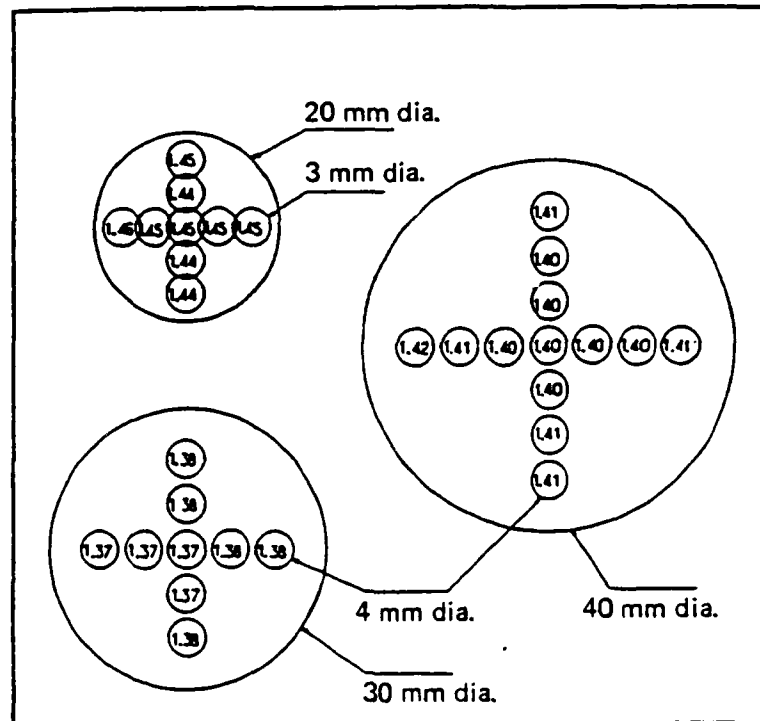


Fig. 5b

Figs. 5a and 5b Radial homogeneity of THM wafers (expressed in terms of detector cutoff wavelengths) for different wafer diameters

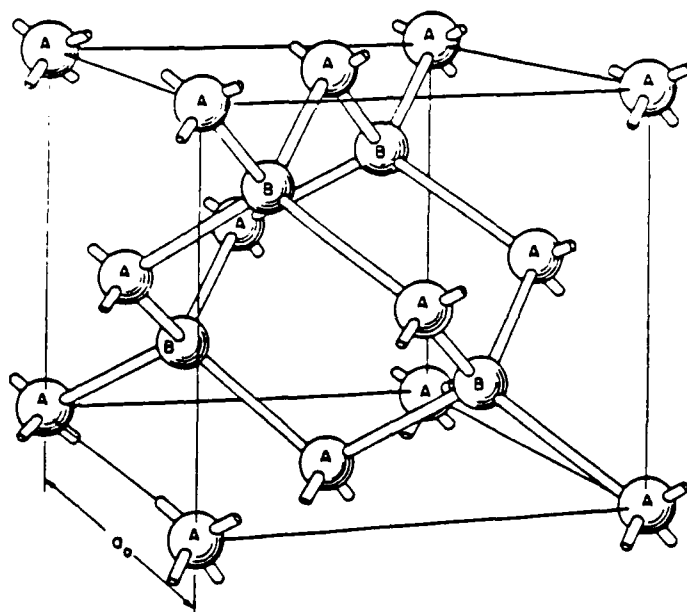


Fig. 6 Zinc blende crystal lattice (after Long (34))

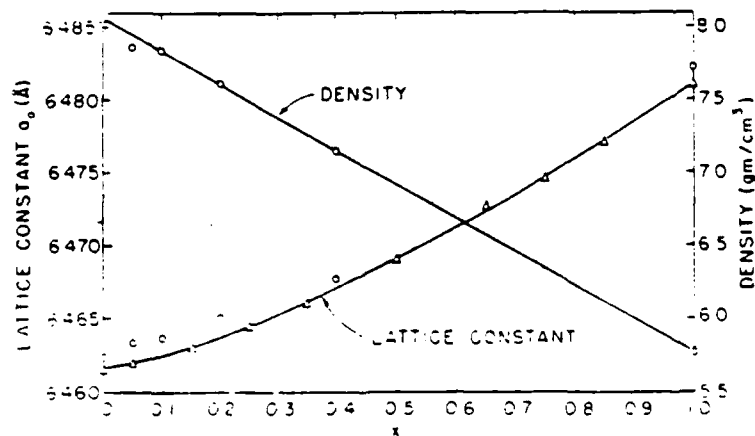


Fig. 7 Lattice constant and density vs. composition

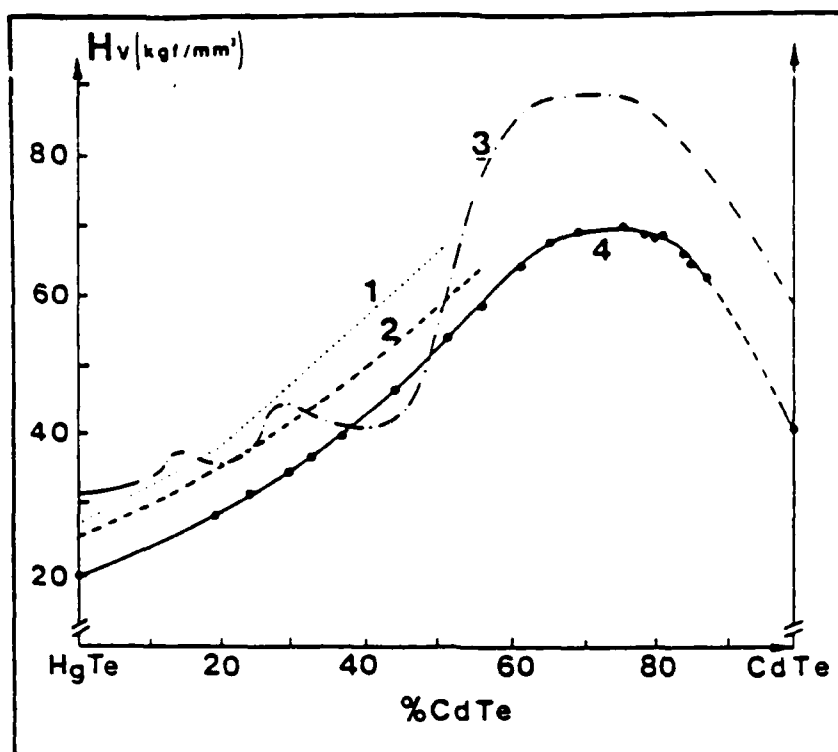


Fig. 8 Microhardness vs. composition for $\text{Hg}_{1-x}\text{Cd}_x\text{Te}$ from:
 1 - COLE (31) 2 - SHARMA (32)
 3 - BALAGUROVA (33) 4 - DURAND (19)

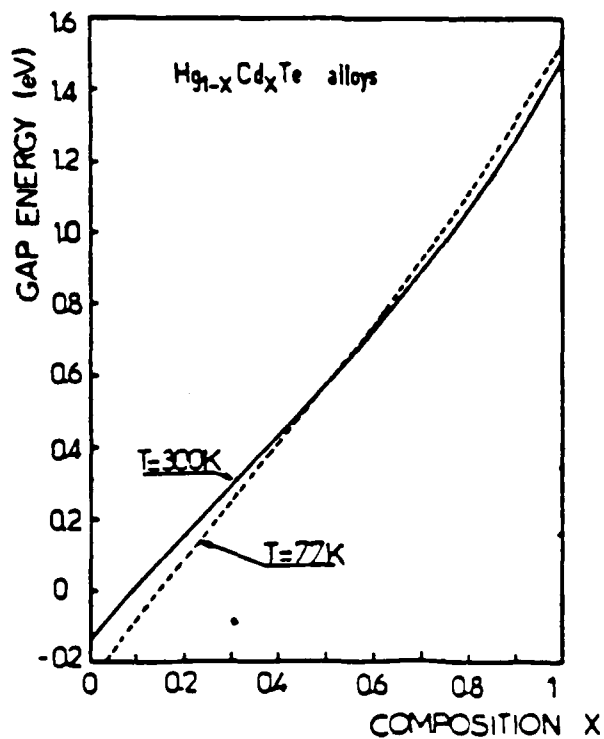


Fig. 9 Variation of gap energy vs. composition
 for $T = 300\text{ K}$ and $T = 77\text{ K}$

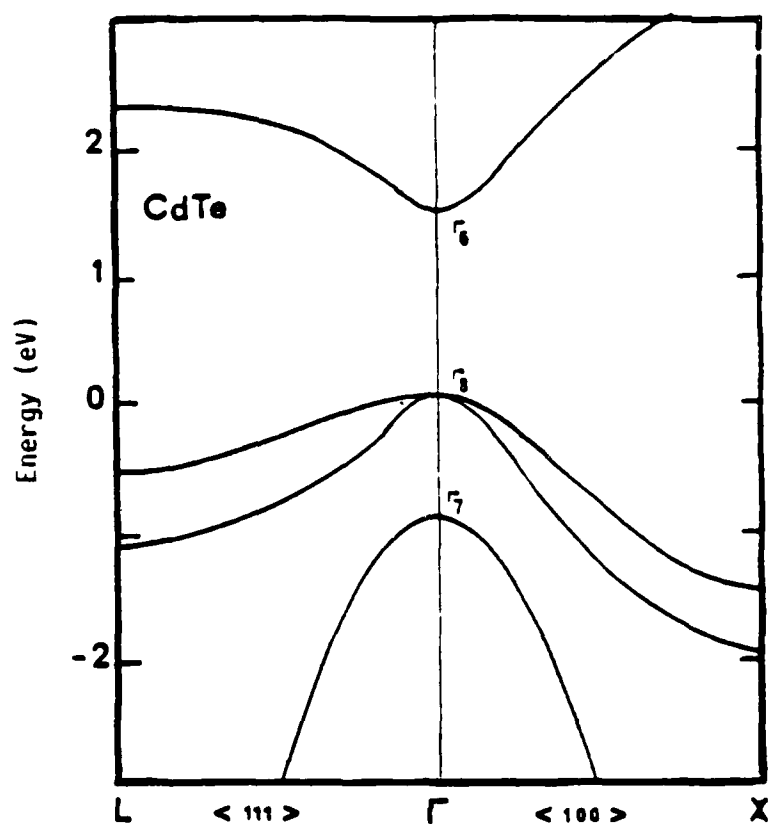


Fig. 10 Band structure of CdTe

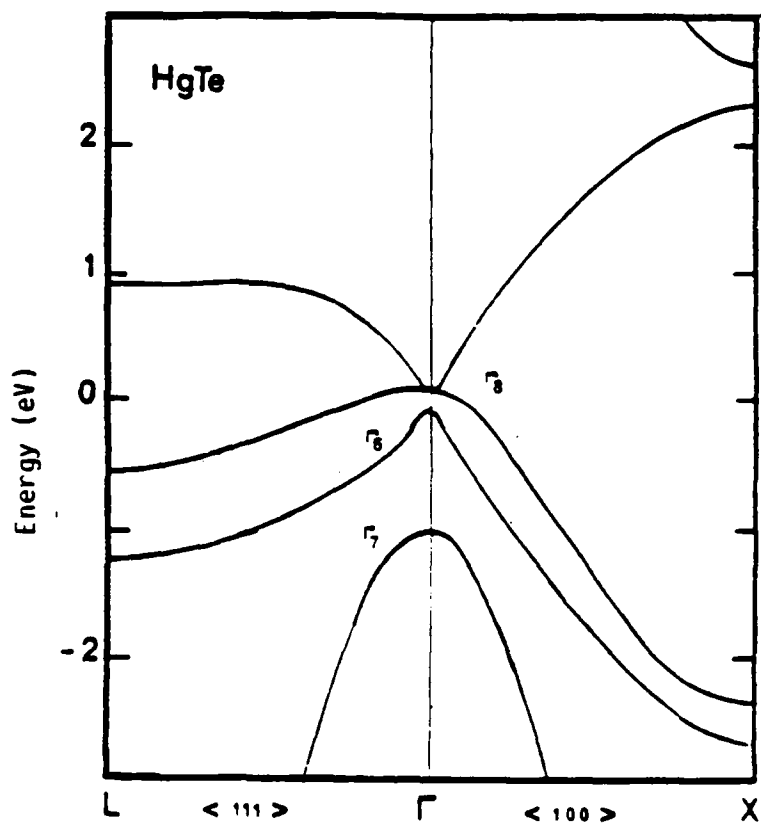


Fig. 11 Band structure of HgTe

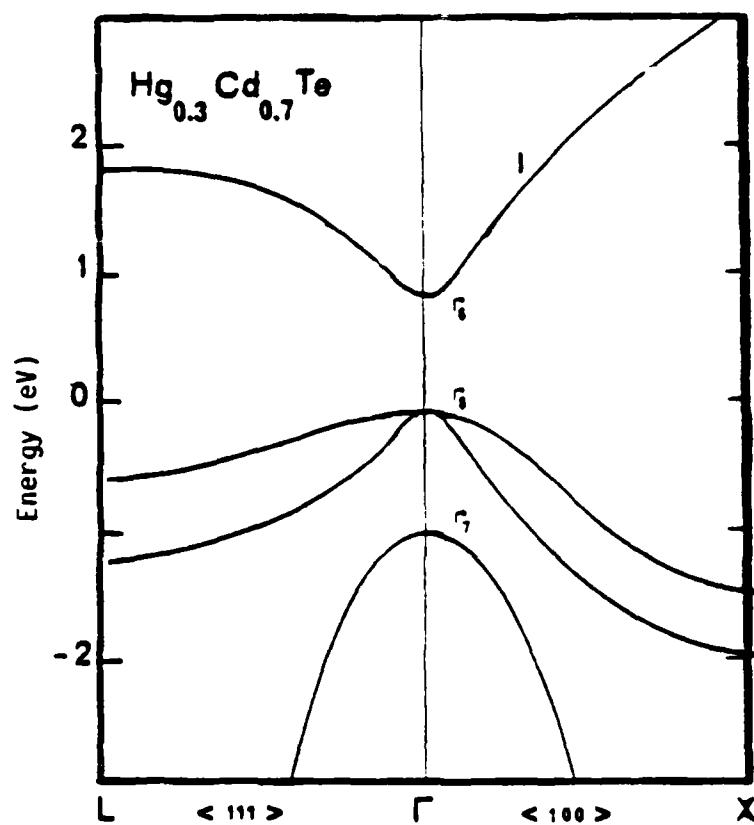


Fig. 12 Band structure of $\text{Hg}_{0.3}\text{Cd}_{0.7}\text{Te}$

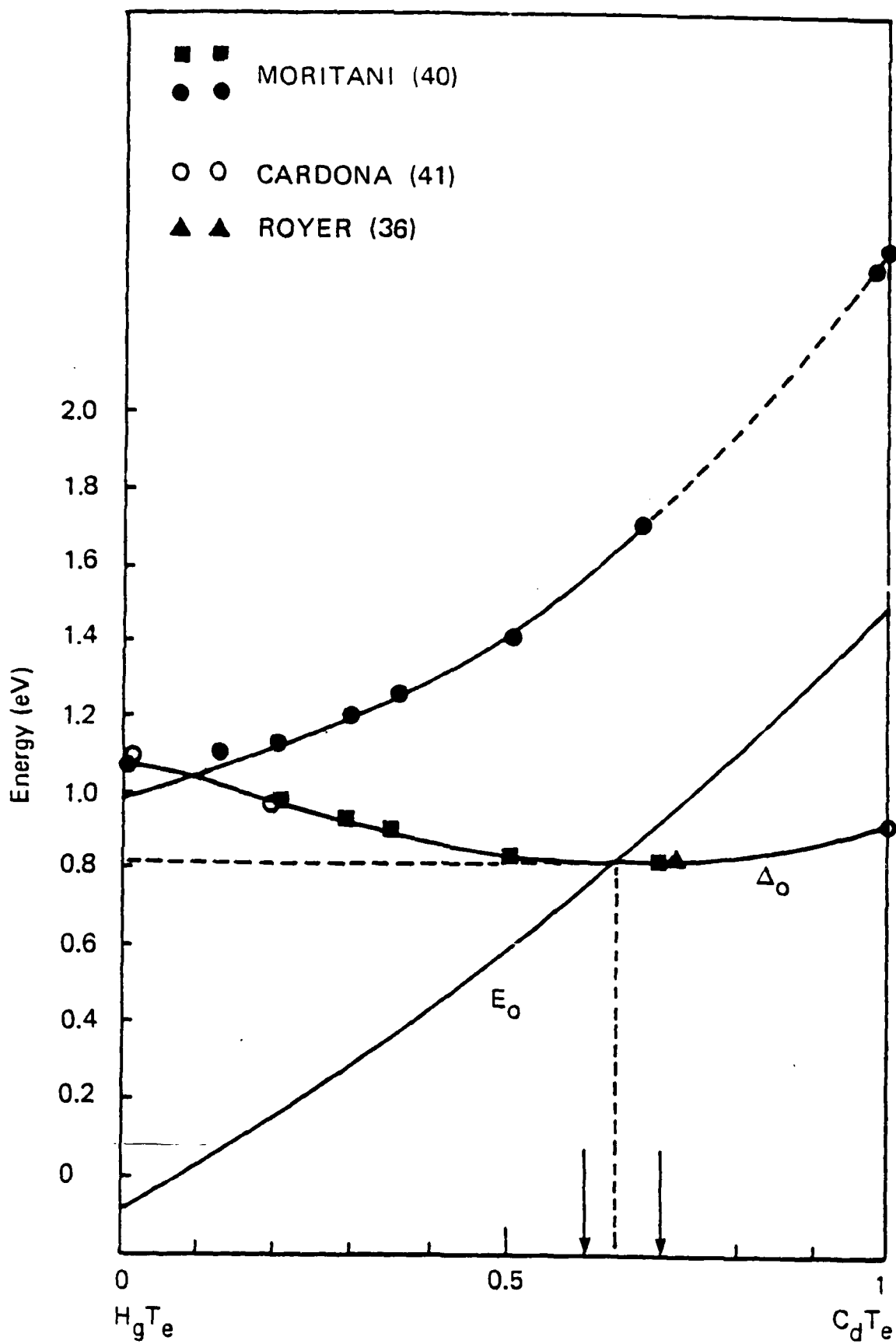


Fig. 13 E_g and Δ_0 vs. composition (36) (40) (41)

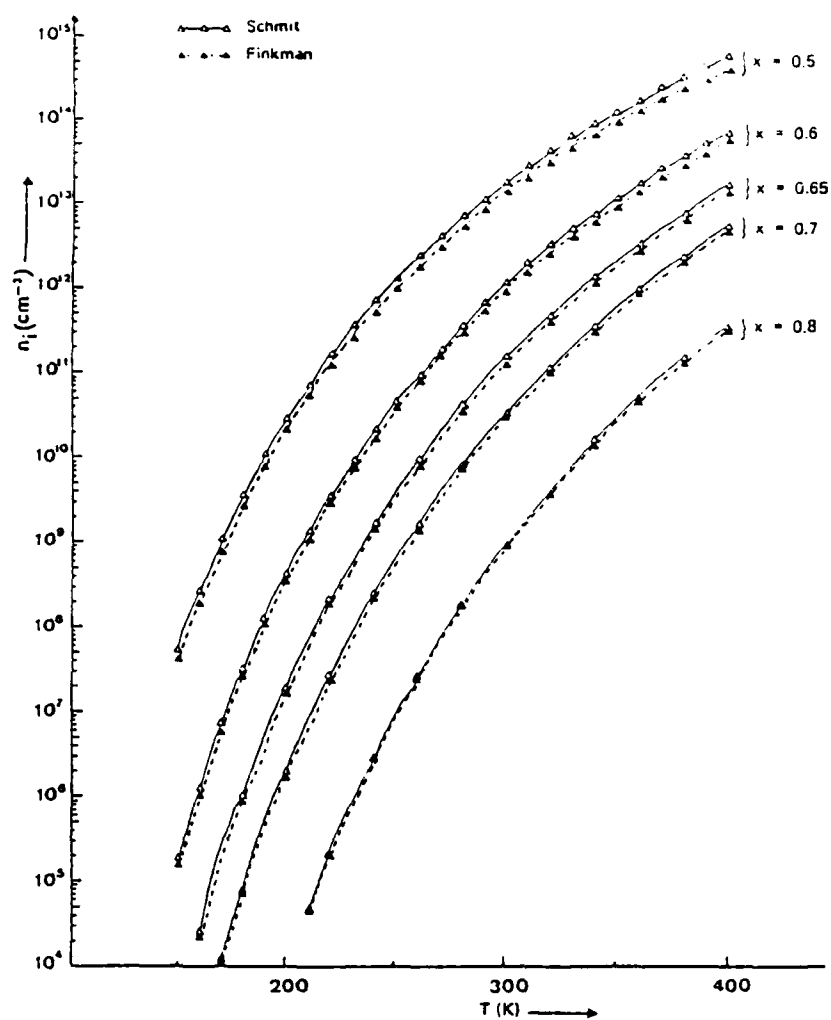


Fig. 14 Intrinsic carrier concentration

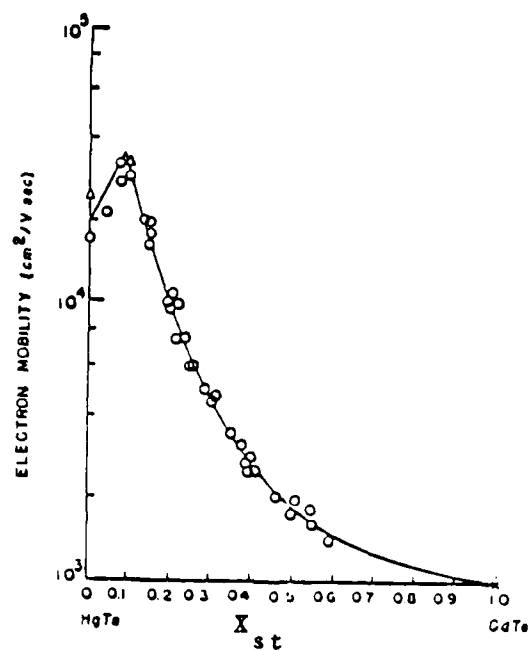


Fig. 15 Electron mobility at 300 K (from Scott (48))

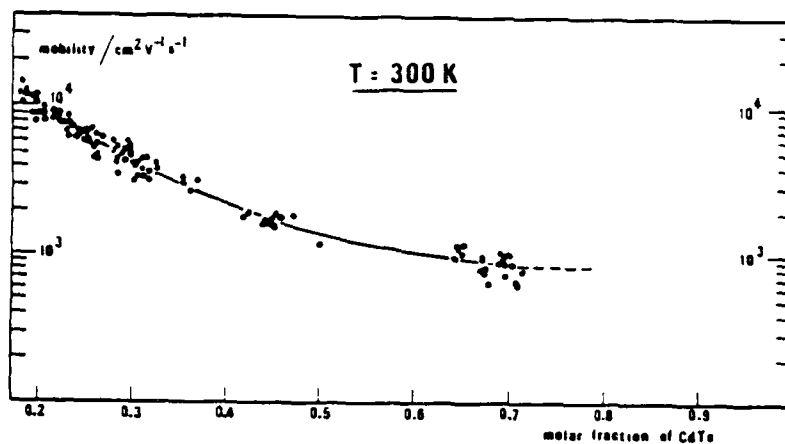


Fig. 16 Mobility of N-type $\text{Hg}_{1-x}\text{Cd}_x\text{Te}$ at 300 K

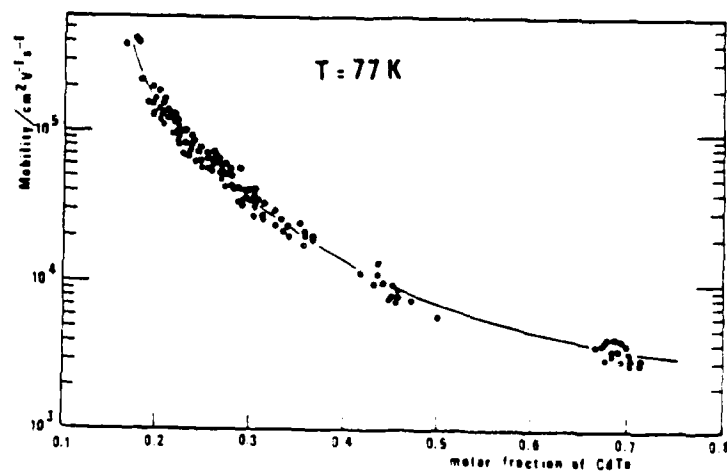


Fig. 17 Mobility of N-type $\text{Hg}_{1-x}\text{Cd}_x\text{Te}$ at 77 K

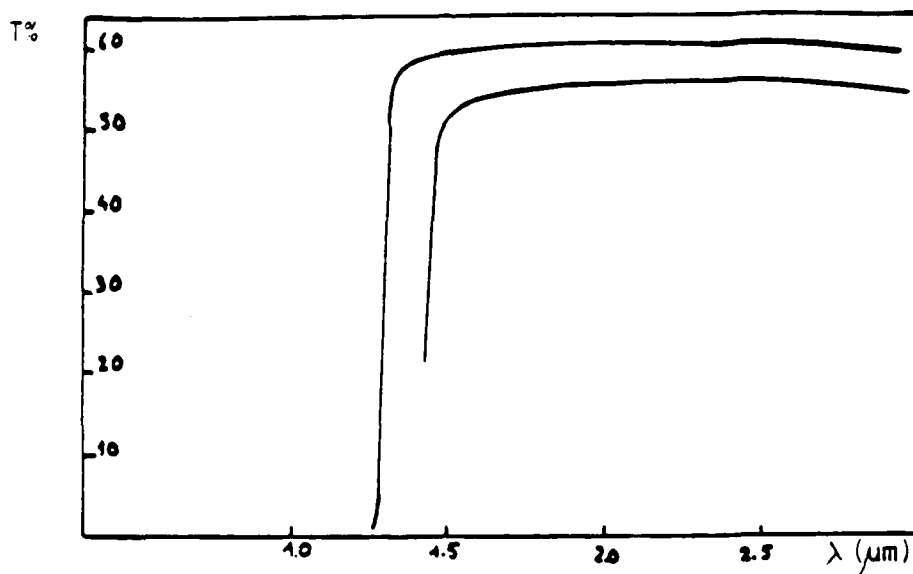


Fig. 18 Optical transmission vs. wavelength

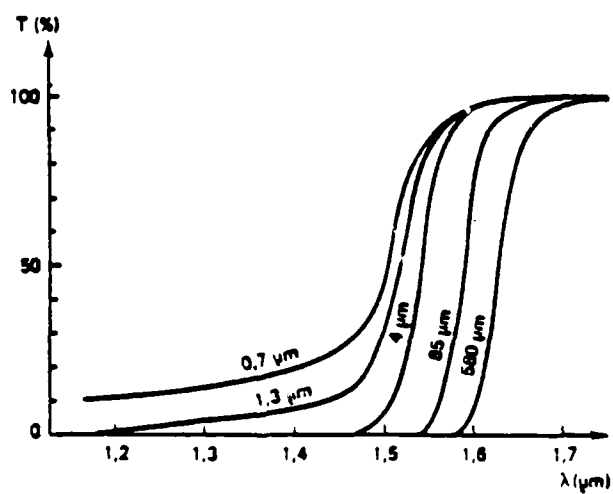


Fig. 19 Internal transmission of $\text{Hg}_{0.3}\text{Cd}_{0.7}\text{Te}$ vs. wavelength for different wafer thicknesses

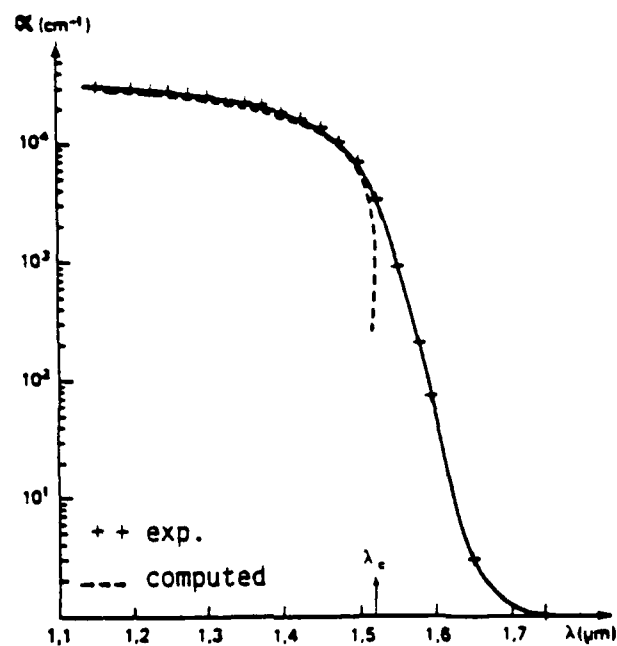


Fig. 20 Absorption coefficient vs. wavelength for $\text{Hg}_{0.3}\text{Cd}_{0.7}\text{Te}$

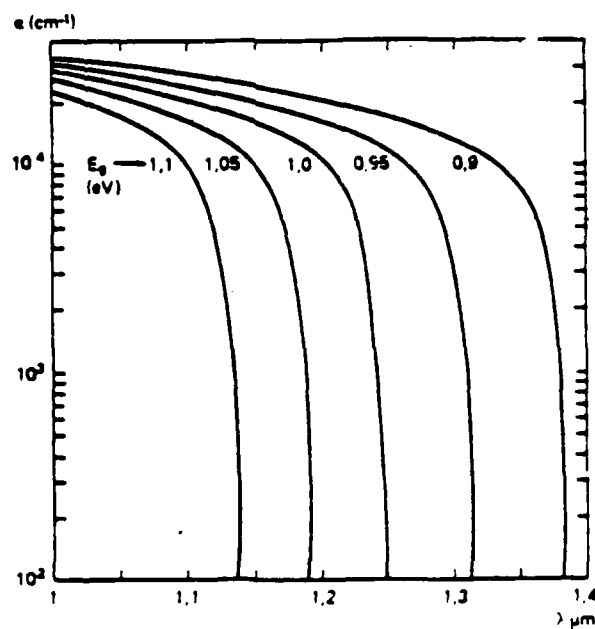


Fig. 21 Absorption coefficient vs. wavelength for different values of E_g

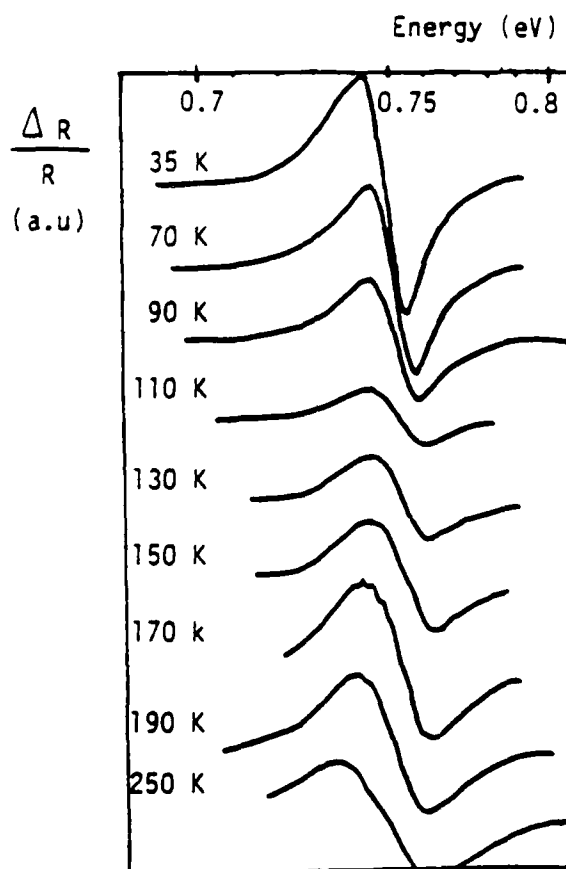


Fig. 22 Relative change of reflectivity at different temperatures for $x = 0.6$

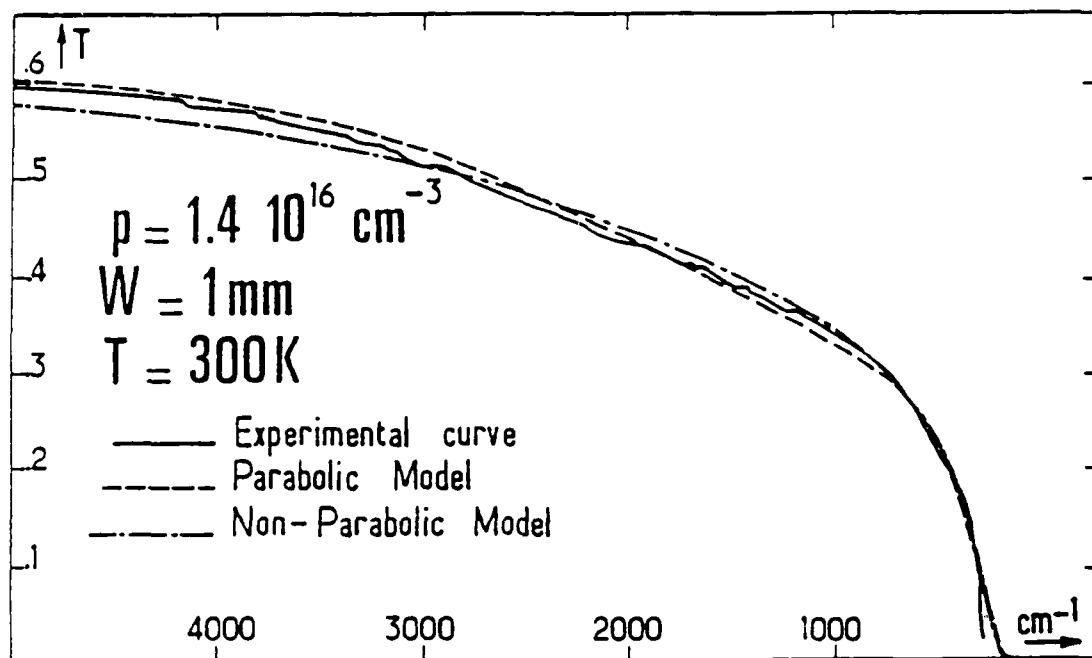


Fig. 23 Theoretical and experimental transmission curves for $E_g = 0.89 \text{ eV}$

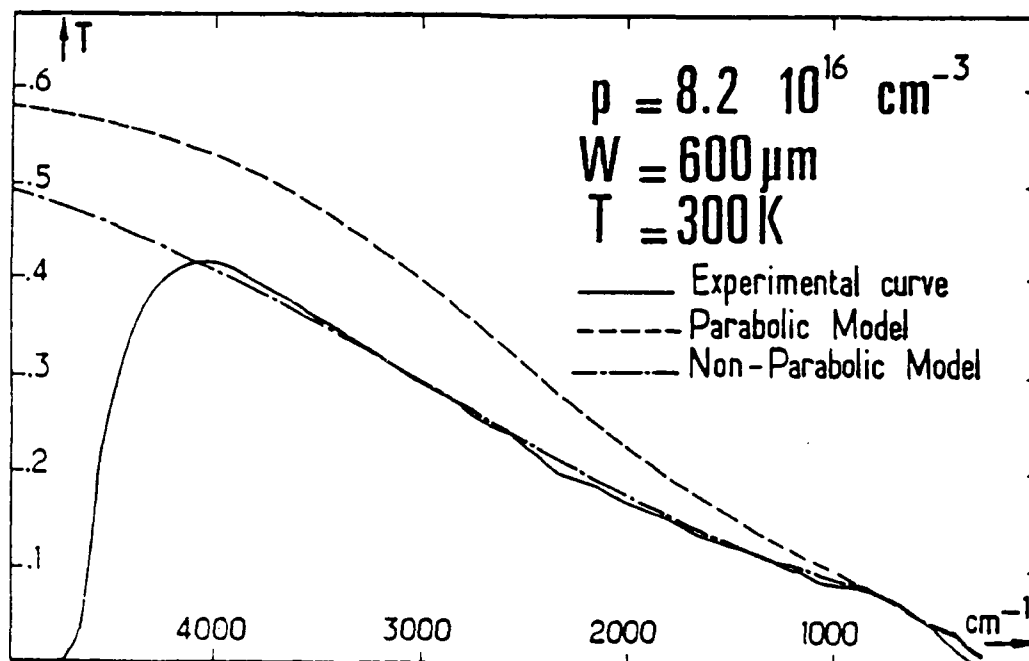


Fig. 24 Theoretical and experimental transmission curves for $E_g = 0.59 \text{ eV}$

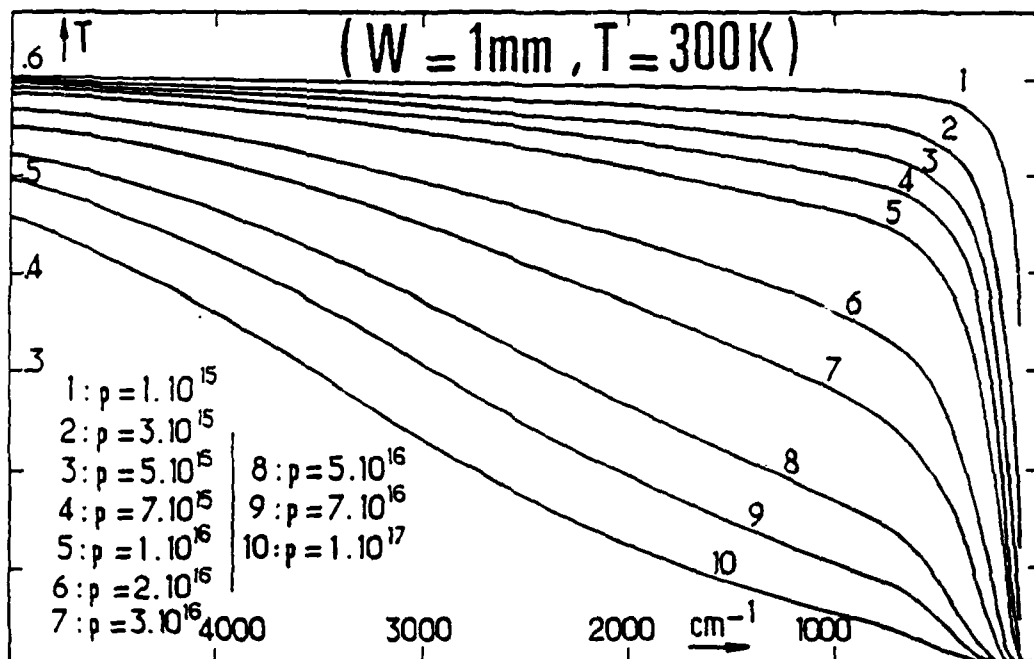


Fig. 25 Transmission curves for different P-type concentrations at $E_g = 0.89 \text{ eV}$

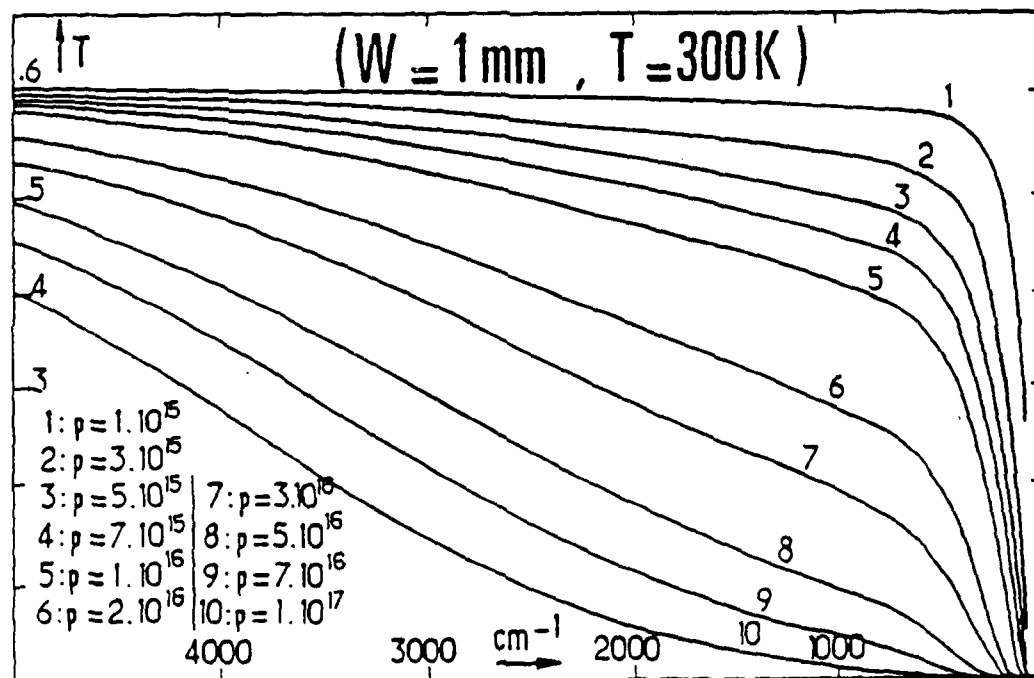
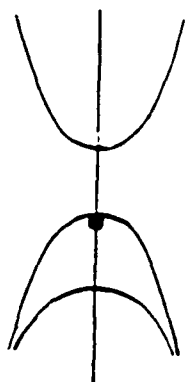
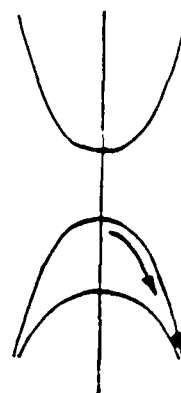


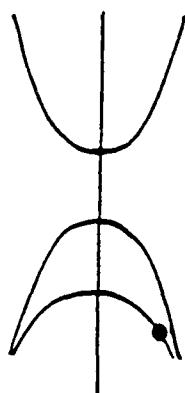
Fig. 26 Transmission curves for different P-type concentrations at $E_g = 0.59 \text{ eV}$



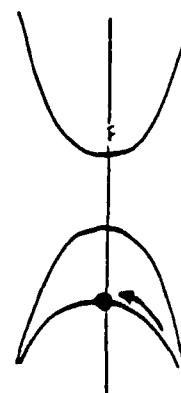
a - Absorption
of a photon



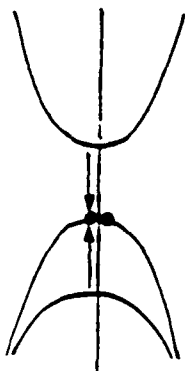
b - Influence of the
strong electric
field



c - Interaction
with a phonon

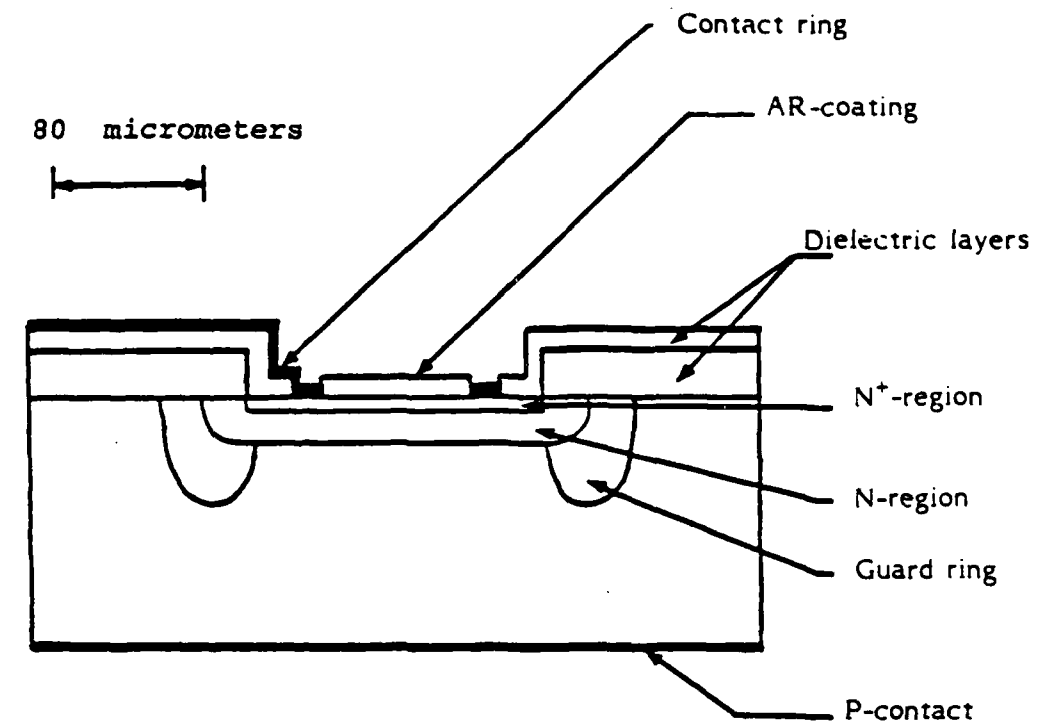


d - Hole relaxation



e - Inverse Auger
effect at $k = 0$

Fig. 27 Hole-generated spin-orbit resonance



Region:	Carrier concentr.: (cm ⁻³)	Depth: (μm)
P	10 ¹⁶	400
N	10 ¹⁵	3
N ⁺	10 ¹⁸	0.3

Fig. 28a Cross-sectional structure of an avalanche photodiode

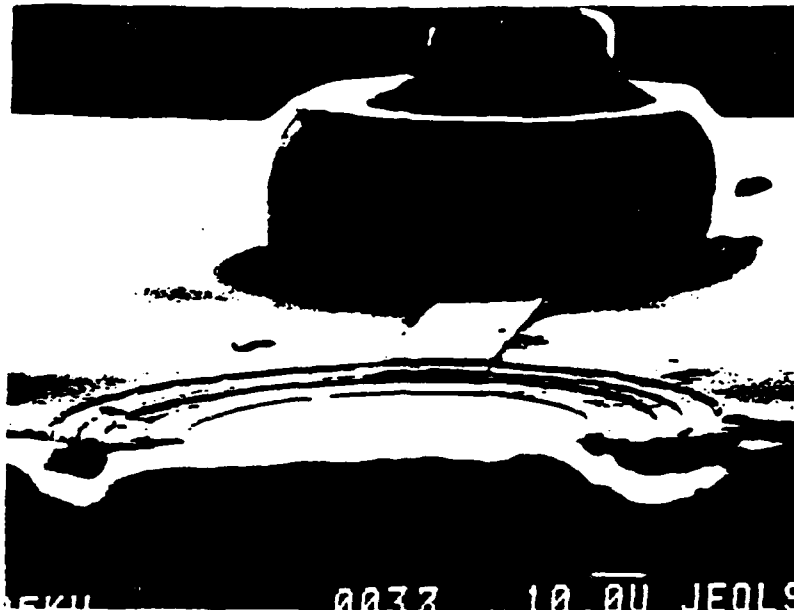


Fig. 28b Cross-sectional view of an avalanche photodiode

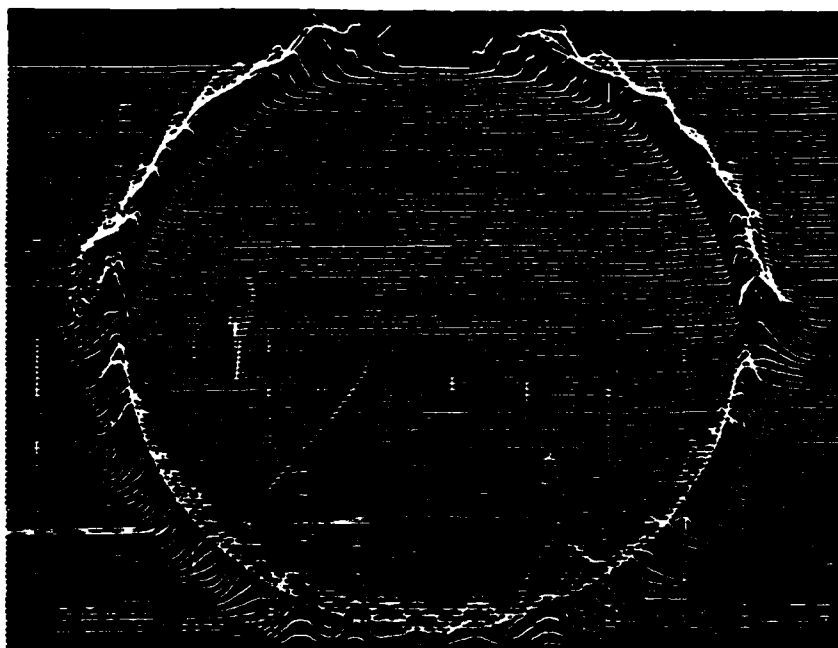


Fig. 29 Breakdown at the edge of the junction of a photodiode without guard ring

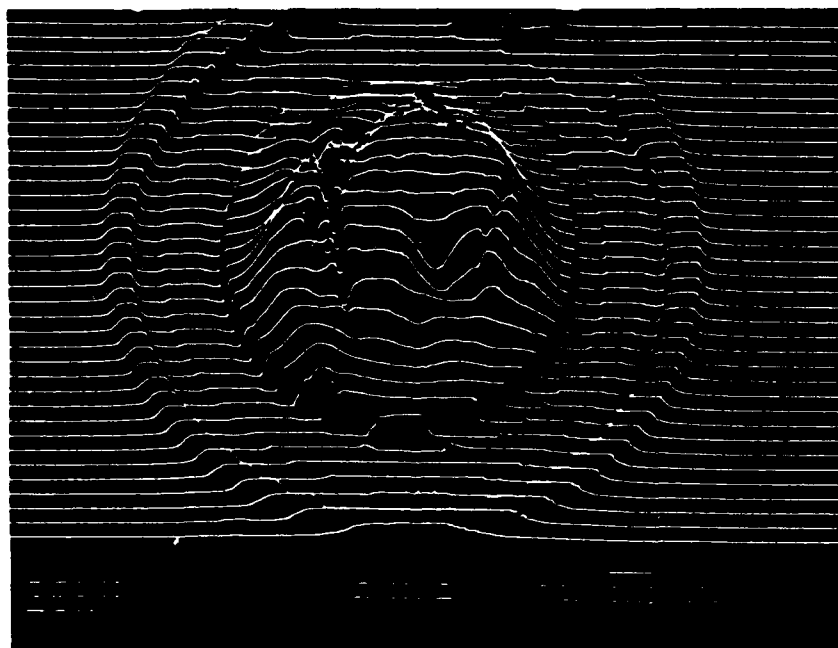


Fig. 30 Central multiplication of a photodiode with guard ring

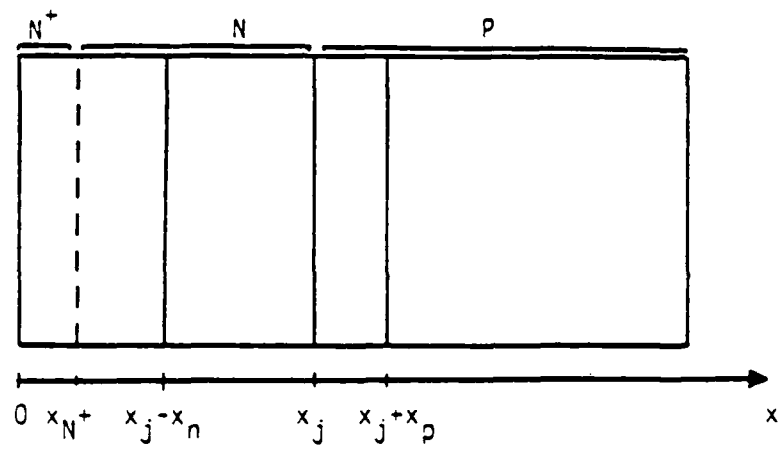


Fig. 31 Schematic structure across the junction

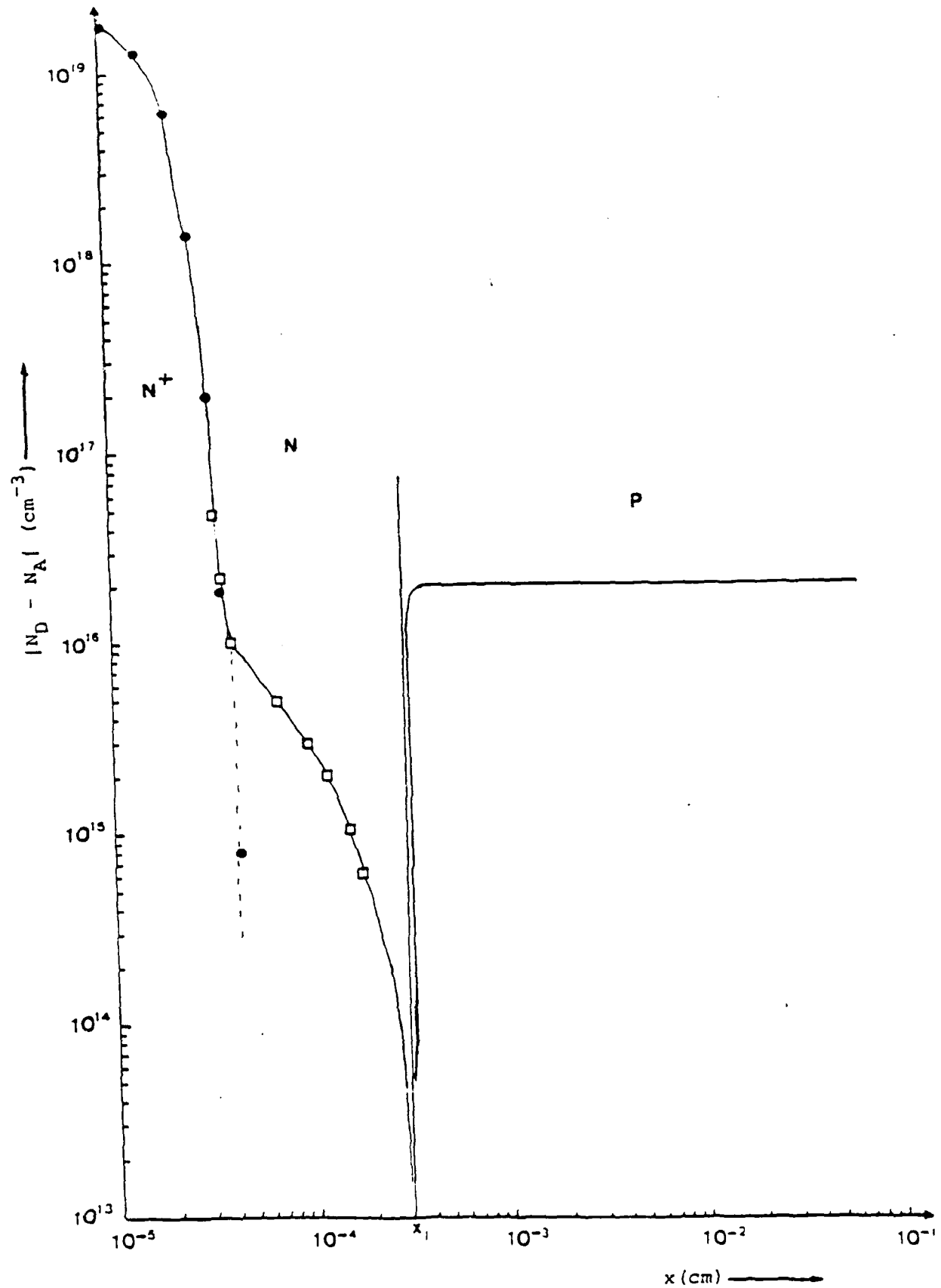


Fig. 32 Valenza's doping profile (59)

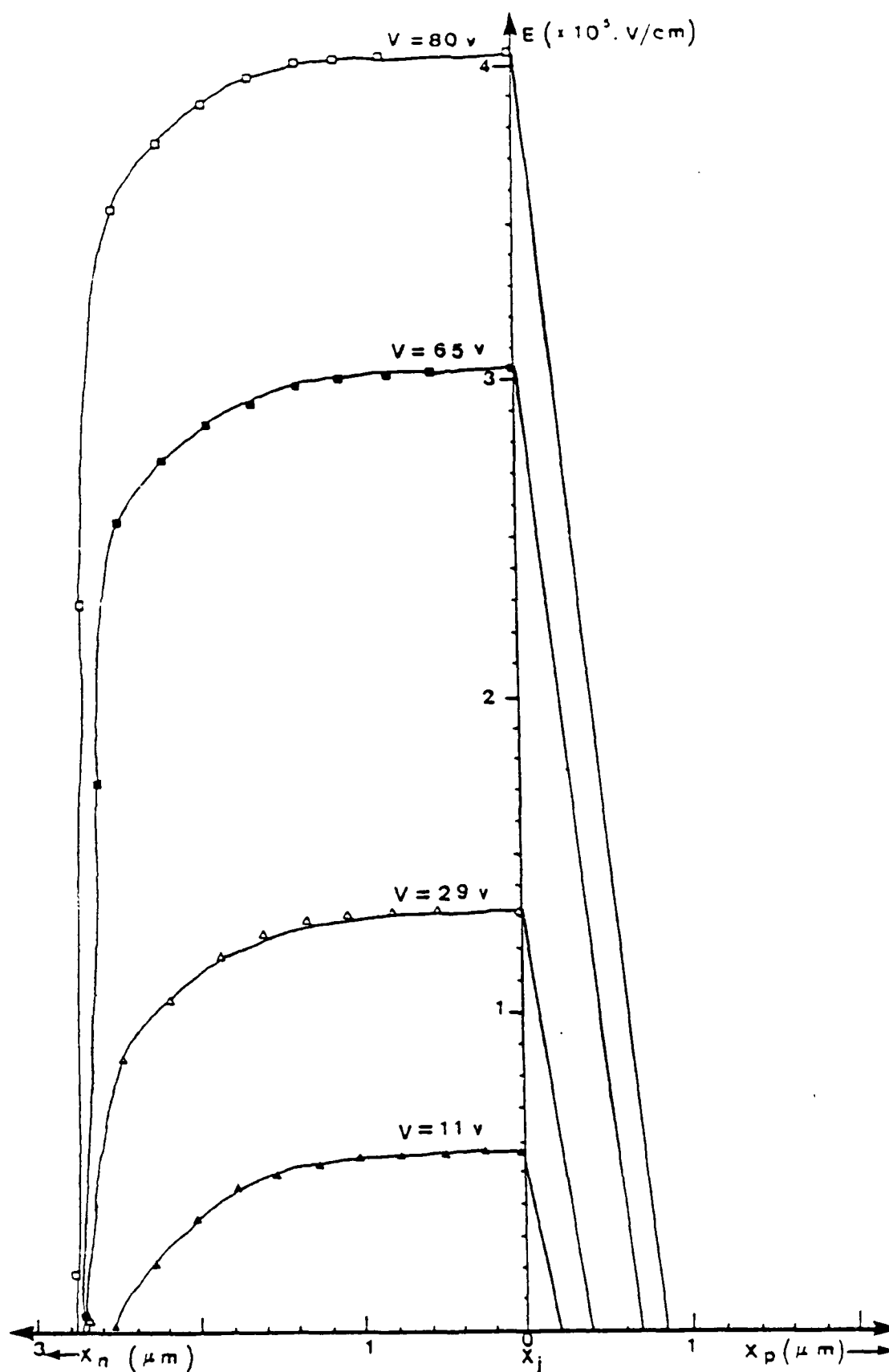


Fig. 33 Electric field as a function of distance, as reported by Valenza (15)

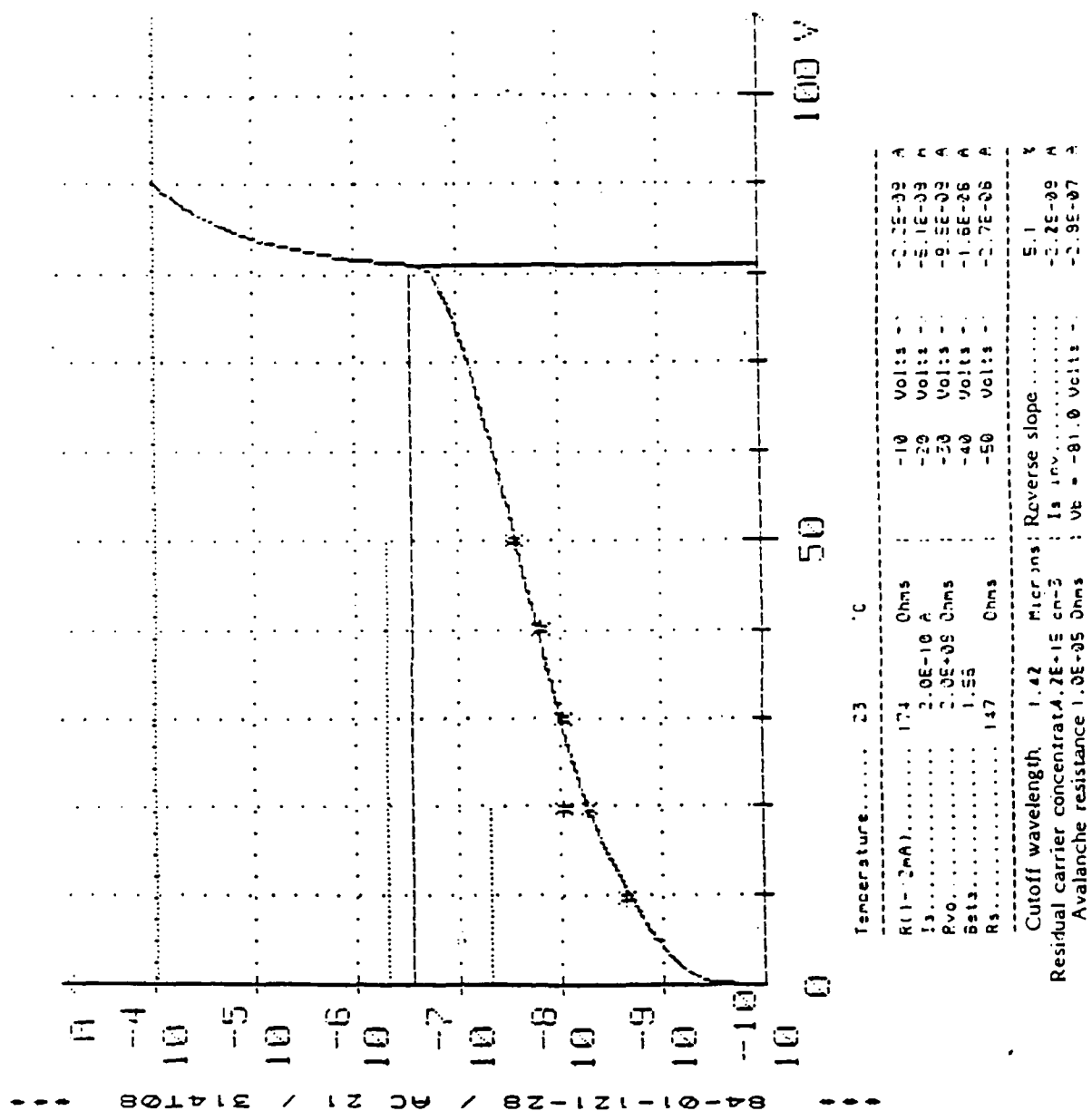


Fig. 34 I(V) curve of an avalanche photodiode

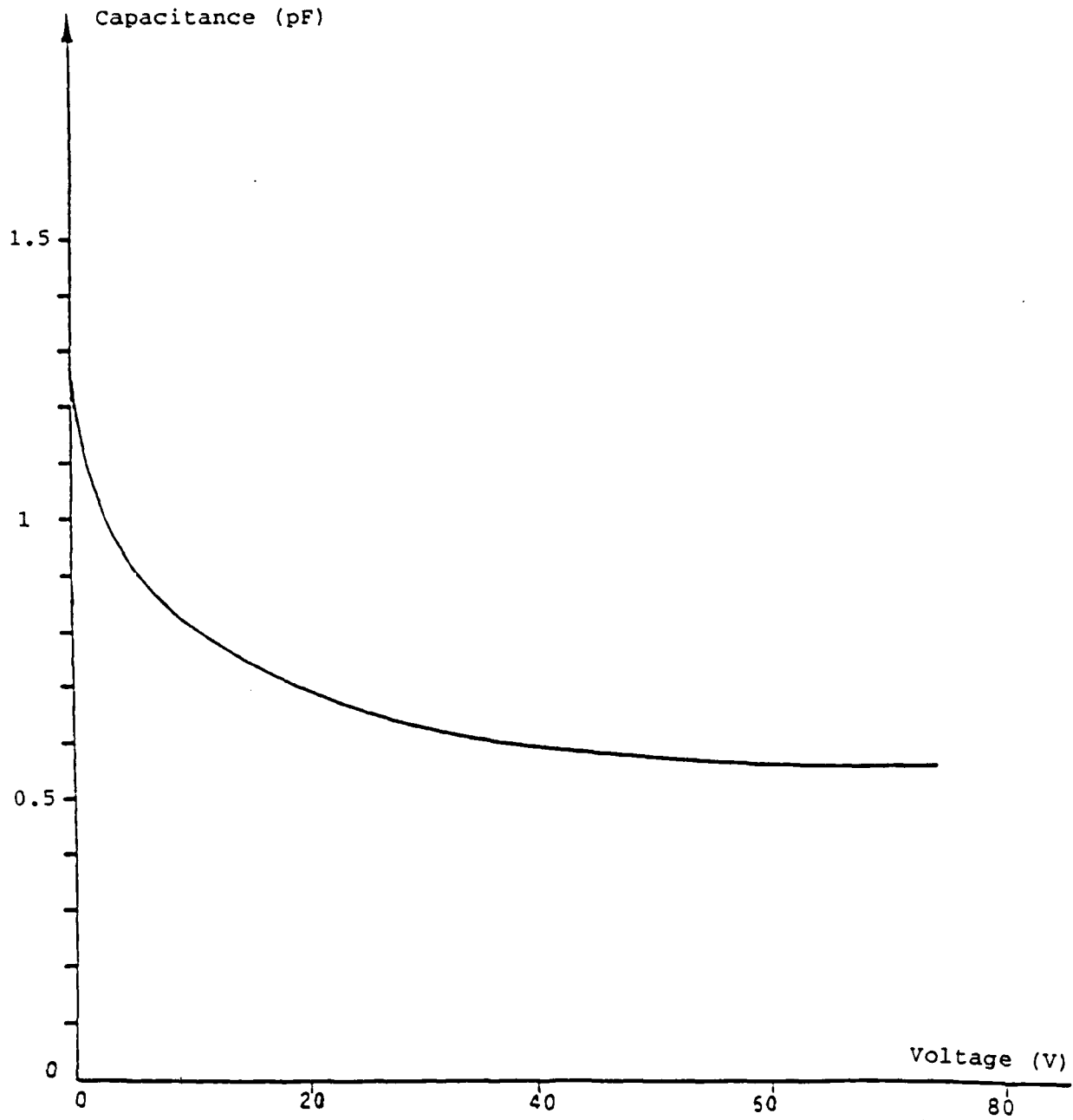


Fig. 35 Voltage - Capacitance characteristics up to 80 V

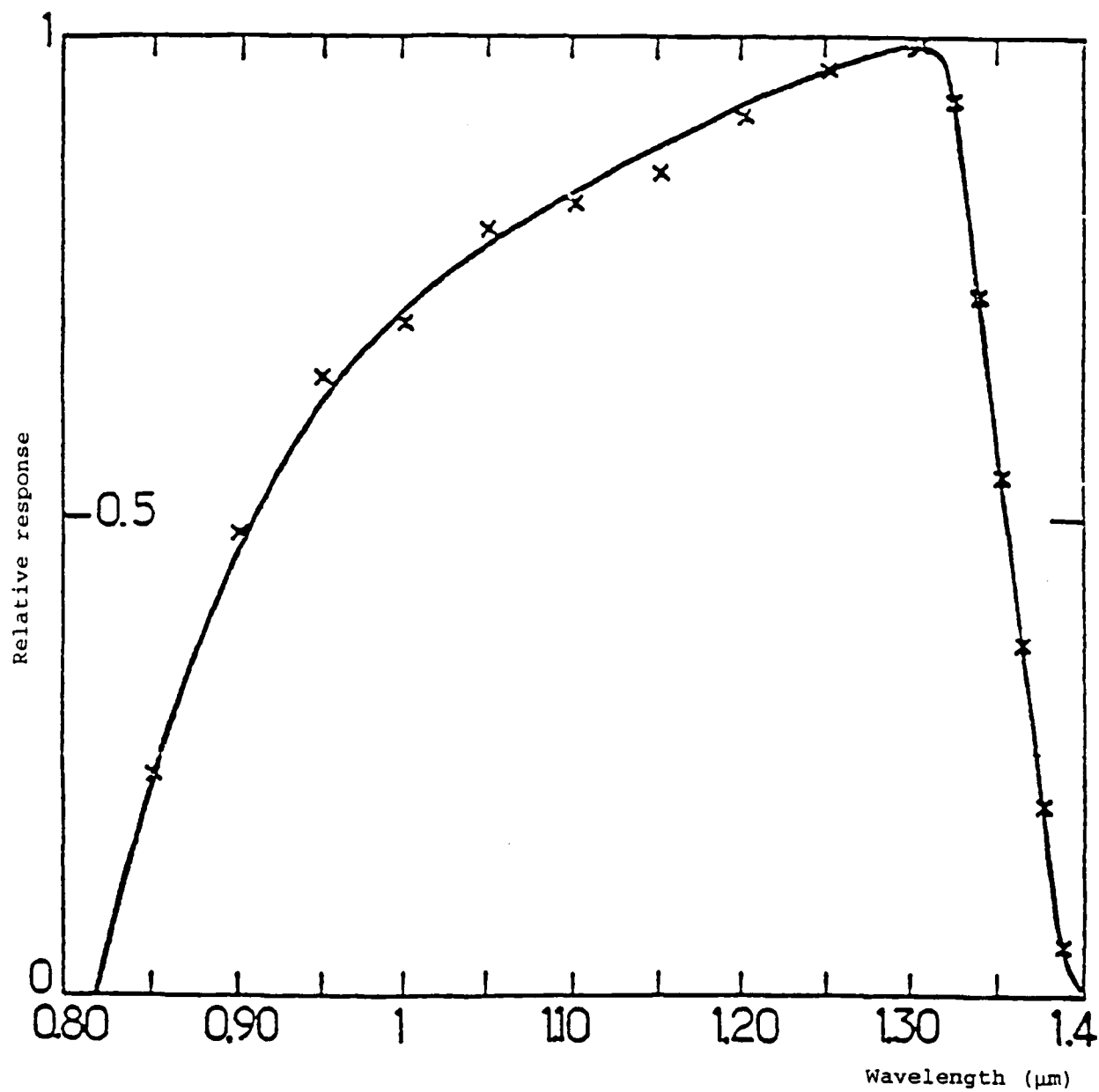


Fig. 36 Spectral response of a $\text{Hg}_{0.3}\text{Cd}_{0.7}\text{Te}$ photodiode at 300 K

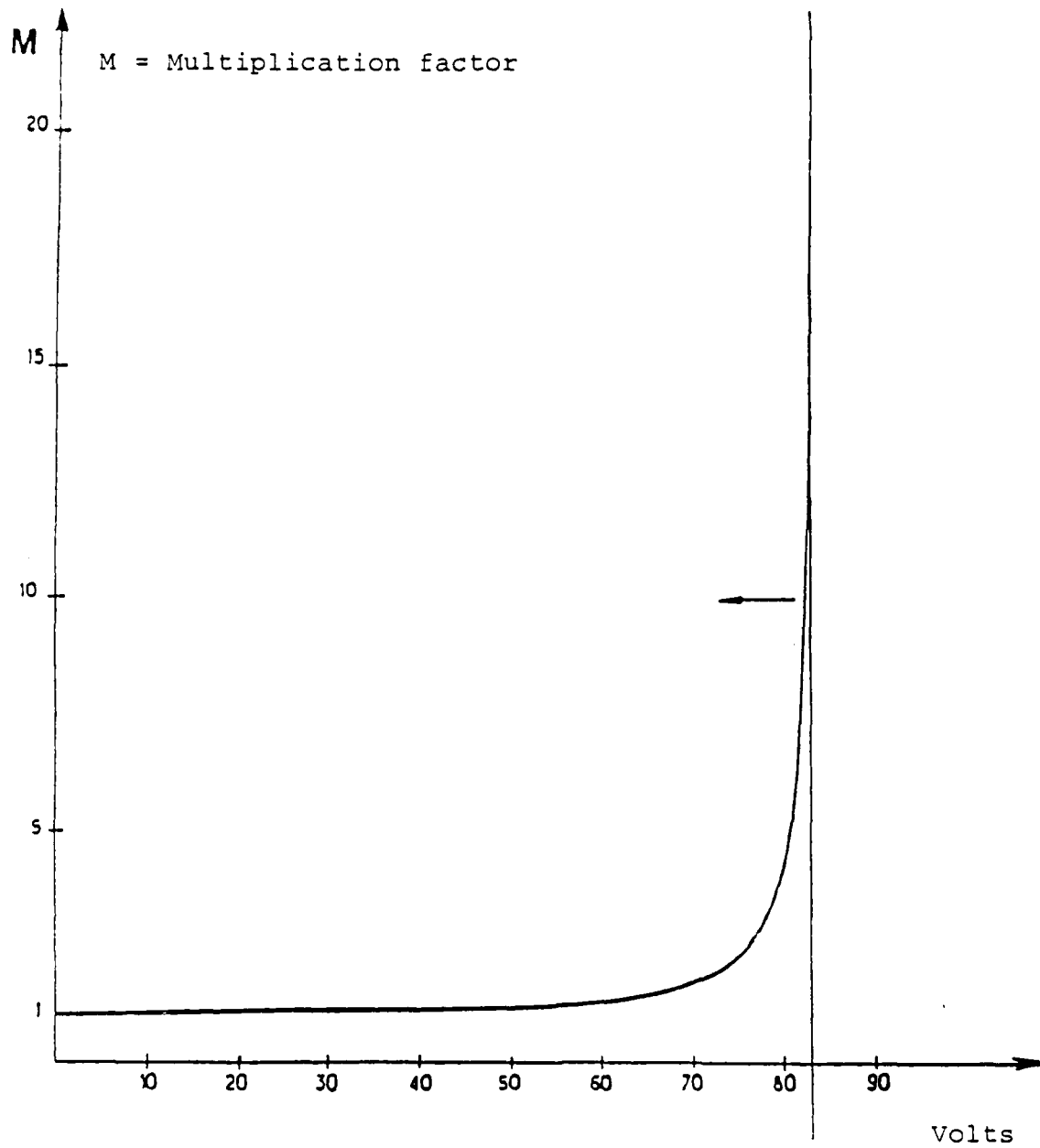


Fig. 37 Multiplication as a function of voltage

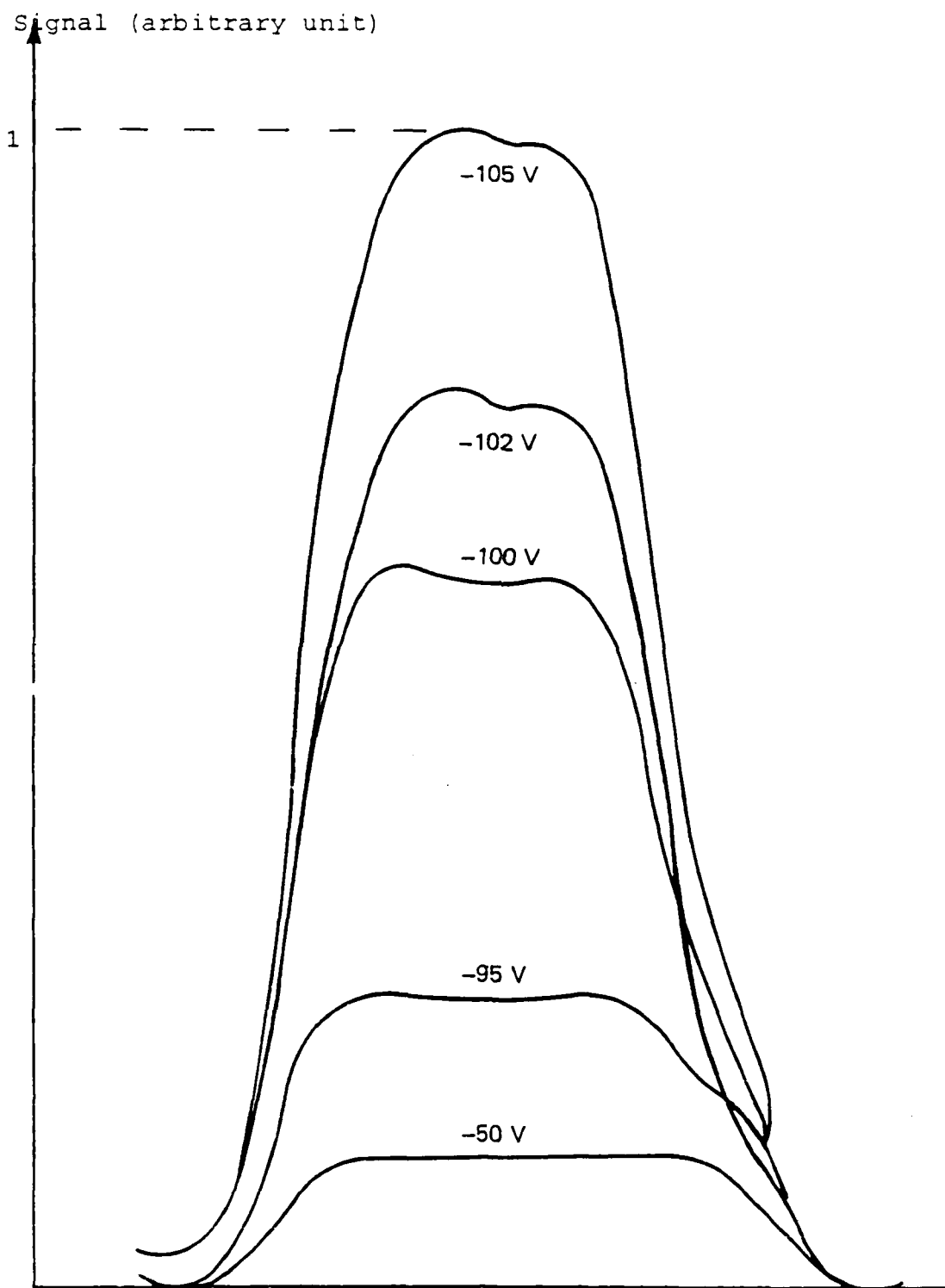


Fig. 38 Photo-response as a function of distance (spot scan along one diameter) for different values of reverse bias voltage

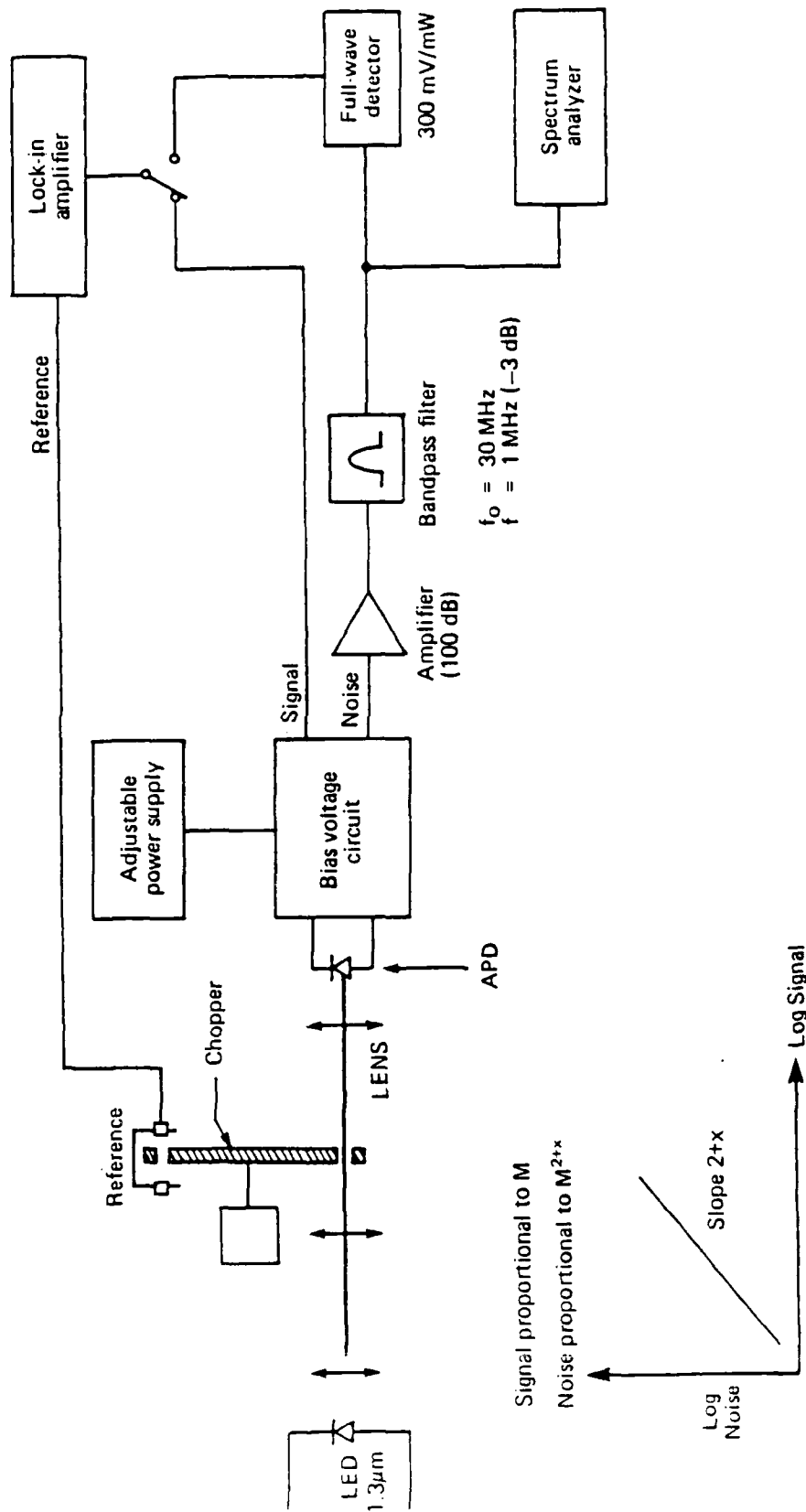


Fig. 39 Schematic layout of the test bench for the measurement of avalanche noise

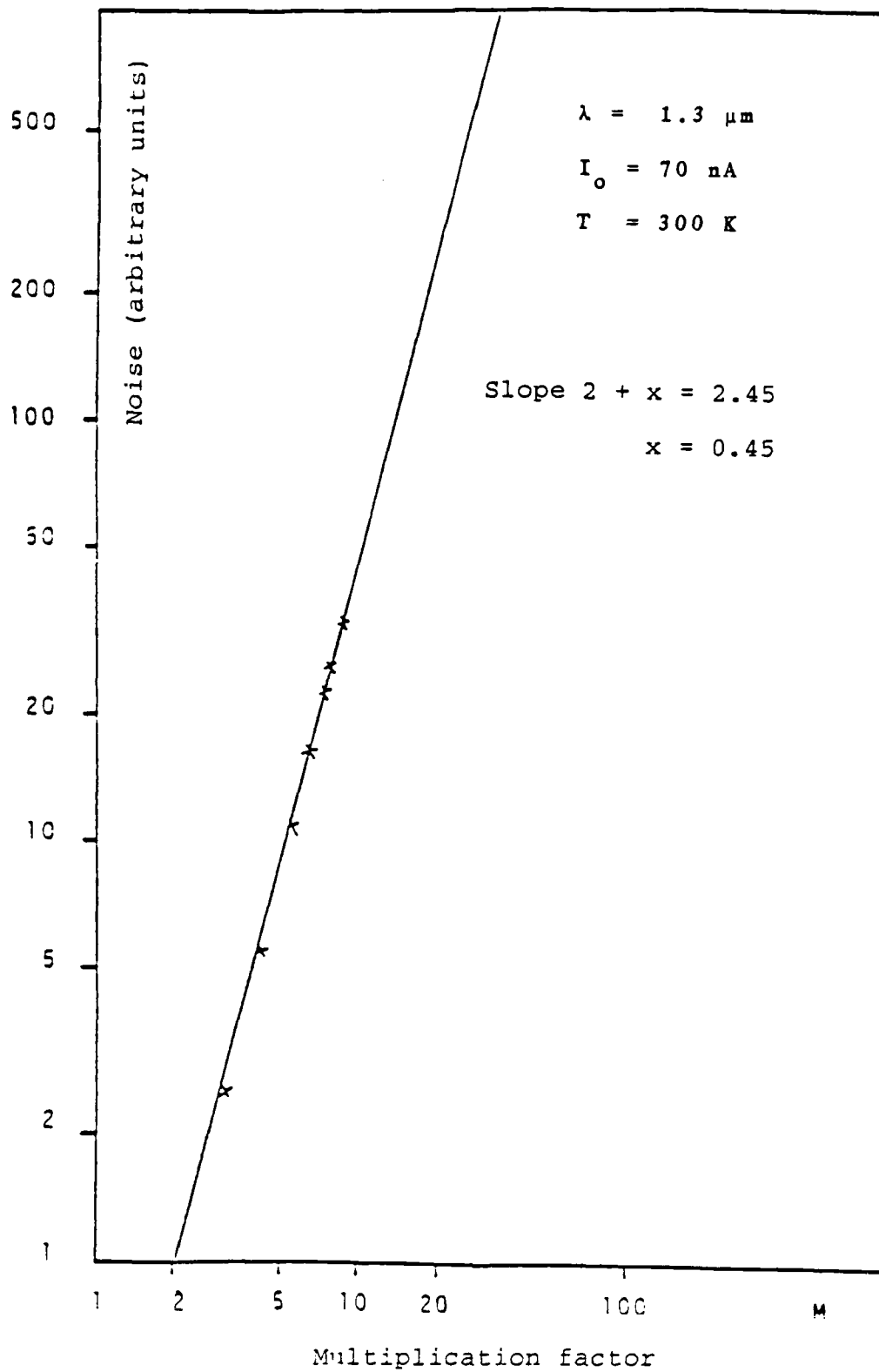


Fig. 40 Photon flux noise as a function of multiplication

	Typical	Maximum
Sensitive area (diameter)	0.080 mm	
Dark current at ~ 10 V	2 nA	0.5 nA
Current responsivity at 1.3 μm	0.70 A W^{-1}	0.8 A W^{-1}
Spectral range	0.9 - 1.35 μm	
Capacitance at ~ 10 V	0.9 pF	0.5 pF
Bandwidth	400 MHz	850 MHz
Quantum efficiency	65%	75%
x-value of excess noise factor $F = M^x$ at $M = 10$	0.5	

Fig. 41 Main characteristics of HgCdTe 1.3 μm Avalanche Photodiodes

83-41-121-30

BA43

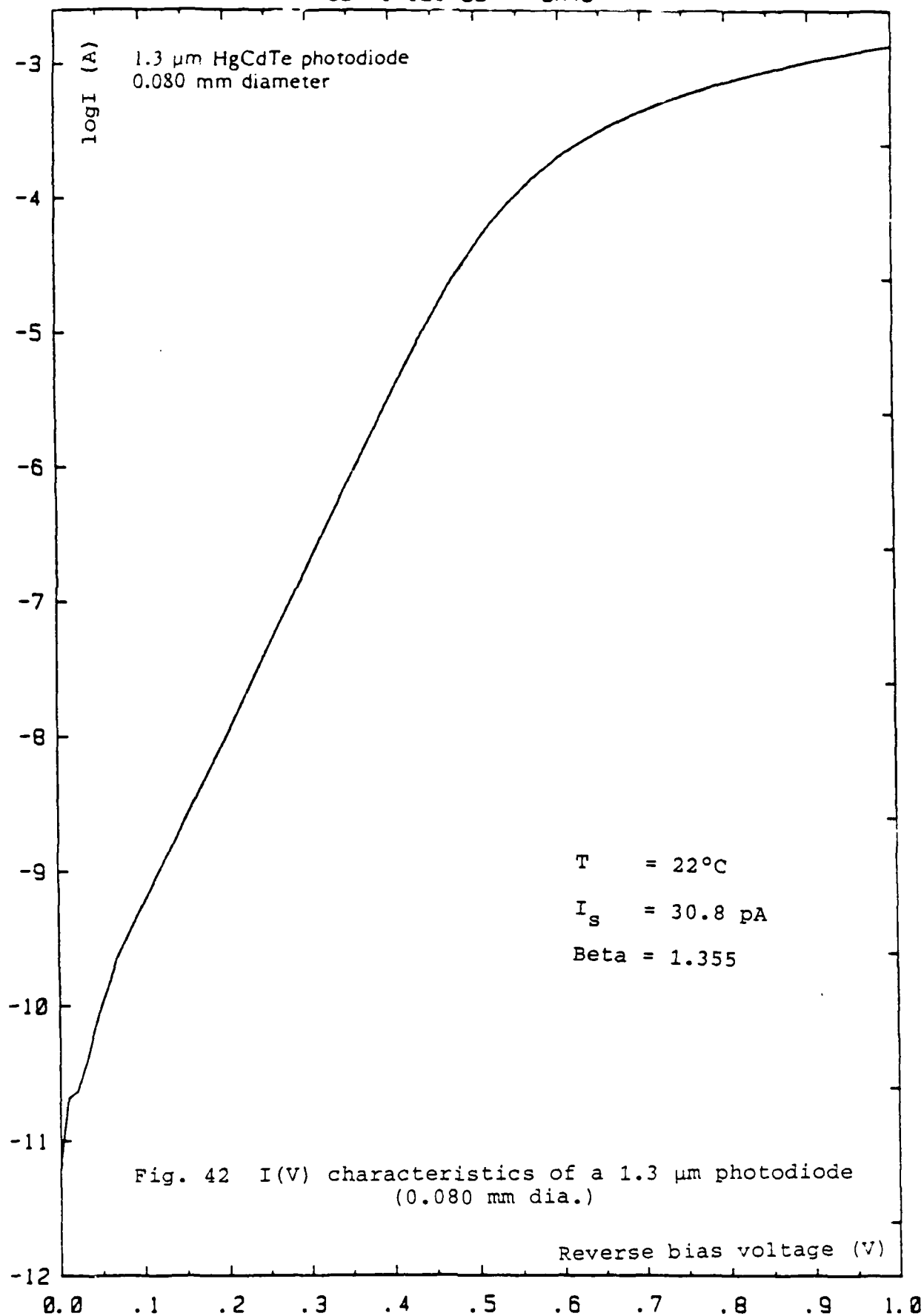


Fig. 42 I(V) characteristics of a 1.3 μm photodiode
(0.080 mm dia.)

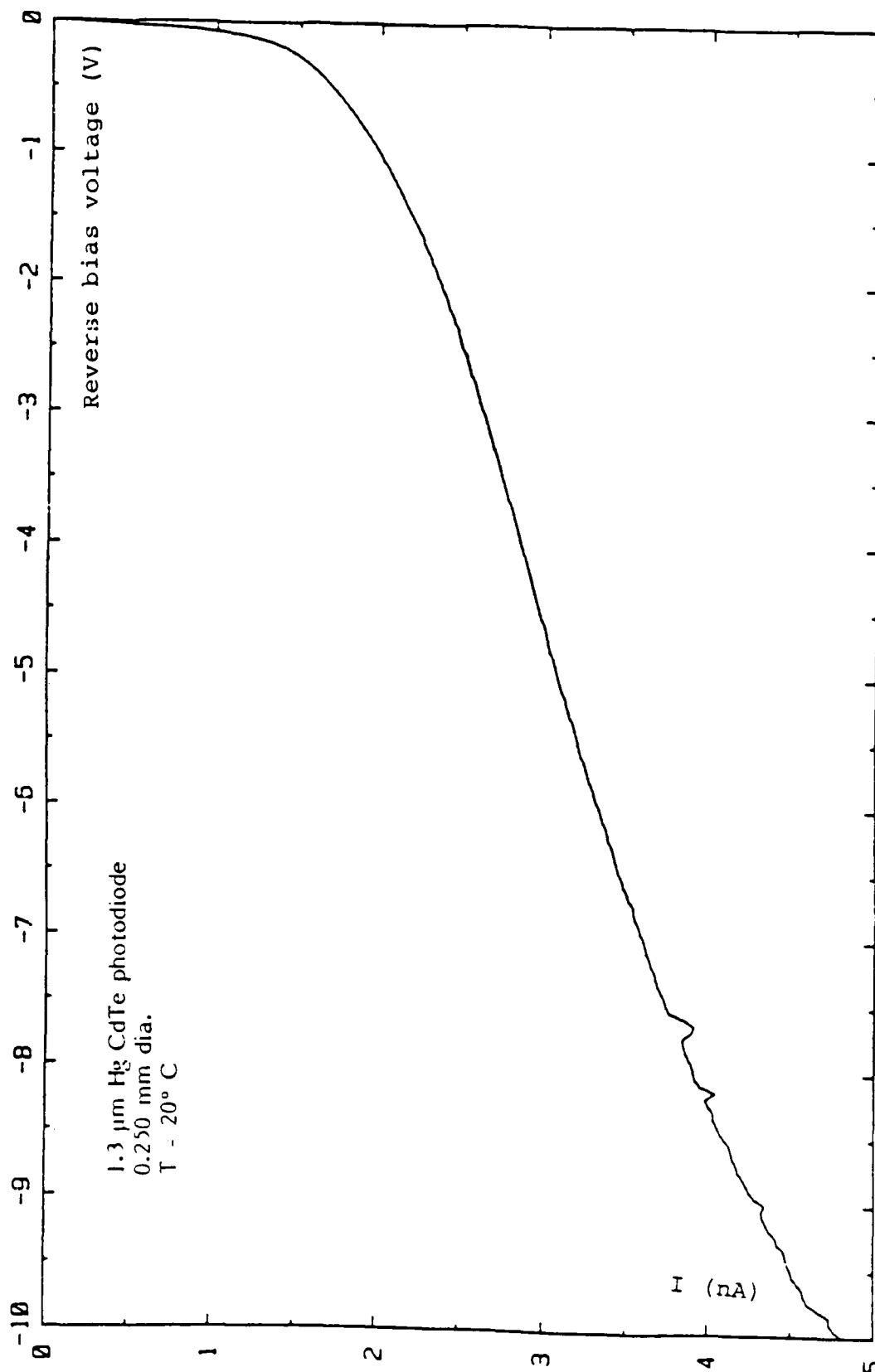
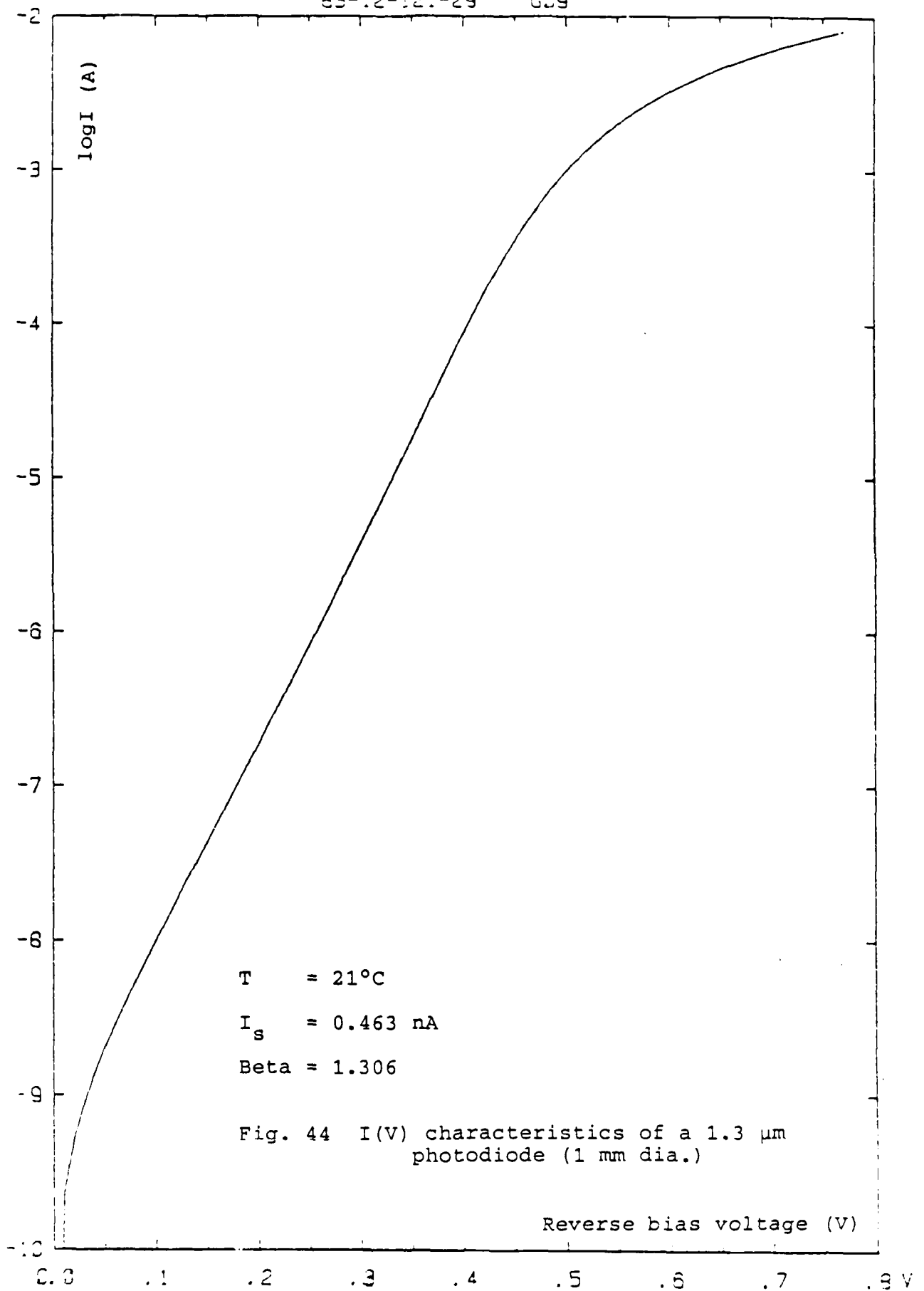


Fig. 43 I(V) characteristics of a 1.3 μm photodiode (0.250 mm dia.)

83-12-121-29

609



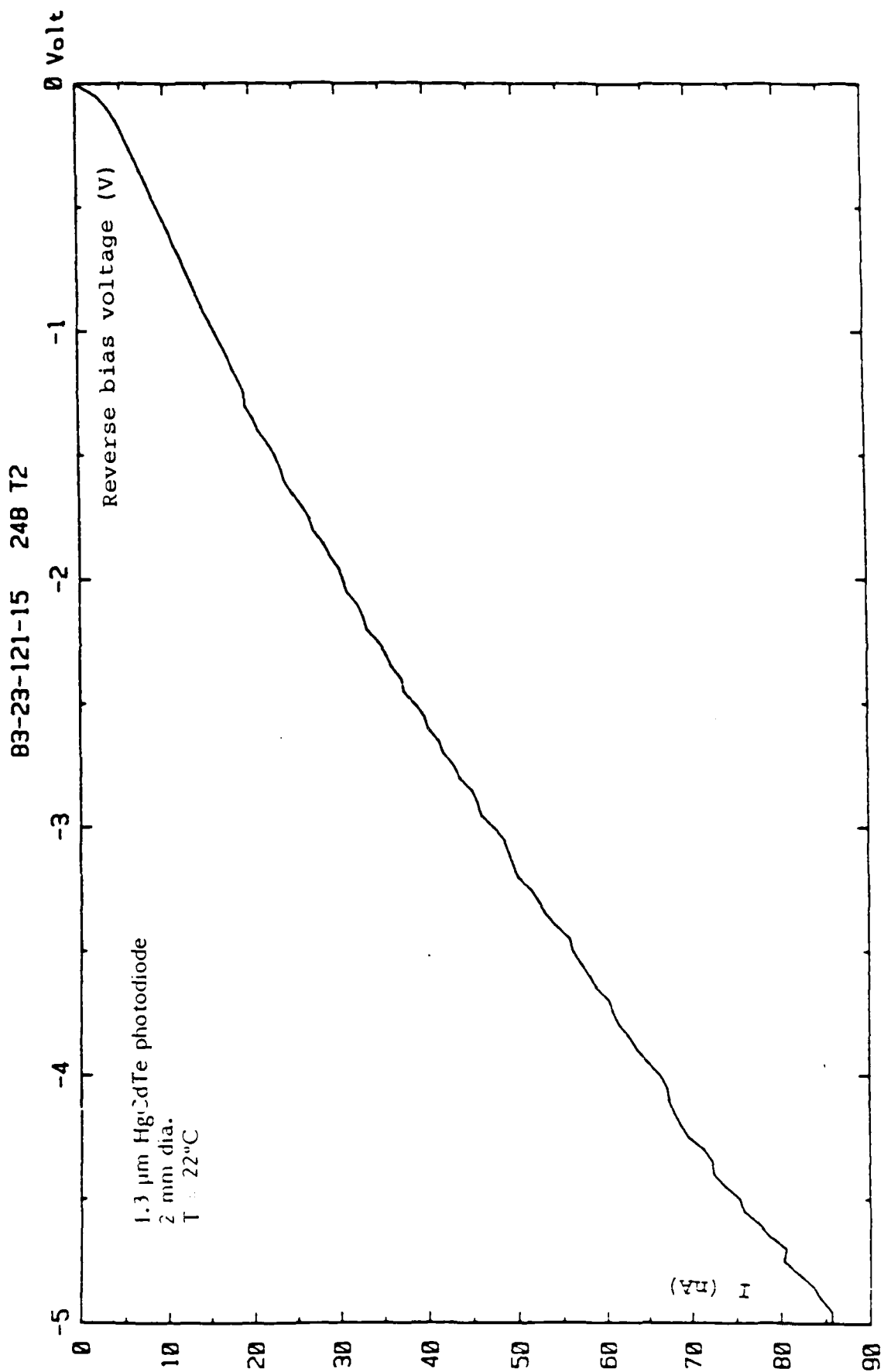


Fig. 45 I(V) characteristics of a 1.3 μm photodiode (2 mm dia.)

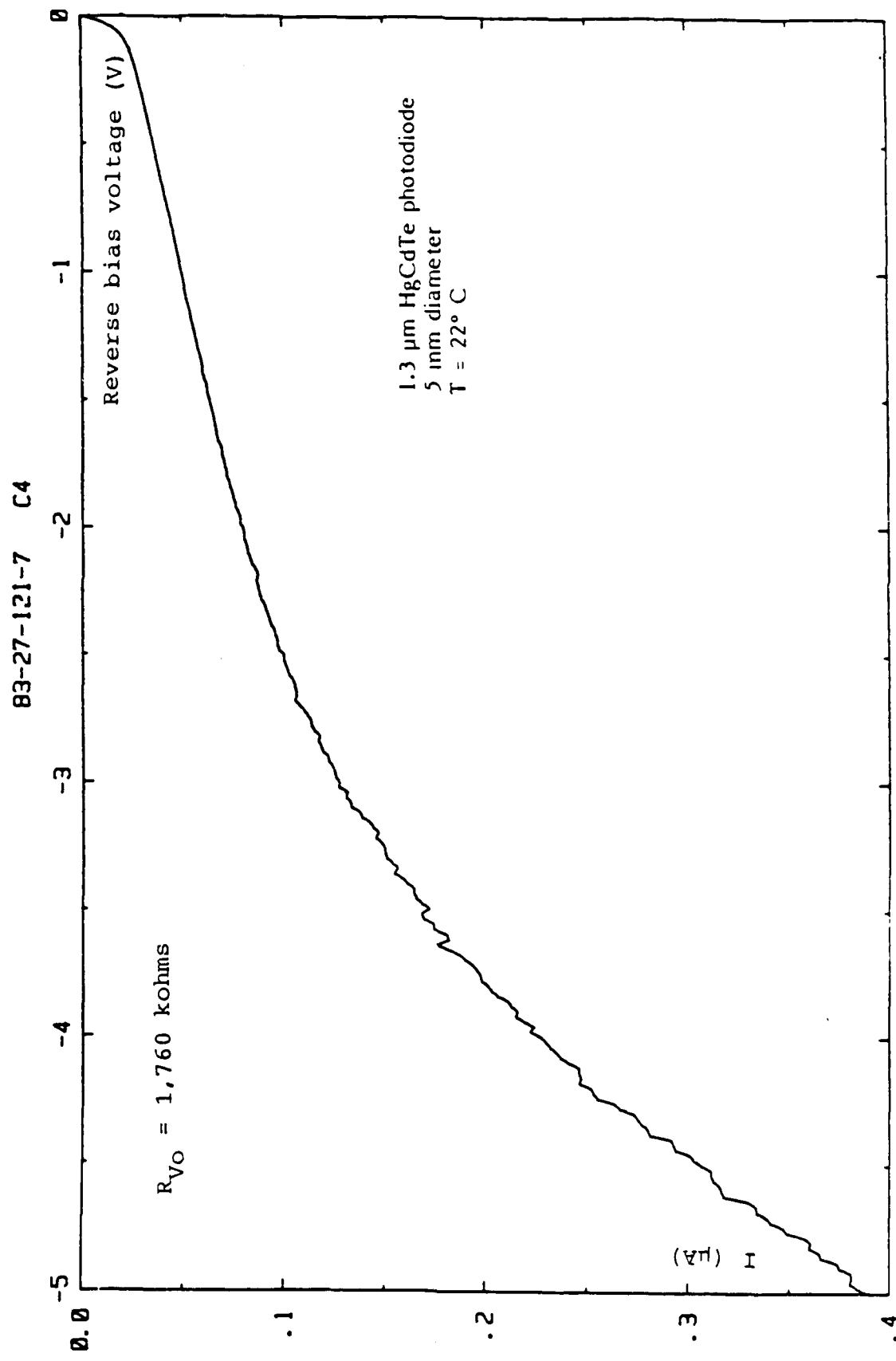
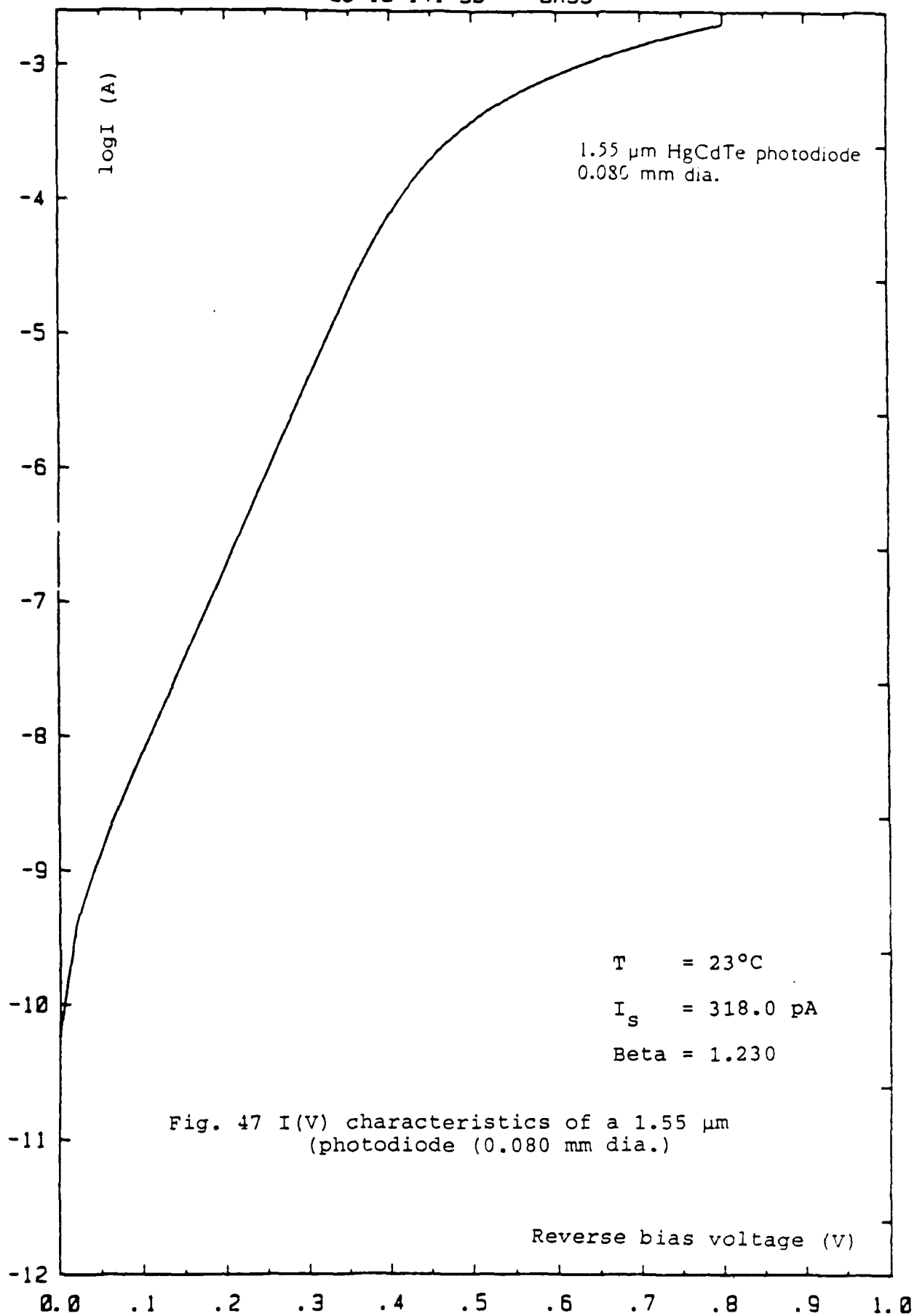


Fig. 46 I(V) characteristics of a 1.3 μm photodiode (5 mm dia.)

83-13-141-35

BA33



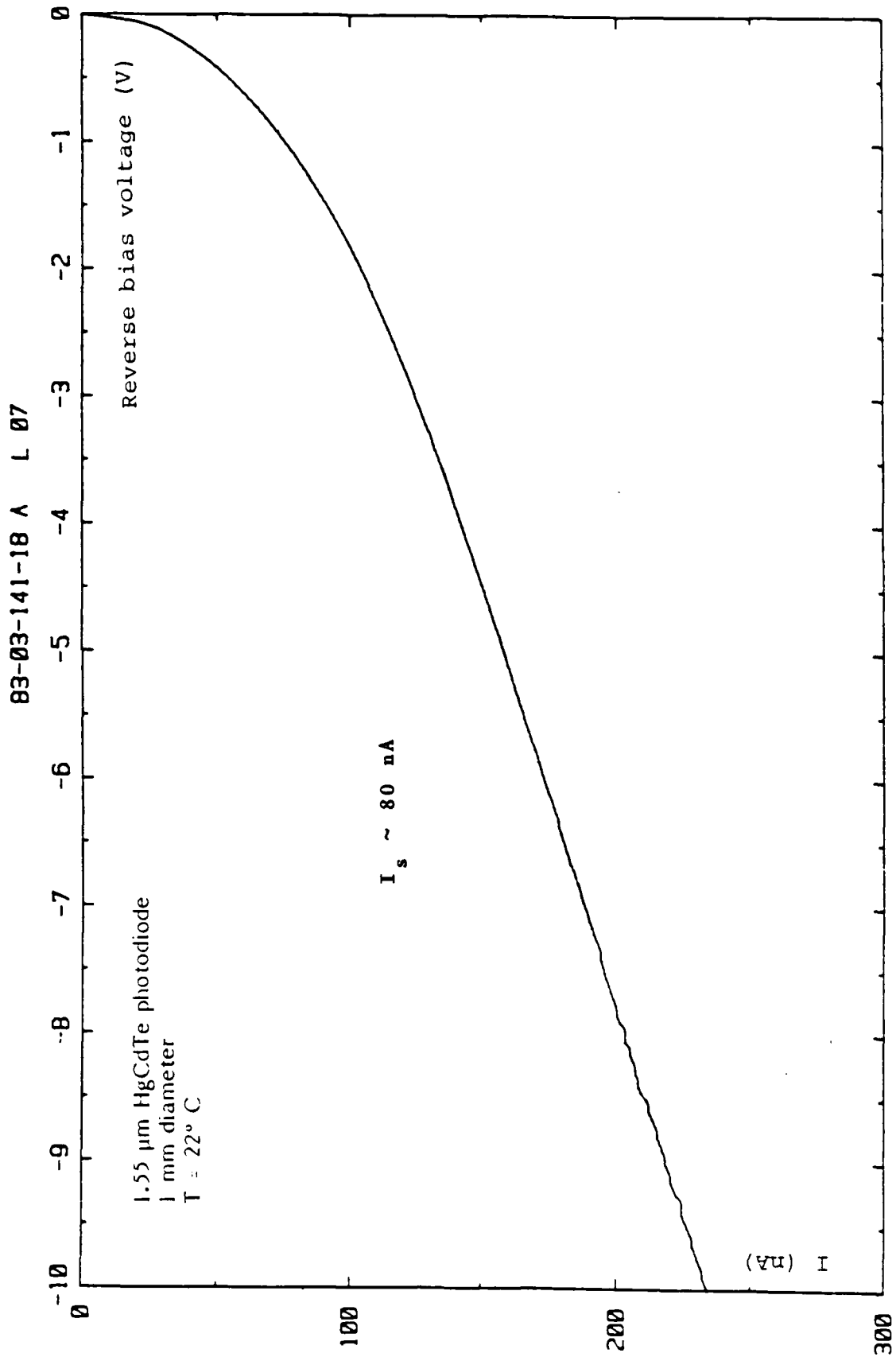


Fig. 48 I(V) characteristics of a 1.55 μm photodiode (1 mm dia.)

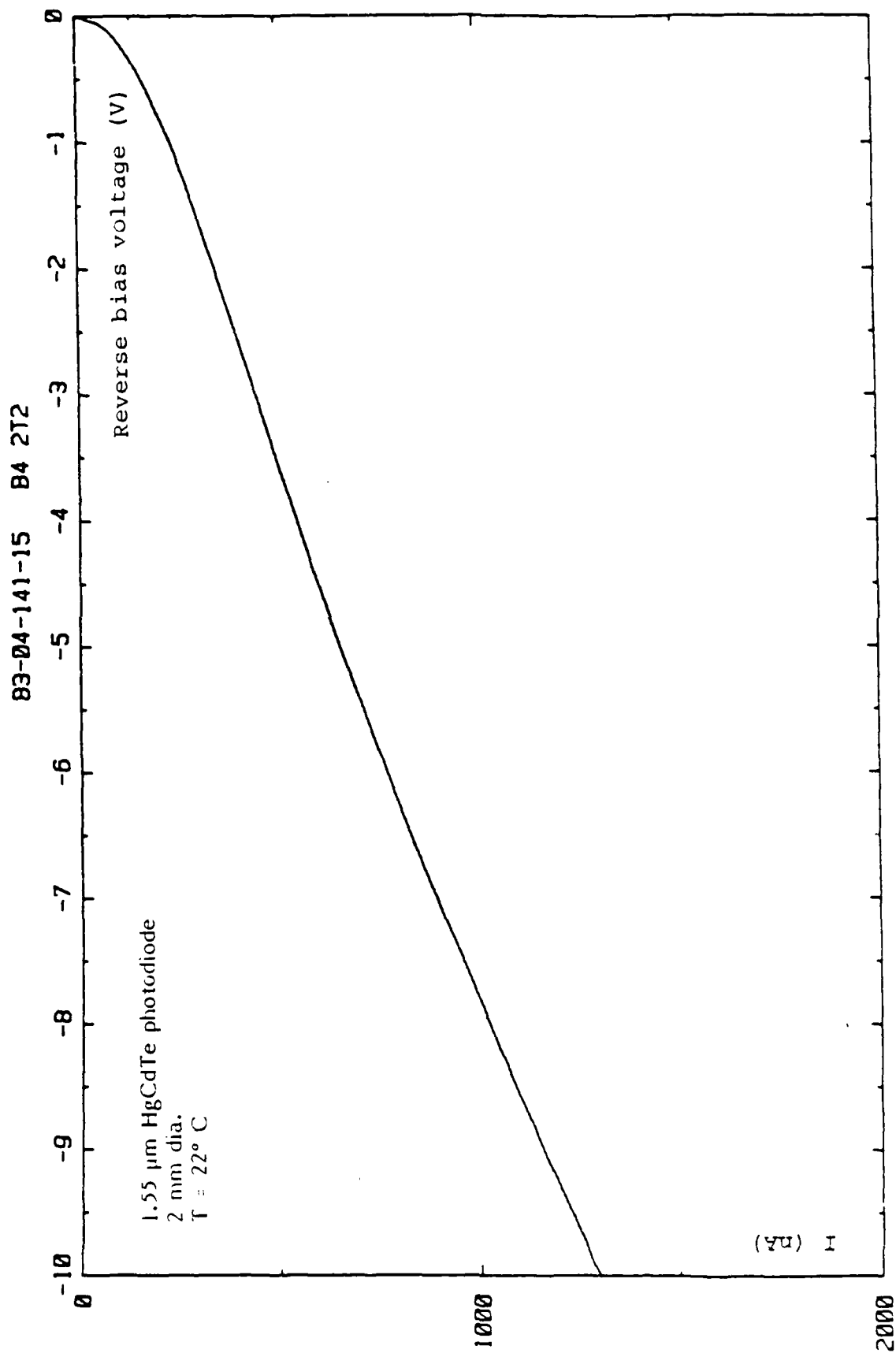


Fig. 49 I(V) characteristics of a 1.55 μm photodiode (2 mm dia.)

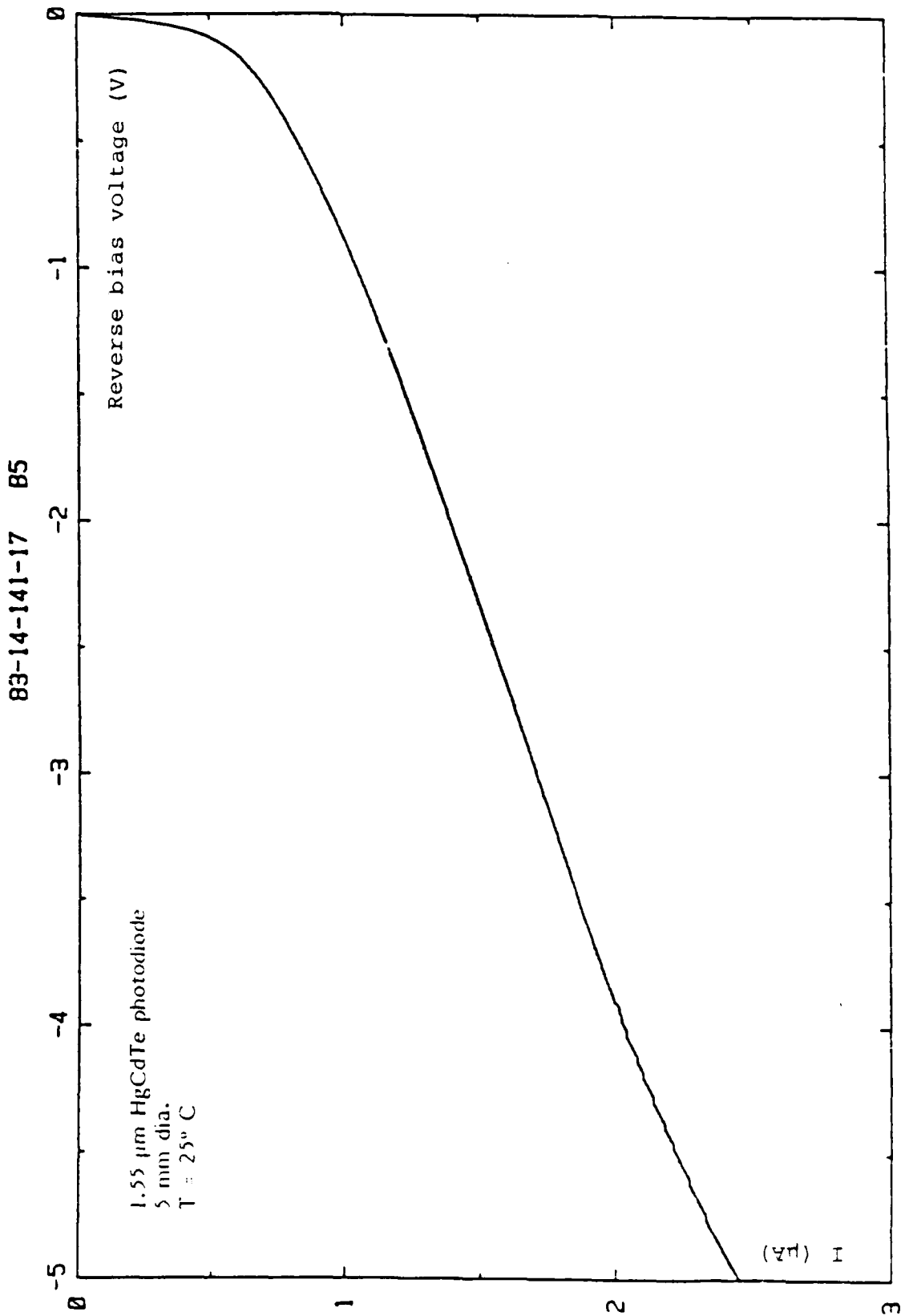


Fig. 50 I(V) characteristics of a 1.55 μm photodiode (5 mm dia.)

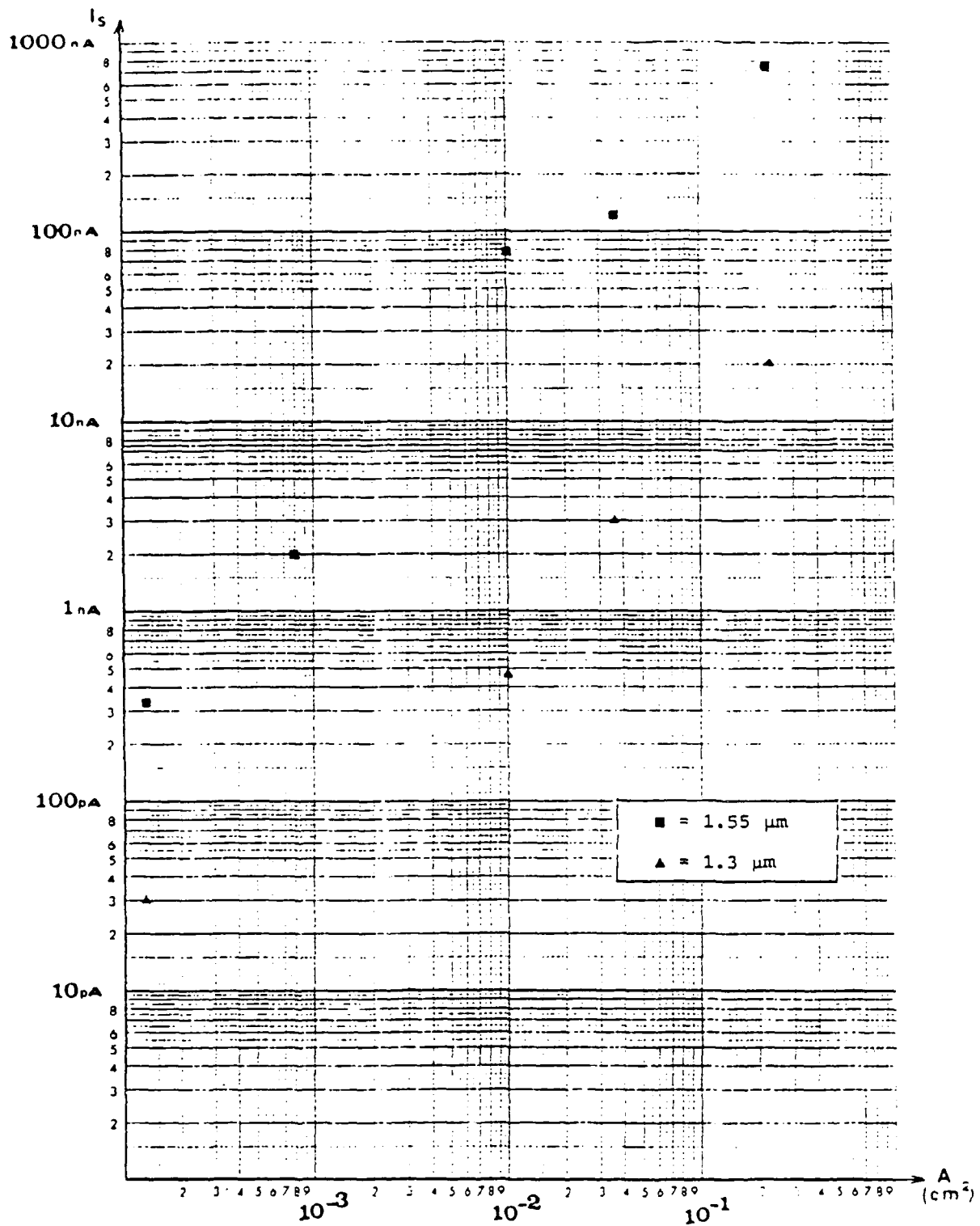


Fig. 51 Saturation current as a function of diode area

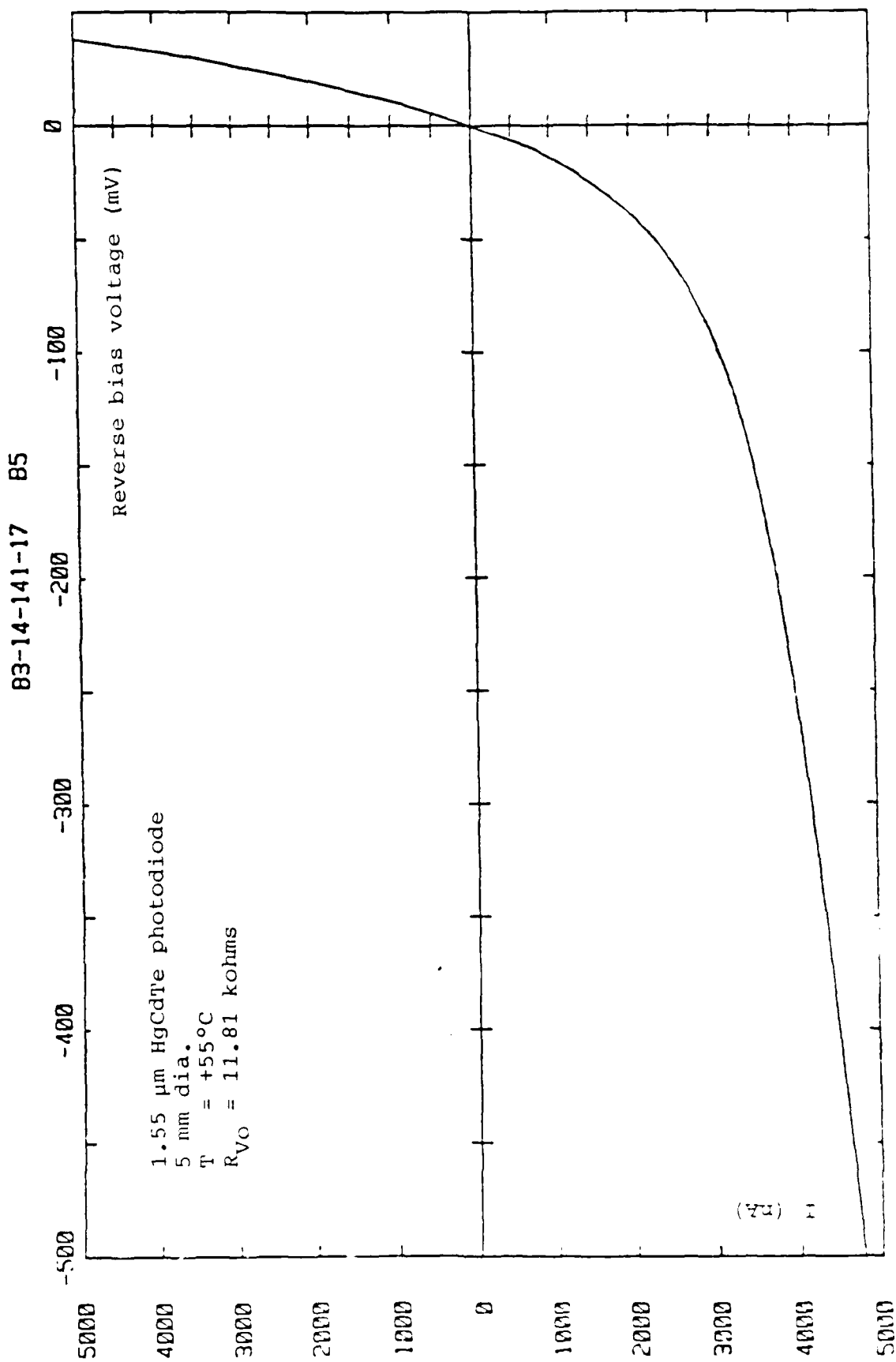


Fig. 52 I(V) characteristics of a 1.55 μm photodiode, 5 mm dia., at $T = +55^\circ\text{C}$

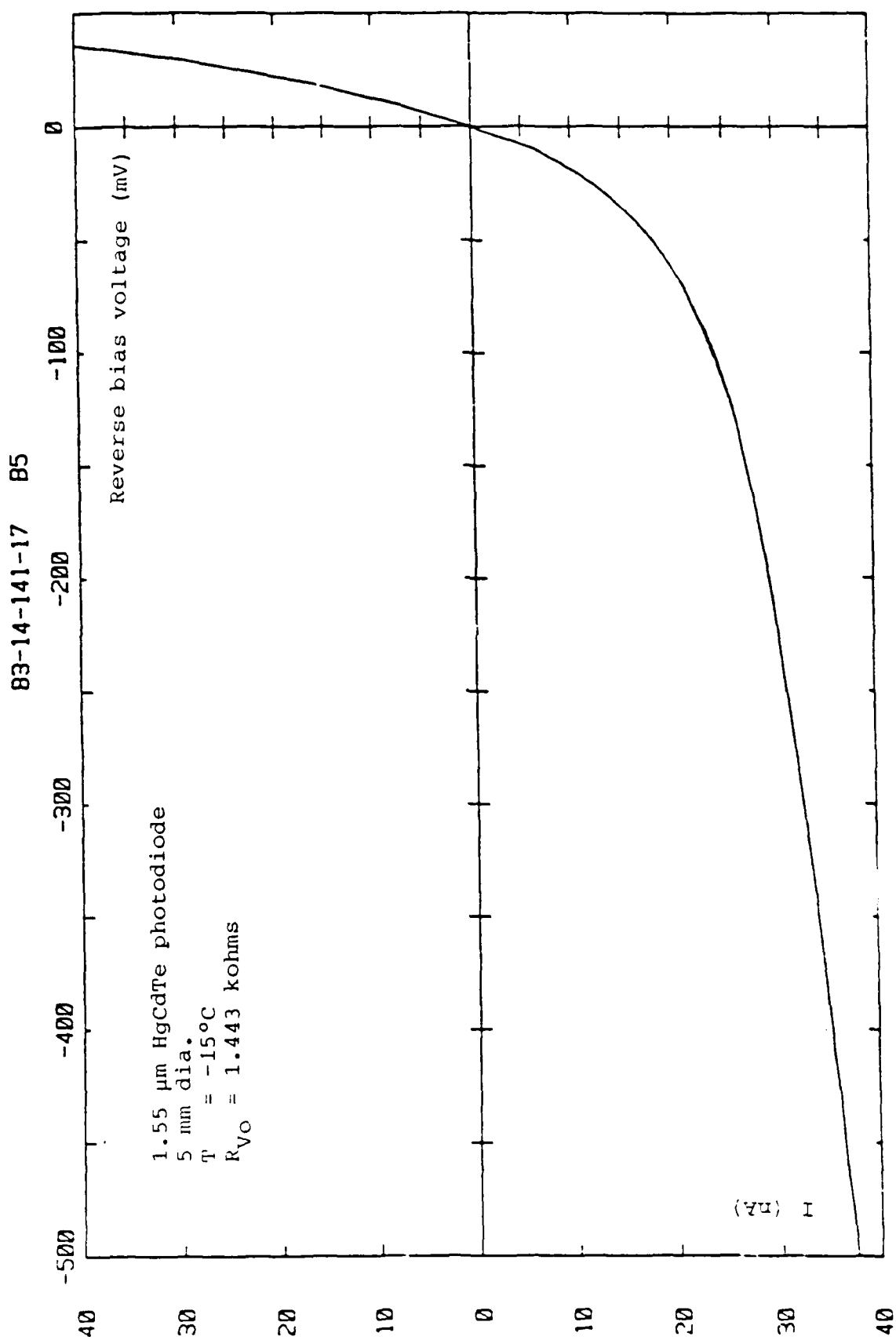
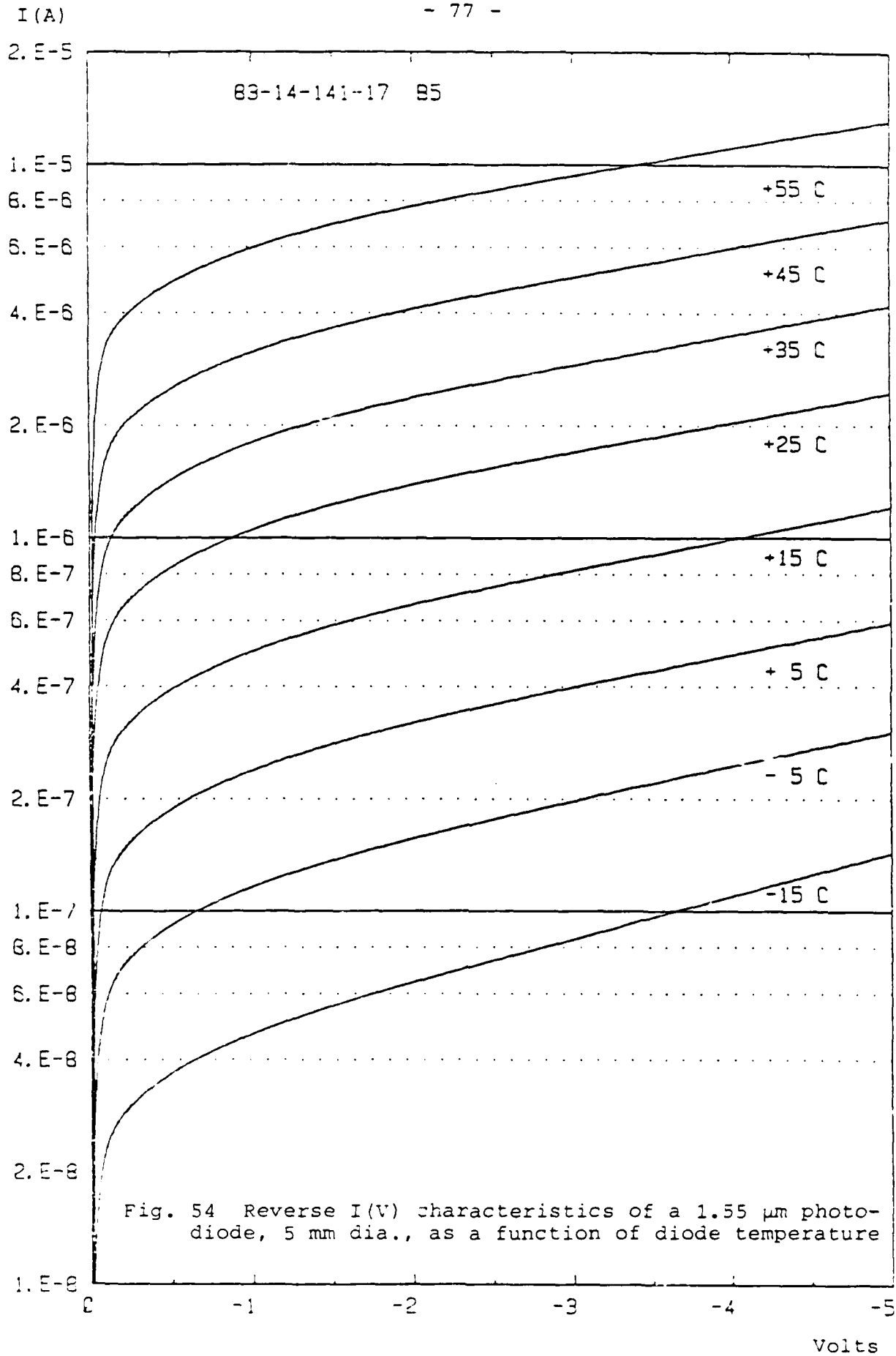


Fig. 53 I(V) characteristics of a 1.55 μm photodiode, 5 mm dia., at $T = -15^\circ\text{C}$



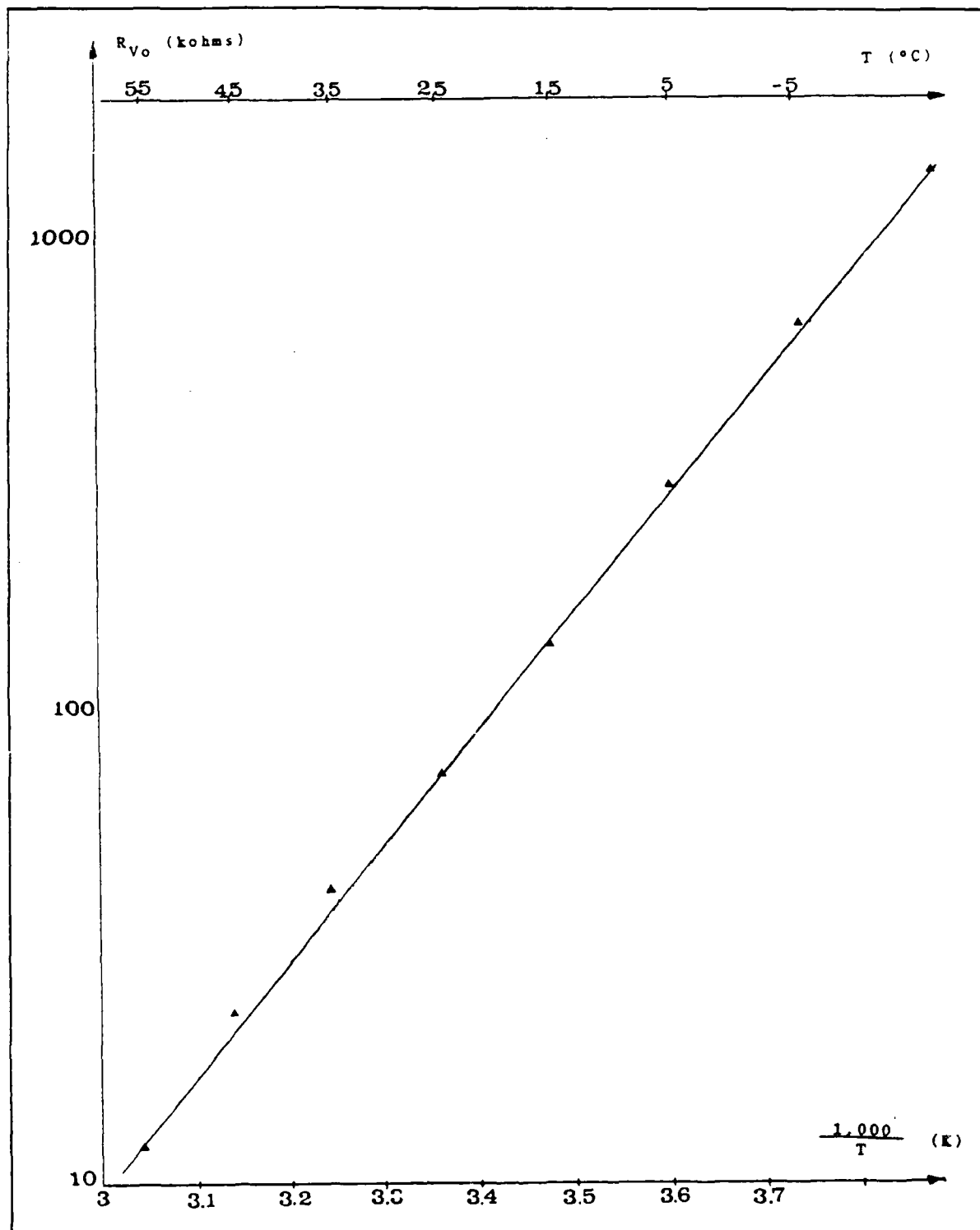


Fig. 55 Reverse variation of R_{V0} as a function of diode temperature

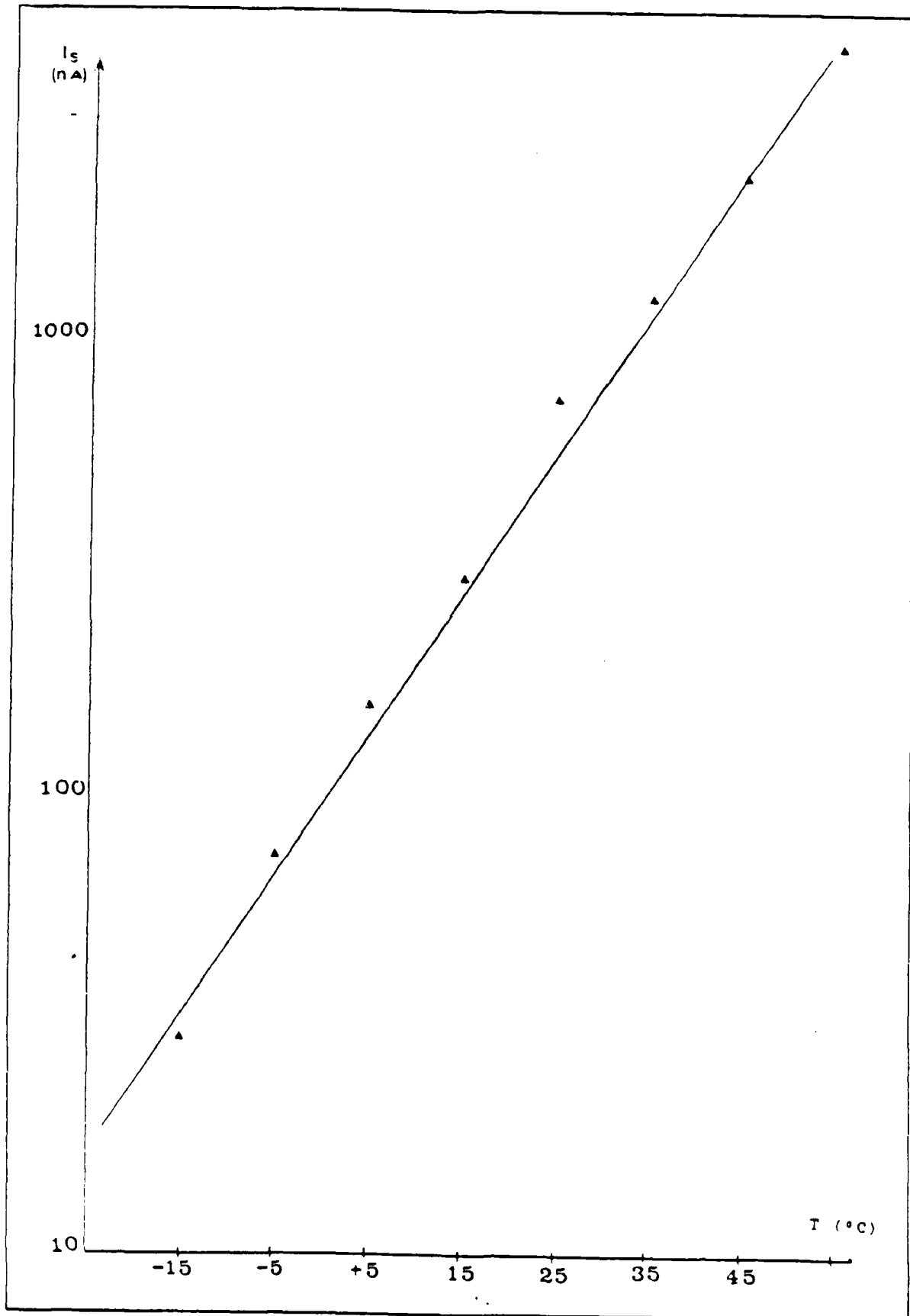


Fig. 56 Variation of saturation current as a function of diode temperature

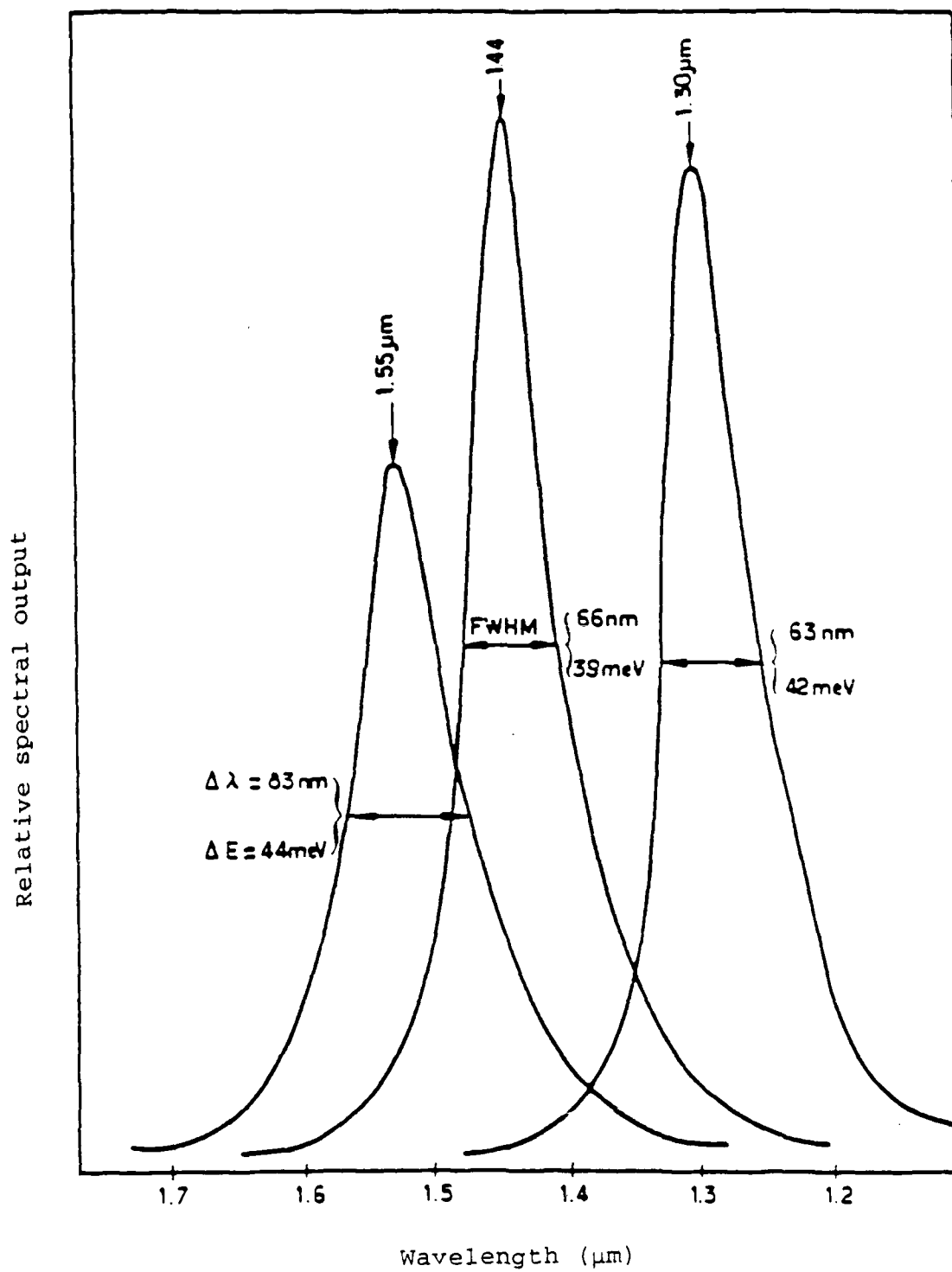


Fig. 57 HgCdTe photodiode emission spectra

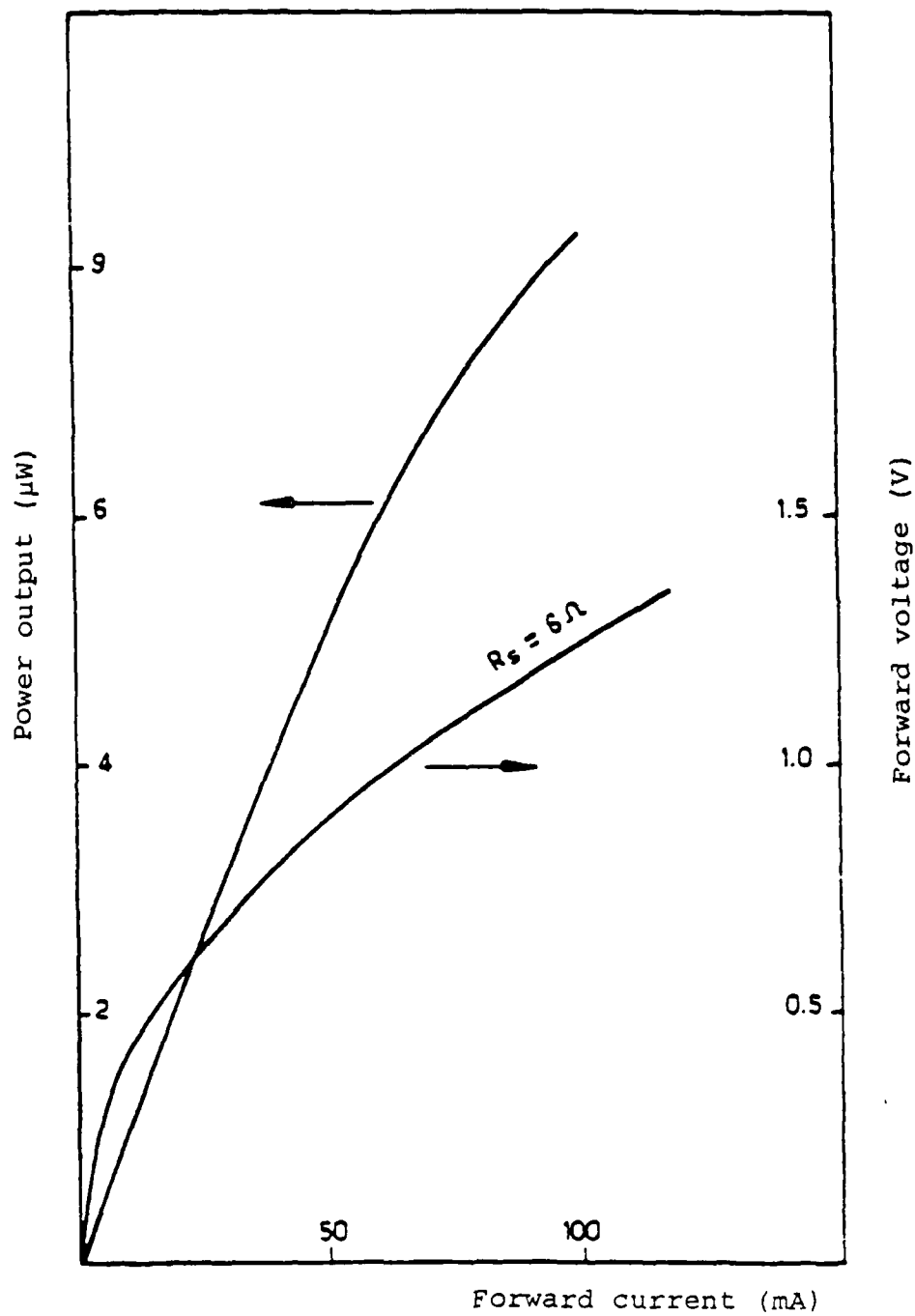


Fig. 58 Emitted power as a function of current and I(V) characteristics